Selected Papers from the International Conference on Nuclear Energy for New Europe 2007

Guest Editors: Igor Jenčič, Ivo Kljenak, and Martina Adorni

Selected Papers from the International Conference on Nuclear Energy for New Europe 2007

Selected Papers from the International Conference on Nuclear Energy for New Europe 2007

Guest Editors: Igor Jenčič, Ivo Kljenak, and Martina Adorni

Contents

Editorial

Selected Papers from the International Conference on Nuclear Energy for New Europe 2007

Igor Jenčič,[1] Ivo Kljenak,[1] and Martina Adorni[2]

[1] *Jožef Stefan Institute, 1000 Ljbljana, Slovenia*
[2] *San Piero a Grado Nuclear Research Group (GRNSPG), Department of Mechanical Nuclear and Production Engineering, University of Pisa, via Diotisalvi 2, 56122 Pisa, Italy*

Correspondence should be addressed to Martina Adorni, m.adorni@ing.unipi.it

We are proud to introduce this special issue of the journal "Science and Technology of Nuclear Installations," which is devoted to selected papers from *the International Conference "Nuclear Energy for New Europe 2007."* The conference was organized by the Nuclear Society of Slovenia and Jožef Stefan Institute, and took place from September 10 to 13, 2007, in Portorož, Slovenia.

Although it began modestly as the yearly meeting of the Nuclear Society of Slovenia, this annual conference has gradually become a truly international meeting of professionals, researchers, academics, members of regulatory bodies, and others involved in the peaceful use of nuclear energy. The *International Conference "Nuclear Energy for New Europe 2007"* was the 16th in the series. The conference was attended by 175 registered participants from 22 countries. Altogether, 112 papers were presented: 48 orally during plenary sessions and 64 as posters. The conference thus proved again to be an international forum for the exchange of ideas from various topics related to nuclear energy.

This is the first time that extended versions of selected papers from the conference are published in a special issue of an international journal. Although the idea of publishing such a special issue has been discussed for some years, it was not realized until now due to the lack of opportunity. The journal "Science and Technology of Nuclear Installations" proved to be a suitable publication for such an undertaking.

After the closing of the conference, authors of papers, presented at the conference, were invited to submit extended papers for publication in the special issue. Papers that were submitted then went through an extensive peer-review process to ensure a high quality of the publications. As a result, 13 papers are included in this special issue. The papers belong to various topics that were considered at the conference.

We take this opportunity to express our gratitude to the conference organizers, to the members of the program committee who performed the first selection of papers and elaborated the conference program, and the reviewers who contributed to the final form of this special issue. Last but not least, we would like to thank Hindawi Publishing Corporation for offering the possibility for this special issue and the members of its editorial staff for all the assistance they have provided.

Igor Jenčič
Ivo Kljenak
Martina Adorni

Research Article

Power Distribution and Possible Influence on Fuel Failure in WWER-1000

Ján Mikuš

Research Centre Řež Ltd., 250 68 Řež, Czech Republic

Correspondence should be addressed to Ján Mikuš, mik@ujv.cz

The work is focused on the influence of investigation of some core heterogeneities and construction materials on the space power (fission rate) distribution in WWER-1000-type cores, especially from viewpoint of the values and gradient occurrence that could result in static loads with some consequences, for example, fuel pin (FP) or fuel assembly (FA) bowing and possible contribution to the FP failure root causes. For this purpose, experimental data and their analysis from two earlier performed measurements on light water, zero-power reactor LR-0 were used, concerning the relative radial power distribution determined by measurements in a WWER-1000-type core containing single FPs with homogeneous gadolinium admixture (Gd_2O_3) and the relative radial power distribution determined by measurements in FA situated on the periphery of a WWER-1000-type core neighbouring the baffle (thermal shielding).

1. INTRODUCTION

The LR-0 reactor in the Nuclear Research Institute Řež plc is an experimental facility for determination of the neutron-physical characteristics of the WWER- and PWR-type lattices and shielding with UO_2 or MOX fuel. Exploitation of this facility is determined by maximum power of 5 kW and maximum thermal neutron flux density of 10^{13} m^{-2}s^{-1}, atmospheric pressure, and room temperature (or heating up to 70°C). The fuel consists of the shortened WWER-1000- and WWER-440-type fuel assemblies (FAs) containing the fuel pins (FPs) with UO_2 pellets (O.D. 7.53 mm, internal central hole 1.4 mm) having a Zr + 1% Nb cladding (O.D. 9.15 × 0.72 mm) with the active length of 1250 mm and enrichment of 1.6–4.4 wt.% in ^{235}U. The FAs can be arranged in a reactor vessel of aluminium (diameter 3.5 m, height 6.5 m); the criticality is controlled by moderator level (boron acid with concentration up to 12 g/L) and control clusters (B_4C pellets).

The most important applications on LR-0 reactor concern the nuclear safety and economy of the WWER-type nuclear power plants (NPPs) operation. In the frame of their modernization, a set of experiments has been performed on the LR-0 reactor, for example, with new type FAs with various burnable absorbers arranged in appropriate configurations and cores of the both WWER-440 and WWER-1000 types including a number of experiments with FAs containing single FPs with Gd (Gd FPs) burnable absorber (Gd_2O_3) integrated into fuel (e.g., [1, 2]). Next experiments concerned the reactor pressure vessel dosimetry and they included measurements of the power (fission rate) distribution in periphery FAs neighbouring the baffle in WWER-1000-type cores (e.g., [3]). Results of power (fission rate) distribution measurements presented in [1–3] are used and analysed in this work.

It is well known that presence of single Gd FPs in reactor core results in a local depression of thermal neutrons in these FPs and corresponding gradients in neighbouring FPs. As for the baffle influence, thermal neutron gradients can be expected in neighbouring FAs, too. Similar situation can also be stated as for the power release and corresponding temperature.

It is also well known (e.g., [4, 5]) that neutron flux nonuniformity, gradients of the temperature, and neutron current can represent root causes of the FP/FA growth and bowing leading to local limitation of coolant flow, reduction of heat transfer, magnifying cladding corrosion, and pellet/cladding interaction (PCI). Therefore detailed
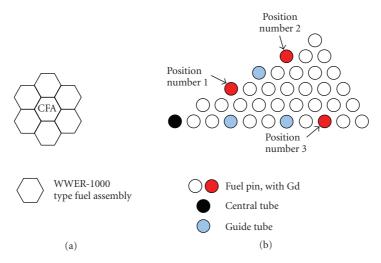
FIGURE 1: (a) Schematic arrangement of the LR-0 reactor core containing 7 WWER-1000 type-FAs with central FA (CFA) for Gd FP influence investigation and (b) the 30-degree symmetry sector of the CFA with 3 Gd FPs.

information about power distribution in FA containing single Gd FPs and in periphery FA neighbouring the baffle in WWER-1000-type core can be useful for above phenomenon investigation. Since such data cannot be obtained in the NPPs, some experiments on research reactors are provided.

As for the fuel performance reliability and fuel failure rates and root causes concerning WWER fuel, it was stated [6] that an overview on WWER fuel failure root causes identified during 1992–2002 shows that

(i) besides a large number of unidentified causes, the most frequent cause is damage by debris;

(ii) different from Western PWR fuel experience, fuel-rod-to-spacer-fretting does not play a significant role;

(iii) at the same time there is a very high number of defected fuel where no failure cause is known.

In case of the PWR fuel the EPRI evaluation of 2004 on US PWR fuel failure rates shows [6] that

(i) after a continuous decrease from 1980 to 2001, there is some increase observed in 2002 and 2003;

(ii) the major contributor to fuel failure rates in PWRs remains grid-to-rod fretting;

(iii) there is also an increase of fuel failures with unknown root causes that primarily affects optimised fuel designs with a thinner rod diameter.

The above information is in accordance with results concerning examination of 5 WWER-440 and 7 WWER-1000 FAs presented in [7]: causes of failure are debris fretting (54%), local overheating (15%), grid-rod fretting (8%), and "the cause is not determined" (23%).

2. AIM OF WORK

The aim of this work is providing some information about below heterogeneities and construction material influence on

radial power (fission rate) distribution in WWER-1000-type cores, namely, concerning the

(i) single Gd FPs by means of power release in an FA containing these FPs,

(ii) baffle by means of power release in selected FPs in neighbouring FA.

3. INFLUENCE OF SINGLE FUEL PINS WITH GADOLINIUM ON POWER DISTRIBUTION IN A WWER-1000-TYPE CORE

3.1. Experimental arrangement and conditions

The materials published in [1, 2] were used for this work preparation. Experiment was realised on reactor LR-0 with critical height of the H_2O moderator level being 266.10 mm ("0" level is at the lower end of FP active part), at atmospheric pressure and room temperature in a WWER-1000-type core shown in Figure 1(a), consisting of 7 FAs, each containing 312 FPs with 4.4% enrichment, whereas 18 FPs in central FA (CFA) were replaced by FPs with 3.6% enrichment containing 2.0% (by weight) of Gd_2O_3 admixture (Gd FP pellets with O.D. 7.50 mm, internal central hole 1.5 mm), arranged with FP pitch of 12.75 mm; the 30-degree symmetry sector of CFA with 3 Gd FPs is shown in Figure 1(b). More information concerning experimental arrangement and conditions can be found in [1, 2].

3.2. Results

The power (fission rate) distribution was determined by means of gamma scanning of irradiated FPs, measuring their gamma radiation in the energy range of 600 to 900 keV. The radial distribution (in a plane perpendicular to the core axis) was determined measuring FPs activity of 50 mm region of FP surface at the central irradiated part along rotating FP using corresponding collimator. Measurements
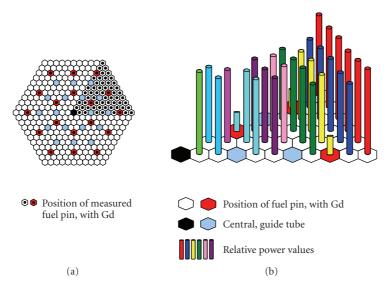
FIGURE 2: (a) Positions of measured FPs in CFA and (b) power distribution in the 30-degree symmetry sector of the CFA with 3 Gd FPs.
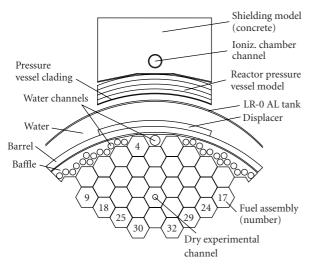
FIGURE 3: The section of the mockup by the XY plane.

FIGURE 4: WWER-1000 mockup general view on reactor LR-0.

were performed in CFA at 74 FPs with positions shown in Figure 2(a); detailed results were presented in [2] and used for evaluation of power distribution in symmetry sector of CFA shown in Figure 2(b). As for this evaluation, absolute value of the difference of power release concerning two FPs in symmetry positions (Figure 2(a)) was calculated and related to the average of these two values and this was done for all above symmetry positions to check reproducibility of the results presented in [2]. The mean and maximum above relative differences are 1.1% and 3.8%, respectively.

Further experimental results were compared with calculations based on a code treats the two-dimensional, four-group diffusion equations using the so-called fine mesh method (each FP cell or absorbing rod cell is considered as one point) and presented in [2]. Results of calculations and measurements are in fairly good agreement: the mean value of the relative power distribution difference absolute values

is 2.4%; maximum positive and negative relative differences are 6.2% and -12.7%, respectively.

Finally the shape of the power distribution in the neighbourhood of a Gd FP can be characterised by the following ratio:

$$Q = \frac{\text{(average energy release at ring of 6 FPs around a Gd FP)}}{\text{(energy release in that Gd FP)}}. \tag{1}$$

As for Gd FPs (Figure 1(b)) in positions nos. 1, 2, and 3, the following experimental Q_E/calculated Q_C values were determined: 3.718/3.553, 3.669/3.501, and 3.694/3.523 with
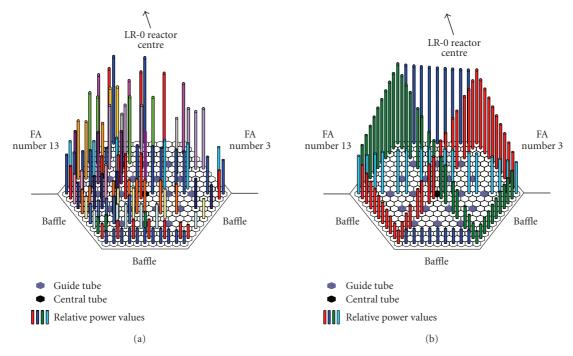
Figure 5: (a) Experimental and (b) calculation power distribution values in selected FP positions in FA no. 4.

relative difference d = 45%, 4.7%, and 4.7%, respectively, where

$$d = \frac{(Q_E - Q_C)}{[(Q_E + Q_C)/2]}. \qquad (2)$$

A fairly good agreement between measured and calculated power distributions can be stated, given by above mean value of 2.4%, as well as between experimental Q_E and calculated Q_C quantities given by above difference d being about 4.7% for all three Gd FP positions. The power release depression in Gd FPs can be characterised by the value of $1/Q$ with corresponding values in positions 1, 2, and 3 being 26.9%, 27.3%, and 27.1%, respectively.

4. INFLUENCE OF BAFFLE IN WWER-1000-TYPE CORE ON POWER DISTRIBUTION IN NEIGHBOURING FA

4.1. Experimental arrangement and conditions

A 60-degree symmetry sector of WWER-1000 mockup in radial direction was realised in the LR-0 reactor at 4.6 ± 0.1 g/l boron acid concentration in moderator with critical height of 1500 mm ("0" level is at the lower end of FP active part), at atmospheric pressure and room temperature—Figures 3 and 4.

This mockup represents the core periphery and radial shielding heterogeneities of the WWER-1000. The core loading was chosen to imitate neutron source in $R - \theta$ geometry with following FAs no./enrichment: 2 FAs nos. 9, 17/3.3%, 6 FAs nos. 18, 24, 25, 29, 30, 32/3.0% and remaining 24 FAs with 2.0% enrichment (more information in [3]). The materials published in [3] were used for this work preparation.

4.2. Results

Influence of the baffle was investigated by means of power (fission rate) distribution in neighbouring FA no. 4, using gamma scanning of irradiated FPs, measuring their gamma radiation of the ^{140}La with energy 1596.5 keV. The radial distribution (in a plane perpendicular to the core axis) was determined by FPs activity of 50 mm region of FP surface at the central part along rotating FP using corresponding collimator.

Results of the power distribution measurements carried out in 107 FP positions in FA no. 4 are presented in Figure 5(a). Power distribution values were determined with mean and maximum relative errors being 3.2% and 5%, respectively.

Obtained experimental values were completed by calculations carried out in all 312 FA positions [3]. They are illustrated by values in selected FP positions in Figure 5(b).

Presented results demonstrate depression of the power distribution in FA no. 4 neighbouring baffle that can be characterised by the ratio of the power distribution mean values in two opposite FP rows in FA no. 4 to- and outwards the baffle. The depression, for example, the above ratio of about 19%, can be stated.

5. DISCUSSION

As for gadolinium influence, the obtained results have limited information relevance since the experiment was realised in 1990 at special conditions as mentioned above and therefore these results can differ from ones corresponding to the real NPP cores because of dependence, for example, on enrichment and dimensions of the (Gd) FPs, Gd_2O_3

contents, FP pitch, and Gd FP positions in FA, boron acid concentration in moderator, temperature, pressure, and so forth.

Similar situation can also be stated concerning the baffle influence. Further, a less influence of baffle on power distribution (depression) can be expected in an NPP core (with real WWER-1000 dimension) because of less dimension of LR-0 core used for investigation.

6. CONCLUSIONS

On reactor LR-0 in WWER-1000-type cores the influence of single Gd FPs and the baffle on the space power (fission rate) distribution was investigated. A strong power release depression of about 27% in a single Gd FP (3.6% enrichment, 2.0 wt.% Gd_2O_3) was determined, given by the ratio of energy release in that Gd FP and average energy release at ring of 6 FPs (4.4% enrichment) around this Gd FP. As for baffle influence in neighbouring FA, the power release depression of about 19% was estimated, given by the ratio of the power distribution mean values in two opposite FP rows in this FA to- and outwards the baffle.

The above results can be utilised for obtaining some information for the temperature gradients and resulting loads estimation in FPs neighbouring a Gd FP and in FA neighbouring the baffle to consider possible contributions of these loads to the FP failure root causes.

REFERENCES

[1] J. Mikuš, F. Hudec, J. Roček, M. Trgiňa, L. Vrba, and K. Záleský, "Gadolinium absorbers in WWER-1000 type fuel lattices," in *Advanced Calculational Methods for Power Reactors and Lwr Core Design Parameters, Proceedings of the Specialists Meeting, Cadarache, France, September 1990, and a Technical Committee Meeting*, pp. 340–344, Řež, Czech Republic, October 1991, IAEA-TECDOC-678.

[2] F. Hudec, J. Mikuš, J. Roček, M. Trgiňa, L. Vrba, and K. Záleský, "Investigations with WWER-1000 type fuel assemblies with Gd-burnable absorbers on LR-0 reactor," in *Proceedings of the 1st Symposium of Atomic Energy Research*, Řež, Czechoslovakia, September 1991.

[3] B. Ošmera and S. Zaritsky, "WWER-1000 mock-up experiment," Tech. Rep. 36/8-2002, Nuclear Research Institute Řež, Institute of Nuclear Reactors RRC "Kurchatov Institute", Řež, Czech Republic, May 2002, Contract IAEA No. RER 4017-04583G,.

[4] E. A. Panov, Yu. M. Shestakov, and V. N. Miglo, "Analysis of trends in fuel rod depressurization and determination of "gas leak" and "pellet-water interaction" type failures using radiation monitoring techniques of fuel rod leak tightness, fuel failure in normal operation of water reactors: experience, mechanisms and management," in *Proceedings of the Technical Committee Meeting*, pp. 263–271, Dimitrovgrad, Russia, May 1992, IAEA-TECDOC-709.

[5] Yu. Likhatchev, V. Troyanov, V. Folomeev, and A. Demishonkov, "Theoretical approach to the WWER core thermomechanical modelling," in *Proceedings of the 5th International Conference on WWER Fuel Performance, Modelling and Experimental Support*, pp. 209–216, Albena, Bulgaria, September-October 2003.

[6] H. G. Weidinger, "PWR and WWER fuel performance: a comparison of major characteristics," in *Proceedings of the 6th International Conference on WWER Fuel Performance, Modelling and Experimental Support*, pp. 40–50, Albena, Bulgaria, September 2005.

[7] D. Markov, V. Smirnov, A. Smirnov, S. Perepelkin, and V. Polenok, "Integration of post-irradiation examination results of failed WWER fuel rods," in *Proceedings of the 5th International Conference on WWER Fuel Performance, Modelling and Experimental Support*, pp. 273–277, Albena, Bulgaria, September October 2003.

Research Article

Modelling of the Production of Source Neutrons from Low-Voltage Accelerated Deuterons on Titanium-Tritium Targets

A. Milocco and A. Trkov

Reactor physics department (F8), Jožef Stefan Institute, Jamova 39, 1000 Ljubljana, Slovenia

Correspondence should be addressed to A. Milocco, alberto.milocco@ijs.si

Fast quasi-monoenergetic neutrons can be produced by accelerating charged deuterons on tritium solid targets. Benchmark experiments were performed in many laboratories with intense D-T neutron sources. The aim is to validate the computational models and nuclear data for fusion applications. The detailed information on the neutron source term is highly important for the benchmark analyses. At present, the MCNP family of codes cannot explicitly model the D-T reaction for Deuterons in the KeV energy range. The physics for the D-T neutron production was modelled at ENEA (Italy) in the SOURCE and SRCDX subroutines to compile with the MCNP source code. Some improvements to the original subroutines were introduced. The differential cross-sections for the D-T reaction from the ENDF/B-VII library were built into the code. The relativistic approach was implemented for neutron kinematics. The new D-T neutron source model was applied to the MCNP5 simulation of the tungsten integral experiment performed at the OKTAVIAN facility. The uncertainty associated with the realistic D-T reactions was separated from the total uncertainty of the source term. The outcome of the benchmark analysis was an improvement in the quality of the computational model of the experiment.

1. INTRODUCTION

The first device for the acceleration of charged particles has been constructed by Cockroft and Walton in 1932, the same year when Chadwick discovered the neutron. Since the 1950s tritium was available as a target material to produce ~ 14 MeV neutrons by the ${}^3\text{H}(d, n){}^4\text{He}$ reaction, which is still the first candidate for plasma fusion technology. Thus, these neutron generators have been widely used to study the interaction of the neutrons with the structural materials of fusion reactors. Other applications of the device include neutron activation analysis, low cross-section measurements, and neutron therapy. The broad resonance of the D-T cross-section at the deuteron energy of 109 KeV permits high yields of fast neutrons to be obtained with low-voltage deuteron accelerators [1]. Integral experiments for fusion technology have been collected in the International Database for Integral Shielding Experiments (SINBAD), which is coordinated by the OECD Nuclear Energy Agency (http://www.nea.fr/)

and Radiation Safety Information Computational Center (http://www-rsicc.ornl.gov/).

A lot of effort is devoted to computational techniques for neutron transport. A real source is not isotropic or monoenergetic. Primary neutrons are generated by deuterons which have interacted in the target and lost part of their original energy. The experimentalists usually provide the source specifications, but these specifications need a detailed investigation to determine parameter uncertainties, whose different contributions are difficult to separate out in a real experiment. Special attention is needed to define the anisotropy of the source and the neutron yield as a function of its flight directions, as well as the spread in the emitted neutron energies.

The MCNP family of codes cannot explicitly model the deuteron transport and neutron emission from the D-T reaction for incident deuterons with energies in the KeV range. At ENEA (Italy), a D-T source model was developed, which includes the effect of the deuteron slowing down inside

a titanium-tritium target and the D-T reaction kinematics. The model is implemented in MCNP subroutines (e.g., SOURCE, SRCDX), which define the neutron source when compiled with the MCNP source code. The subroutines are available in SINBAD database.

The present work is a case study to identify the essential information which is needed for the source definition in computational analyses. Section 2 illustrates the approach to the D-T reaction kinematics from first principles. These results allow a refinement of the original ENEA source subroutines (described in Section 3). The upgraded D-T source model is internally validated by reproducing the theoretical angle dependence of the neutron energy and yields and by cross-validating the cell flux with the point detector flux. In Section 3 a brief description of the deuteron transport model is also provided. The sample case (Section 4) concerns the 14 MeV neutron facility OKTAVIAN, which was built at Osaka University and has been operating since 1981. In the framework of the SINBAD project the measured neutron leakage spectra from a Tungsten sphere were analysed. In this work the source model from the previous analysis is compared to the MCNP5 calculation with the improved neutron source model. The outcome of the benchmark analysis represents an improvement in the quality of the computational model of the experiment.

2. THEORETICAL FRAMEWORK OF THE D-T REACTION

The ^{3}H(d, n)^{4}He reaction is properly modelled as a two-body reaction. Some nomenclature: in Figure 1 the subscript "a" denotes the incident particle (deuteron), "b" the target particle (tritium), "1" the emitted neutron and "2" the alpha particle. P and θ are the momenta in the laboratory frame and the angles between the outgoing particle and the deuteron direction. The energy of the outgoing neutron (E_1) is calculated according to the relativistic equation (1). E_a is the relativistic energy of the deuterons, which are given a nominal kinetic energy of 280 KeV:

$$
\begin{aligned}
E_1 = & \left\{ \left(E_a + m_b \right)^2 - P_a^2 \cos^2 \theta_1 \right\}^{-1} \\
& \times \left[\left(E_a + m_b \right) \left\{ m_b E_a + \frac{1}{2} \left(m_a^2 + m_b^2 + m_1^2 - m_2^2 \right) \right\} \right. \\
& + P_a \cos \theta_1 \left[\left\{ m_b E_a + \frac{1}{2} \left(m_a^2 + m_b^2 - m_1^2 - m_2^2 \right) \right\}^2 \right. \\
& \left. \left. - m_1^2 m_2^2 - m_1^2 P_a^2 \sin^2 \theta_1 \right]^{1/2} \right].
\end{aligned}
$$

(1)

The effect of the relativistic kinematics formulation is studied in comparison with the classical kinematics equations. The relativistic equations are implemented in a MATLAB function (RELKIN.M) for graphical purposes (Figure 2). The original source for the particle masses is the NIST reference on constants, units, and uncertainties web site (http://physics.nist.gov/), except for triton. This is computed subtracting the electron contribution to the tritium mass
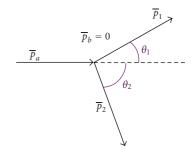
FIGURE 1: Scheme of two body reaction model.
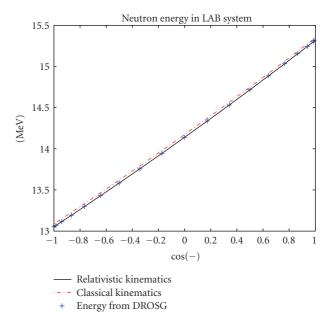
FIGURE 2: Comparison of relativistic and classical approach of energy-angle dependences of D-T neutron yielding.

taken from the atomic mass tables of G. Audi and A. Wapstra (http://www-nds.iaea.org/amdc/web/masseval.html). It is worthwhile to point out that in the ENDF-6 formats manual [2] this datum is incorrect. The calculation of the Q-value for the D-T reaction is 17.589 MeV. The relativistic calculation agrees with the one provided by the DROSG2000 code (http://www-nds.iaea.org/ndspub/libraries/drosg2000/), which also uses the relativistic approach. The classical results are obtained from the kinematics formulas available in the ENDF-6 formats manual. The difference in energy when solving the two-body reaction problem with the classical equations is about 30 KeV.

The angular distributions of the outgoing neutrons in the centre-of-mass system are represented by Legendre polynomials. The Legendre coefficients up to the tenth order are available in the ENDF files (MAT = 2, MF = 50, MT = 6) at the nominal deuteron energy of 280 KeV. For the conversion into the angular distribution in the laboratory frame it is necessary to calculate the momentum of the deuteron (P_a),

whose evaluation is trivial, and of the neutron (P_1) and apply the Jacobian ($d\Omega_{cm}/d\Omega_{lab}$) as follows:

$$P_1 = \left\{ (E_a + m_b)^2 - P_a^2 \cos^2\theta_1 \right\}^{-1}$$

$$\times \left[P_a \cos\theta_1 \left\{ m_b E_a + \frac{1}{2}(m_a^2 + m_b^2 + m_1^2 - m_2^2) \right\} \right.$$

$$+ (E_a + m_b) \left[\left\{ m_b E_a + \frac{1}{2}(m_a^2 + m_b^2 - m_1^2 - m_2^2) \right\}^2 \right.$$

$$\left. \left. - m_1^2 m_2^2 - m_1^2 P_a^2 \sin^2\theta_1 \right]^{1/2} \right],$$

$$\frac{d\Omega_{CM}}{d\Omega_{LAB}} = K \frac{P_1^2}{(E_a + m_b)P_1 - P_a E_1 \cos\theta_1},$$

(2)

K is a constant independent of the angle, so it is adjusted to normalise the distribution at zero degree. This normalisation is a common practice because the angular dependence of both the neutron energy and the neutron yield on the angle is comparatively small in the forward direction [3]. The effect of both the anisotropy in the CM system and the transformation into the LAB frame can be assessed in Figure 3. For the CM anisotropic reaction the data of DROSG2000 code are replaced by the Legendre expansion from the ENDF/B-VII library. The same coefficients are used in the RELKIN function. The calculations with the new equations coincide with the DROSG 2000 results for the angular distribution in the LAB system. It is noticeable that the anisotropy of the reaction with 280 KeV deuterons implies a difference of ~3% at backward angles in the laboratory angular distribution. As a matter of fact, at energies typical for deuteron accelerators the assumption of isotropic CM distribution is to be considered a rough approximation.

3. THE DEUTERON BEAM SLOWING DOWN

The deuteron particles hitting solid Titanium-Tritium targets get slowed down by interactions with the electrons and nuclei in the medium. The electronic stopping power, that is, the inelastic scattering with electrons, can be considered independent on nuclear interactions. On interaction with Ti or T nuclei, the deuteron deflects and loses part of its kinetic energy by elastic collisions. Eventually, the deuteron interacts with the tritium nucleus to produce one neutron. For low-energy deuterons, the only reaction branches to consider are elastic scattering and nuclear fusion. The energy and angular distributions of incident deuterons inside the target cause the primary energy spread of the neutron energy at a fixed detection angle.

For the simulation of a D-T neutron source the first choice was to search into the MCNP family of codes. The deuteron ion transport in MCNPX is performed by physics models designed for incident deuterons of 200 MeV and higher. They are able to provide a good response in the 10–100 MeV range, however, the results are poor down to the MeV range. Till now, there are no D and T nuclear
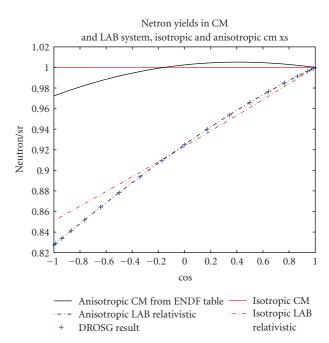
FIGURE 3: Comparison of isotropic and anisotropic D-T neutron yields in CM and LAB frames.
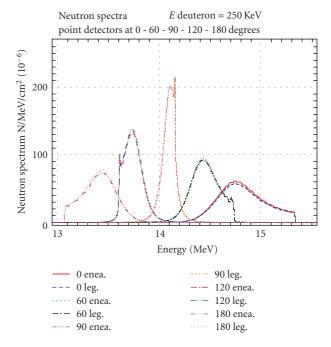
FIGURE 4: Neutron spectra calculated with the original and ENDF/B-VII cross-sections.

data libraries. Therefore, the D transport within the solid target can be achieved with MCNPX, but results are to be interpreted with caution and should be benchmarked against experiments or otherwise known answers. The D energy cut-off for the D-T fusion reaction in MCNPX is 2 MeV, so neutrons cannot be generated at the low energies of our interest. Starting from MCNP4 the possibility

Neutron spectra E deuteron = 250 KeV
point detectors at 0 - 60 - 90 - 120 - 180 degrees
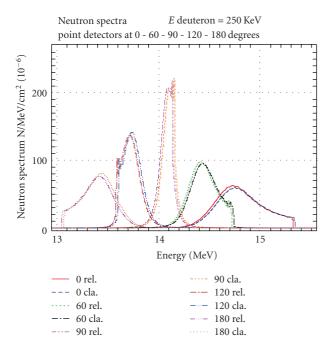
FIGURE 5: Effect of relativistic kinematics.

Neutron spectra E deuteron = 250 KeV
point detectors at 0 - 60 - 90 - 120 - 180 degrees
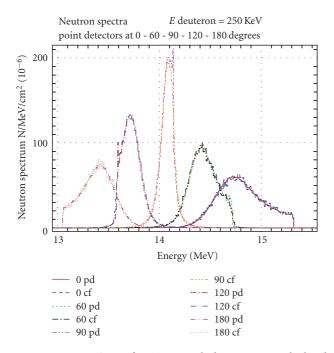
FIGURE 6: Comparison of D-T energy leakage spectra calculated with MCNP using both cell flux estimators and point detectors.

was introduced to develop and compile ad hoc source subroutines. The SINBAD database makes available the subroutines to compile with MCNP5 source codes for the simulation of the neutron emission in the Frascati neutron generator. The routines were provided by Angelone et al. from ENEA, who developed a detailed model of the FNG neutron source [4]. For the D slowing down inside the

solid FNG target the basic-language source code from TRIM software was translated into FORTRAN language. The Monte Carlo program, the Transport of Ions in Matter (TRIM), is the most comprehensive program included in SRIM (http://www.srim.org/). SRIM is a well-established collection of software packages which calculate many features of the transport of ions in matter, such as ion stopping powers and ranges in targets, ion implantation, sputtering, ion transmission, ion beam therapy. The main author is James F. Ziegler. TRIM does not model nuclear reactions. M. Pillon implemented the D-T neutron production in the TRIM-based model for the D transport inside the Ti-T target. The essential characteristics of the ENEA D-T source model are the following:

(1) Monte Carlo method,

(2) free flight paths between collisions, which "condense" negligible amounts of energy transfer and deflection angles,

(3) impulse approximation for the free flight paths in the low-energy range,

(4) universal interatomic potential,

(5) Rutherford scattering at higher ion energies,

(6) electron stopping power data from the TRIM code tables,

(7) D-T double differential cross-sections retrieved from the DROSG2000 code calculations at different deuteron energies,

(8) neutron generation by the modified von Neumann rejection method,

(9) classical kinematics.

The MCNP5 source subroutines are SOURCE.F90 (coding the D slowing down in solid Ti-T target and modelling the fusion reactions), SRCDX.F90 (specific for transporting neutrons generated in SOURCE to point detectors), and six other subroutines for numeric calculus. The D-T source routines require the use of the RDUM card in the MCNP input file to specify deuteron beam energy, target thickness, T/Ti atomic fraction, beam width, and target axis coordinates.

At ENEA the last version of the D-T source model was prepared for MCNP5 on the Unix systems. The possibility to perform routine calculations on Windows systems is achieved by producing a patch file to apply to the original MCNP5 source code for Windows systems.

Some flaws have been found in the last version of the source routines. The range of the deuterons was underestimated with reference to the TRIM calculations. The problem has been found in the stopping power of the Ti-T mixture. Since the units of the data imported into the routines from TRIM tables changed from the original MCNP4B version, some parameters needed to be modified accordingly. It is now possible to ascertain that the mean average range of the deuteron ions is about 1.5 μm, about the same value given by the TRIM code.

A new condition is implemented into the source routines to terminate the Monte Carlo history when the cumulative deuteron free flight path exceeds the target thickness.

The calculation of the neutron spectra on a very fine energy binning with the original source routines showed an unphysical spike at the deuteron maximum energy, corresponding to uncollided deuterons. After discussion with M. Pillon the special treatment of the first collision was dropped and the spike disappeared.

The major new contribution to the D-T source routines involves items 7 and 9 of the list above. The use of double differential cross-sections in the ENEA code had two drawbacks. First, it was not easy to check if the data were wrong or approximate because the data section was huge. Second, the cross-section data relied on DROSG2000 Legendre coefficients, which could change according to new experimental evidence or refinement of theoretical nuclear models. The source routines are modified to reconstruct the double-differential cross-sections from tabulated reaction cross-sections and the Legendre coefficients, defined by DATA statements in the code with values as given in the ENDF/B-VII library. The results of a test calculation comparing the original source routines and the modified routines with the data from ENDF/B-VII are shown in Figure 4. The deuteron energy is 280 KeV. The other parameters are set to their standard values: the beam width is 0.7 cm, T/Ti atomic ratio is 1.5, and target thickness is 0.001 cm. The energy binning is 10 KeV. The source and the detectors are placed in the void. In the MCNP5 input file point detectors are located at different angles from 0 to 180 degrees. The slight differences between the cross-sections in last ENEA version of the source routines (labelled "enea") and the modified routines with ENDF/B-VII cross-sections (labelled "leg.") result in a small difference in the absolute yield ($\sim$5%). Except for this detail, the distributions at each angle agree very well.

For the present work the source routines are further improved to introduce the neutron relativistic kinematics as given by equations defined in the previous section. The use of relativistic kinematics results in a shift in energy, as seen from Figure 5.

The modifications above imply a revision of the SRCDX subroutine for point detectors. A cross-validation of the source model coding is performed by comparing the MCNP5 cell flux estimator ("cf") and the point detector ("pd") flux. Figure 6 shows that both tallies are consistent, except from some fluctuations in the cell flux estimator. The energy range starts at the theoretical neutron energy. The energy spread is greater in the forward direction. The shape of the neutron spectra can be explained by considering that the maximum of the ^{3}H(d, n)^{4}He integral cross-section is at 109 KeV.

To calculate the mean values of the neutron energy and the yields at different angles a MATLAB function (ACEPD.M) is developed which reads from ACEFLX output. Thanks to the newly introduced target thickness condition described above, the target thickness is progressively reduced to simulate a very thin target (0.1μ). The neutron mean energies and yields at different angles converge to the theoretical values (indicated by crosses), as shown in Figures
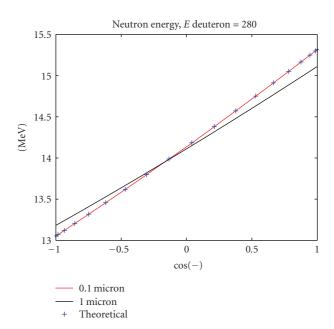
FIGURE 7: Ti target thickness effect on D-T energy-angle dependence.
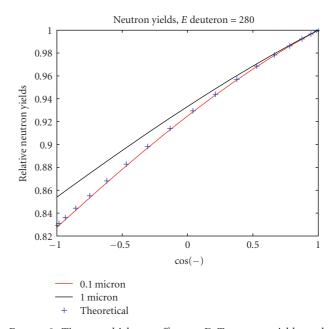
FIGURE 8: Ti target thickness effect on D-T neutron yields-angle distribution.

7 and 8. This also confirms that the random variables are properly sampled from the angular distributions.

4. THE OKTAVIAN TUNGSTEN EXPERIMENT

The OKTAVIAN facility has been devoted to perform studies on fusion neutron-related subjects by university researchers

and has also served for international collaborations. The facility was a contributor to the SINBAD Project. SINBAD declared objective is the validation and benchmarking of computer codes and nuclear data used for radiation transport and shielding problems and the preservation of a unique set of experiments for the present and future needs.

The integral experiment under consideration consisted of measurements of the neutron leakage spectra from a 40 cm diameter tungsten (W) sphere pile. W is a candidate material for the first wall of fusion reactors. In the computational models, the evaluated nuclear data for W are from the IAEA files compiled in April 2007 [5]. The source neutrons were produced by bombarding a solid Ti-T target at the centre of the W pile with a 250 KeV deuteron beam. The geometry of the MCNP5 input file is based on the available information about the experimental setup. The precollimator and the main collimator bodies are modelled whereas the simulations in the original analyses neglected them. The information on the target assembly is retrieved from the report [6] and allows only an approximate model of the accelerator structures. The results presented here tend to focus on the issues arising in the analyses of MCNP5 simulations of integral experiments and directly concerning the D-T neutron source. Three approaches to the source specifications in the MCNP5 input file are assessed.

(a) In this first approach, the monoenergetic angle-dependent yields of source neutrons are given by empirical expressions which hold for thick targets. The method is illustrated by Csikai et al. [7] and is commonly used for modelling neutron sources. For comparison with measured spectra, the calculated spectra usually need to be resolution-broadened.

(b) In the second approach, the use is made of the measured spectrum in the forward direction of the bare source, provided by the experimentalist. The source is defined by scaling the outgoing-energy and the magnitude of the measured spectrum such that the positions of the peak and the yield match the measured average values. In this way, resolution broadening and certain geometrical features (such as room-return, collimator, etc.) are implicitly taken into account. This procedure has been used by A. Trkov for the OKTAVIAN nickel sphere benchmark experiment [8].

(c) The upgraded D-T source model described in Section 2 is applied. The deuteron energy is 250 KeV, while the other parameters are left at their standard values. An equivalent source definition (in the form of the SDEF and DS cards) is prepared for users that do not wish to recompile MCNP5 with the source routines by calculating the neutron energy distributions and yields in point detectors in void at different angles. These two forms of input give the same results and are not treated separately.

The source spectra at forward angle for cases (b) and (c) are compared in Figure 9. For clarity, the plotted spectra are normalised at the peak. The scattering effects of source
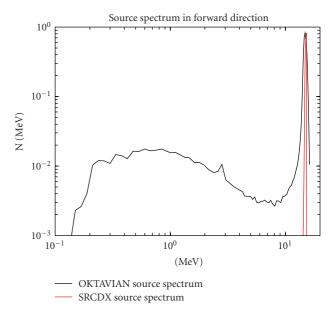
FIGURE 9: Comparison of OKTAVIAN source spectrum in forward direction versus the one generated by the SRCDX subroutine.
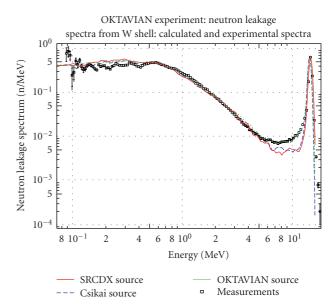
FIGURE 10: Neutron leakage spectra obtained with different source models implemented, benchmarked with the experimental measurements of OKTAVIAN W sphere test.

neutrons with the structures of the experimental setup are intrinsic to the measured response function, as can be inferred from the tail below the main peak (labelled "OKTAVIAN spectrum"). The energy spread due to the deuteron interactions inside the target as calculated by the source routine is small (labelled "SRCDX spectrum"). The calculated spectrum partly justifies the approximation in case (a), in which the energy distribution is a delta function. At other angles the source neutron distributions are similar, except for a shift in energy and the total yield.

Due to the finite resolution of the detectors, their finite size, resolution of the electronics, and so forth, some smearing in the measured spectrum is inevitable. To compare the calculated and measured spectra, the calculated ones usually have to be resolution-broadened. Assuming the applicability of the central limit theorem, the calculated spectra for cases (a) and (c) are broadened with a Gaussian resolution function. Note that resolution-broadening is not needed in case (b), because it is approximately accounted for in the source definition. The neutron leakage spectra obtained with the sources above described are compared in Figure 10. The best agreement with experimental spectrum is obtained with the recommended OKTAVIAN source. The calculated spectra at the peak agree well with the measurement. The observed discrepancy in cases (a) and (c) between 5 and 12 MeV is an indication of inadequate modelling of the detailed geometry of the experimental setup: the use of the measured response function for source definition in case (b) effectively corrects for some modelling deficiencies. Although the source in case (c) is physically better, the overall result compares worse with the measurements because it is not possible to improve the physical models of the experimental setup due to lack of information. The differences below 0.5 MeV could be due to the W nuclear data or the modelling assumptions about the surrounding structures.

5. CONCLUSIONS

The interest in the materials for nuclear fusion reactors promoted extensive research in facilities producing D-T source neutrons on small scale, as the low-voltage deuteron accelerators with Ti/T targets.

In the present work, the basic principles of the D-T fusion reaction are clarified. The calculations of the neutron energy and angular distribution are performed in the framework of relativistic kinematics. The source routines allow realistic modelling of the Ti-T target assembly, which is the starting point for the analysis of the integral experiments. The uncertainties contained in the source spectrum propagate to the neutron leakage spectrum. The analysis of the OKTAVIAN experiment showed the energy regions and the magnitude of the corresponding discrepancies which arise from the source definition and not from the nuclear data of the primary measured structural material.

In this early stage of the analysis, progress is made in establishing codes and procedures for the modelling of the D-T source neutrons. The importance of detailed and accurate specifications of the experimental setup is emphasized if integral experiments are to be used to discriminate between different sets of nuclear data.

ACKNOWLEDGMENTS

REFERENCES

[1] J. Csikai, "Production of 14 MeV neutrons by low voltage accelerators," in *Proceedings of the IAEA Consultants Meeting on Neutron Source Properties*, Vienna, Austria, March 1980, IAEA (INDC(NDS)-114-GT).

[2] Cross Section Evaluation Working Group, "ENDF- 6 formats manual," Tech. Rep. BNL-NCS-44945-05-Rev, Brookhaven National Laboratory, Upton, NY, USA, April 2004.

[3] M. Drosg, "Monoenergetic neutron production by two-body reactions in the energy range from 0.0001 to 500 MeV," in *Proceedings of the IAEA Technical Committee Meeting on Accelerator-Based Neutron Sources*, Debrecen, Hungary, October 1999.

[4] M. Angelone, M. Pillon, P. Batistoni, M. Martini, M. Martone, and V. Rado, "Absolute experimental and numerical calibration of the 14 MeV neutron source at the Frascati neutron generator," *Review of Scientific Instruments*, vol. 67, no. 6, pp. 2189–2196, 1996.

[5] R. Capote, A. Trkov, I. Kodeli, et al., "Evaluation of tungsten isotopes in the fast neutron range including cross section covariance estimation," in *Proceedings of the International Conference on Nuclear Data for Science and Technology*, Nice, France, April 2007.

[6] H. Hashikura, K. Haikawa, A. Takahashi, et al., "Neutron leakage spectra from a large iron sphere pulsed with 14 MeV neutrons," in *Proceedings of the NEA Specialists' Meeting on Shielding Benchmarks*, Saclay, France, September 1984.

[7] J. Csikai, Zs. Lantos, and Cs. M. Buczkó, "Investigations on the properties of D+D and D+T neutron sources," in *Proceedings of the Advisory Group Meeting on Properties on Neutron Sources*, Kossuth University, Leningrad, Russia, June 1986.

[8] K. Sumita, A. Takahashi, T. Kasahara, et al., "Measurements of neutron leakage spectra from 16 cm radius nickel sphere," Tech. Rep. A-84-04, OKTAVIAN, Los Angeles, Calif, USA, 1984.

Research Article

Machine Learning of the Reactor Core Loading Pattern Critical Parameters

Krešimir Trontl,[1] Dubravko Pevec,[1] and Tomislav Šmuc[2]

[1] *Department of Applied Physics, Faculty of Electrical Engineering and Computing, Unska 3, 10000 Zagreb, Croatia*
[2] *Division of Electronics, Ruđer Bošković Institute, Bijenička 54, 10002 Zagreb, Croatia*

Correspondence should be addressed to Krešimir Trontl, kresimir.trontl@fer.hr

The usual approach to loading pattern optimization involves high degree of engineering judgment, a set of heuristic rules, an optimization algorithm, and a computer code used for evaluating proposed loading patterns. The speed of the optimization process is highly dependent on the computer code used for the evaluation. In this paper, we investigate the applicability of a machine learning model which could be used for fast loading pattern evaluation. We employ a recently introduced machine learning technique, support vector regression (SVR), which is a data driven, kernel based, nonlinear modeling paradigm, in which model parameters are automatically determined by solving a quadratic optimization problem. The main objective of the work reported in this paper was to evaluate the possibility of applying SVR method for reactor core loading pattern modeling. We illustrate the performance of the solution and discuss its applicability, that is, complexity, speed, and accuracy.

1. INTRODUCTION

Decrease of the fuel cycle costs is an important factor in nuclear power plant management. The economics of the fuel cycle can strongly benefit from the optimization of the reactor core loading pattern, that is, minimization of the amount of enriched uranium and burnable absorbers placed in the core, while maintaining nuclear power plant operational and safety characteristics.

The usual approach to loading pattern optimization involves high degree of engineering judgment, a set of heuristic rules, an optimization algorithm, and a reactor physics computer code used for evaluating proposed loading patterns. Since the loading pattern optimization problem is of combinatorial nature and involves heuristics requiring large numbers of core modeling calculations (e.g., genetic algorithms or simulated annealing algorithms), the time needed for one full optimization run is essentially determined by the complexity of the code that evaluates the core loading pattern.

The aim of the work reported in this paper was to investigate the applicability of a machine learning modeling for fast loading pattern evaluation. We employed a recently introduced machine learning technique, support vector regression (SVR), which has a strong theoretical background in statistical learning theory. SVR is a supervised learning method in which model parameters are automatically determined by solving a quadratic optimization problem.

This paper reports on the possibility of applying SVR method for reactor core loading pattern modeling. Required size of the learning data set, as a function of targeted accuracy, influence of SVR free parameters, as well as input vector definition were studied.

In Section 2, the support vector regression method is discussed. Basics of fuel loading pattern development and optimization as well as the methodology applied for the investigation of applicability of the SVR method for fuel loading pattern evaluation are presented in Section 3. Results and discussion are given in Section 4, while in Section 5 the conclusions based on this work are drawn.

2. SUPPORT VECTOR REGRESSION

Machine learning is, by its definition, a study of computer algorithms that improve automatically through experience.

One of machine learning techniques is the support vector machines (SVMs) method, which has a strong theoretical background in statistical learning theory [1]. The method proved to be a very robust technique for complex classification and regression problems. Although, historically speaking, the first implementation of SVM was for classification problems [2, 3], in the last decade, the application of SVM for nonlinear regression modeling is noticeable in different fields of science and technology [4–10], the main reason being robustness and good generalization properties of the method.

In the upcoming paragraphs, we will give a short introduction into the support vector regression method, stressing only the most important theoretical and practical aspects of the technique. Additional information can be found in referenced literature.

In general, the starting point of the machine learning problem is a collection of samples, that is, points, to learn the model (training set) and a separate set to test the learned model (test set). Since we are interested in developing a regression model, we will consider a training data set, as well as testing data set, comprised of a number of input/output pairs, representing the experimental relationship between input variables ($\vec{x}_i$) and corresponding scalar output value (y_i):

$$\{(\vec{x}_1, y_1), (\vec{x}_2, y_2), \ldots, (\vec{x}_n, y_n)\} \subset \mathfrak{R}^d \times \mathfrak{R}. \tag{1}$$

In our case, the input vector defines the characteristics of the loading pattern, while the output value, also referred to as a target value, denotes the parameter of interest.

The modeling objective is to find a function $y = f(\vec{x})$ such that it accurately predicts (with ε tolerance) the output value (y) corresponding to a new input vector ($\vec{x}$), yet unseen by the model (the model has not been trained on that particular input vector) [11].
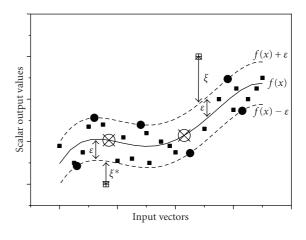
Due to the high complexity of underlying physical process that we are modeling, the required function can be expected to have high nonlinear properties. In the support vector regression approach, the input data vector $\vec{x}$ is mapped into a higher dimensional feature space F using a nonlinear mapping function Φ, and a linear regression is performed in that space. Therefore, a problem of nonlinear regression in low-dimensional input space is solved by linear regression in high-dimensional feature space.

The SVR technique considers the following linear estimation function:

$$f(\vec{x}) = \langle \vec{w}, \Phi(\vec{x}) \rangle + b, \tag{2}$$

where $\vec{w}$ denotes the weight vector, b is a constant known as bias, $\Phi(\vec{x})$ is the mapping function, and $\langle \vec{w}, \Phi(\vec{x}) \rangle$ is the dot product in feature space, such that $\Phi : \vec{x} \rightarrow F$, $\vec{w} \in F$ [12]. The unknown parameters w and b are estimated using the data points in the training set. To avoid overfitting and maximize generalization capability of the model, a regularized form of the functional, following principles of structural risk minimization (SRM), is minimized:

$$R_{\text{reg}}[f] = \sum_{i=1}^{M} C(f(\vec{x}_i) - y_i) + \lambda ||\vec{w}||^2, \tag{3}$$

Figure 1: The schematic illustration of the SVR using ε-insensitive cost function (tube).

where $R_{\text{reg}}[f]$ denotes regression risk (possible test set error), based on empirical risk which is expressed through the cost function C determined on the points of the training set, and a term reflecting the complexity of the regression model. Minimization task thus involves simultaneous minimization of the empirical risk and minimization of structural complexity of the model. Most commonly used cost function (loss functional) related to empirical risk is the so called "ε insensitive loss function":

$$C(f(\vec{x}_i) - y_i) = \begin{cases} ||f(\vec{x}) - y|| - \varepsilon, & \text{for } ||f(\vec{x}) - y|| \geq \varepsilon, \\ 0, & \text{otherwise,} \end{cases} \tag{4}$$

where ε is a parameter representing radius of the tube around regression function. The SVR algorithm attempts to position the tube around the data, as depicted in Figure 1 [7], and according to (4) does not penalize data points for which calculated values (y) lie inside this tube. The deviations of points that lie more than ε away from the regression function are penalized in the optimization through their positive and negative deviations ξ and ξ^*, called "slack" variables.

It was shown that the following function minimizes the regularized functional given by (3) [1]:

$$f(\vec{x}, \vec{w}) = f(\vec{x}, \vec{\alpha}, \vec{\alpha}^*) = \sum_{i=1}^{n} (\alpha_i^* - \alpha_i) K(\vec{x}_i, \vec{x}) + b, \tag{5}$$

where $\alpha_i^* \alpha_i$ are Lagrange multipliers describing $\vec{w}$, and are estimated, as well as parameter b, using an appropriate quadratic programming algorithm, and $K(\vec{x}_i, \vec{x})$ is a so called *kernel* function describing the dot product $\langle \vec{w}, \Phi(\vec{x}) \rangle$ in the feature space. A number of kernel functions exist [13].

Kernel functions used in this work are described in more details in the following section.

Due to the character of the quadratic optimization, only some of the coefficients $\alpha_i^* - \alpha_i$ are nonzero, and the corresponding input vectors $\vec{x}$ are called *support vectors* (SVs). Input vectors matching zero $\alpha_i^* - \alpha_i$ coefficients are positioned inside the ε tolerance tube and are therefore, not interesting for the process of model generation. Support vectors that are determined in the training (optimization) phase are the "most informative" points, that compress the information content of the training set. In most of the SVR formulations, there are two free parameters to be set by the user: C-cost of the penalty for data-model deviation, and ε-insensitive zone. These two free parameters and the chosen form of the kernel function and its corresponding parameters control the accuracy and generalization performance of the regression model.

3. METHODOLOGY

One of the key processes of both, safe and economical operations of nuclear reactor, is in-core fuel management, or to be more precise, fuel loading pattern determination and optimization. Every method and technique used for fuel loading pattern determination and optimization tasks, whether based on engineering judgement, heuristic rules, genetic algorithms, or a combination of stated approaches, requires a large number of potential fuel loading patterns evaluation. The evaluation is normally performed using a more or less sophisticated reactor physics code. Usage of such codes is time consuming. Therefore, in this work, we are investigating the possibility of SVR method being used as a fast tool for loading pattern evaluation.

However, taking into account that the SVR method is to be used, a number of factors have to be addressed prior to creating a model. The first is the setting of the loading pattern that is to be investigated, including the method by which the experimental data points are to be generated, the definition of the input space and parameters used as target values. The second is the choice of the kernel function and appropriate free parameters used in the SVR model. Finally, SVR modeling tools have to be addressed.

3.1. Computational experiment setup

Taking into account the preliminary and inquiring characteristics of the study, we decided to use limited fuel assembly inventory for a single loading pattern optimization as a basis for the development of our regression models. NPP Krško Cycle 22 loading pattern has been used as a reference one. 121 fuel assemblies, grouped in 7 batches that were used for core loading in Cycle 22 have been used for generating a large number of randomly generated fuel loading patterns, which were then divided into training and testing data sets and employed in SVR model development process. The global core calculations of each of the trial loading patterns have been conducted using MCRAC code of the FUMACS code package, which also includes the LEOPARD code for

two-group cross-section preparation [14]. The calculation is based on quarter core symmetry, fixed cycle length, and fixed soluble boron concentration curve.

The generation phase, that is, the definition of the loading patterns, has been based on a semirandom algorithm. In order to narrow the investigated input space as much as possible, as well as to stay within the limits of the numbers of available fuel assemblies per batch, we introduced a limitation for every fuel assembly regarding the position where it can be placed: fuel assemblies originally placed on axes positions could be randomly placed only on axes positions, and vice versa. The central location fuel assembly was fixed for every loading pattern.

The most important issue in the regression model development is the definition of the input space to be used for SVR model development. Since in a quarter core symmetry setup, the NPP Krško core is defined by 37 fuel assemblies, and having in mind the inquiring nature of the work, we decided to simplify the problem by the assumption of the 1/8 core symmetry, resulting in 21 fuel assemblies defining the core. Fuel assembly (position) is defined by initial enrichment, number of IFBAs, and reactor history, or at least burnup accumulated in previous cycles. Therefore, the number of potential parameters defining the input space is 63. The high dimensionality of the input space generally increases the number of training points and time required for the development of the SVR of certain generalization properties. Therefore, we decided to reduce the number of parameters by introducing k-inf at the beginning of the cycle as a new parameter and representing fuel assembly only by k-inf and number of IFBAs (0 for old fuel, and 32, 64, 92, and 116 for fresh fuel). Thus, the final number of parameters defining the input space was 42.

The SVR model would eventually be used in an optimization algorithm as a fast tool for loading pattern evaluation. Therefore, the target parameters which we want to model should be the most important parameters on which such an evaluation is based. In this work, we used the global core effective multiplication factors at the beginning and at the end of the cycle (k_{effBOC} and k_{effEOC}), as well as power peaking factor ($F_{\Delta H}^N$) as target parameters for which separate SVR models were built.

3.2. Kernel functions

The idea of the kernel function is to enable mathematical operations to be taken in the input space, rather than in the high-dimensional feature space [15]. The theory is based upon reproducing kernel Hilbert spaces (RKHSs) [16].

A number of kernel functions have been proposed in the literature. The particular choice of the kernel that is going to be used for mapping nonlinear input data into a linear feature space is highly dependent on the nature of the data representing the problem. It is up to the modeller to select the appropriate kernel function. In this paper, the focus is placed on two widely used kernel functions, namely, radial basis

function (RBF), also called Gaussian and the polynomial function (PF), which are defined by (6)

$$K_{\mathrm{RBF}}(\vec{x}_i, \vec{x}_j) = \exp\left(\frac{-\|\vec{x}_i - \vec{x}_j\|^2}{2\sigma^2}\right),$$

$$K_{\mathrm{PF}}(\vec{x}_i, \vec{x}_j) = (\vec{x}_i^T \vec{x}_j + 1)^d. \qquad (6)$$

In the case of RBF kernel, parameter σ represents the radius of the Gaussian kernel, while d in the case of PF kernel represents the degree of the polynomial kernel.

As already mentioned, the behaviour of the SVR technique strongly depends on the selection of the kernel function, its corresponding parameters, and general SVR "free" parameters (C and ε). All the parameters used in this study were determined by a combination of engineering judgement and optimization procedure based on the application of genetic algorithms [17].

3.3. SVR modeling tools

Excellent results in SVR application to a wide range of classification and regression problems in different fields of science and technology, initiated creation of a number of implementations of the support vector machines algorithm, some of which are freely available software packages. In this work, we decided to test three often used packages: SVMTorch [18], LIBSVM [19], and WEKA [20].

As stated in the previous subsection, RBF and PF kernel functions have been used. The general form of the kernels is given in (6). However, practical parameterisation of the functions, that is, their representation, is somewhat different from code to code. For example, parameter g in LIBSVM notation for RBF represents $1/(2\sigma)^2$. Whenever, a direct comparison of codes has been performed, general kernel parameters have been set (see (6)), and code specific parameters were modified to reflect on these values.

4. RESULTS AND DISCUSSION

4.1. Comparison of code packages

The comparison of three code packages for SVR modeling, namely, SVMTorch, LIBSVM, and WEKA, has been conducted using a maximum training set size of 15 000 data points while the test set consisted of 5000 data points. The number of data points for learning models is typically enlarged until satisfactory results regarding the accuracy are achieved. In this subsection, only the results of final models comparison are presented.

Preliminary analyses revealed that preprocessing of the input data is required in order to allow normal and reasonably fast operation of all SVR code packages. Mainly, due to the fact that input variables span extremely different ranges, scaling of the input data has been performed, including the scaling of the target values (all in the range 0 to 1), using one of LIBSVM codes: SVMSCALE.

Models for three target values (k_{effBOC}, k_{effEOC} and $F_{\Delta H}^N$) were compared for the model accuracy, learning and

implementation times (Pentium 4 Mobile CPU 1.7 GHz, 256 MB RAM, Windows XP SP2), and the relative number of support vectors as the measure of model generalization characteristics. The implementation time has been measured on 5000 data points. The accuracy of the model was determined using root mean square error (RMSE) and relative average deviation (RAD) defined as

$$\mathrm{RMSE} = \sqrt{\frac{\sum_{i=1}^{n}(y_i - f_i)^2}{n}},$$

$$\mathrm{RAD} = \frac{\sum_{i=1}^{n}(|y_i - f_i|/y_i) \times 100\%}{n}, \qquad (7)$$

where f_i stands for predicted value corresponding to the target value y_i. The metric of interest was also the percentage of tested data points which had the predicted value deviate from the target value by more than 20%:

$$\frac{|y_i - f_i|}{y_i} \times 100\% > 20\%. \qquad (8)$$

In the case of RBF kernel function, the initial values of free parameters were estimated using a genetic algorithm (GA) on the LIBSVM code. The ranges for every parameter (C, ε, and σ) were set, based on engineering judgement, from 1 to 1000 for C and 0.001 to 2.0, and 1 to 7.07 ($\sqrt{50}$) for ε and σ, respectively. The GA was characterized by 20 populations each consisting of 100 members. The training set consisted of 4500 data points, while the test set had 500 data points. The best result was obtained for $C = 371.725$, $\varepsilon = 0.05154$, and $\sigma = 6.4697$.

In the case of the PF kernel function, we decided to set the d parameter to the commonly used value of 3, while for simplicity reasons C and ε were set to 371.725 and 0.05154, respectively. Comparison results for RBF kernel function are given in Table 1 while in Table 2 comparison results for PF kernel function are presented.

The results of preliminary tests suggest that appropriate regression models using SVM method can be developed for all target values regardless of the applied code package. The only difference is the learning time required for the model to be developed. The implementation or deployment time for the execution of the model (maximum of 30 seconds for 5000 calculations) is not the issue. The accuracy for the k_{effBOC} and k_{effEOC} target values is satisfactory, while additional effort has to be placed on developing the $F_{\Delta H}^N$ model by adjusting SVR parameters and increasing the training set size.

4.2. Training set size influence on SVR model quality

SVR model quality can be interpreted as the time required for the model learning, accuracy of the model, and generalization characteristics of the model. As shown in the previous subsection, model implementation/deployment time is not the key issue.

As discussed previously, the size of the training set influences all factors of the model quality, and generally thorough analysis of that influence is necessary. Here, we present the results of preliminary tests conducted for

TABLE 1: Comparison of results for RBF kernel function.

Target value	Code package	Accuracy			Learning/Implem. time [s]	SV [%]
		RMSE	RAD [%]	>20%[%]		
k_{effBOC}	SVMTorch	0.029	6.793	3.44	120/14	5.27
	LIBSVM	0.029	7.179	3.96	18/3	3.59
	WEKA	0.028	6.621	3.20	2250/6	3.77
k_{effEOC}	SVMTorch	0.050	5.048	1.96	10800/30	16.69
	LIBSVM	0.045	4.550	1.76	1260/15	18.37
	WEKA	0.045	4.570	1.98	28160/30	18.22
$F_{\Delta H}^{N}$	SVMTorch	0.040	15.060	20.42	13080/13	16.91
	LIBSVM	0.039	14.810	19.64	1080/14	17.97
	WEKA	0.039	14.801	19.58	33362/14	17.86

TABLE 2: Comparison results for PF kernel function.

Target value	Code package	Accuracy			Learning/Implem. time [s]	SV [%]
		RMSE	RAD [%]	>20% [%]		
k_{effBOC}	SVMTorch	0.030	6.418	3.76	50/11	6.88
	LIBSVM	0.030	7.610	5.62	9/3	4.83
	WEKA*	0.030	6.259	3.46	4027/10	2.43
k_{effEOC}	SVMTorch	0.072	7.147	4.92	840/20	19.33
	LIBSVM	0.058	5.856	3.12	2113/11	30.21
	WEKA*	0.056	6.095	3.34	31120/45	30.02
$F_{\Delta H}^{N}$	SVMTorch	0.044	16.057	22.92	420/18	18.50
	LIBSVM	0.039	14.992	20.50	325/8	18.43
	WEKA*	0.042	15.701	22.40	7000/30	17.17

* PF kernel in the form $K_{\text{PF}}(\vec{x}_i, \vec{x}_j) = (\vec{x}_i^{\text{T}} \vec{x}_j)^d$.
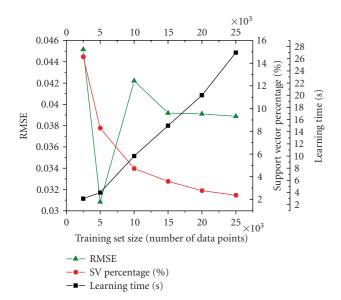
FIGURE 2: Training set size influence on model quality for k_{effBOC}-preliminary tests.

k_{effBOC} model development using LIBSVM code package (see Figure 2). The characteristics of applying other code packages on all target values are qualitatively very similar.

Apart from the anomaly observed for the RMSE curve at the training set size of 5000 data points originating in statistical and random characteristic of the training and testing data sets, the accuracy (RMSE) and the generalization properties (low SV percentage) of the models increase with the increase of the training set size. The learning time is also increased exhibiting a nearly linear trend.

5. CONCLUSIONS

This work introduces a novel concept for fast evaluation of reactor core loading pattern, based on general robust regression model relying on the state of the art research in the field of machine learning.

Preliminary tests were conducted on the NPP Krško reactor core, using the MCRAC code for the calculation of reference data. Three support vector regression code packages were employed (SVMTorch, LIBSVM, and WEKA) for creating regression models of effective multiplication factor at the beginning of the cycle (k_{effBOC}), effective multiplication factor at the end of the cycle (k_{effEOC}), and power peaking factor ($F_{\Delta H}^{N}$).

The preliminary tests revealed a great potential of the SVR method application for fast and accurate reactor core loading pattern evaluation. However, prior to the final conclusion and incorporation of SVR models in optimization

codes, additional tests and analyses are required, mainly focused on the parameters defining input vector, thus influencing its size, the required size of the training set and parameters defining kernel functions.

In the case of the scenario involving machine learning from the results of more accurate and time consuming 3D code, we do not anticipate any major changes in the learning stage of SVR model development, as well as it its implementation. However, generation of training and testing data sets would be more demanding (time consuming and requiring more hardware resources).

These are the issues that are within the scope of our future research.

REFERENCES

[1] V. N. Vapnik, *Statistical Learning Theory*, John Wiley & Sons, New York, NY, USA, 1998.

[2] E. Osuna, R. Freund, and F. Girosi, "Training support vector machines: an application to face detection," in *Proceedings of the IEEE Computer Society Conference on Computer Vision and Pattern Recognition (CVPR '97)*, pp. 130–136, San Juan, Puerto Rico, USA, June 1997.

[3] B. Schölkopf, *Support vector learning*, Ph.D. thesis, R. Oldenbourg, Munich, Germany, 1997.

[4] S. M. Clarke, J. H. Griebsch, and T. W. Simpson, "Analysis of support vector regression for approximation of complex engineering analyses," in *Proceedings of the Design Engineering Technical Conferences and Computers and Information in Engineering Conference (DETC '03)*, pp. 535–543, Chicago, Ill, USA, September 2003.

[5] T. Gu, W. Lu, X. Bao, and N. Chen, "Using support vector regression for the prediction of the band gap and melting point of binary and ternary compound semiconductors," *Solid State Sciences*, vol. 8, no. 2, pp. 129–136, 2006.

[6] E. Myasnikova, A. Samsonova, M. Samsonova, and J. Reinitz, "Support vector regression applied to the determination of the developmental age of a *Drosophila* embryo from its segmentation gene expression patterns," *Bioinformatics*, vol. 18, supplement 1, pp. S87–S95, 2002.

[7] S. Nandi, Y. Badhe, J. Lonari, et al., "Hybrid process modeling and optimization strategies integrating neural networks/support vector regression and genetic algorithms: study of benzene isopropylation on Hbeta catalyst," *Chemical Engineering Journal*, vol. 97, no. 2-3, pp. 115–129, 2004.

[8] D. J. Strauß, G. Steidl, and U. Welzel, "Parameter detection of thin films from their X-ray reflectivity by support vector machines," *Applied Numerical Mathematics*, vol. 48, no. 2, pp. 223–236, 2004.

[9] D. O. Whiteson and N. A. Naumann, "Support vector regression as a signal discriminator in high energy physics," *Neurocomputing*, vol. 55, no. 1-2, pp. 251–264, 2003.

[10] K. Trontl, T. Šmuc, and D. Pevec, "Support vector regression model for the estimation of γ-ray buildup factors for multilayer shields," *Annals of Nuclear Energy*, vol. 34, no. 12, pp. 939–952, 2007.

[11] N. Cristianini and J. Shawe-Taylor, *An Introduction to Support Vector Machines and Other Kernel-Based Learning Methods*, Cambridge University Press, Cambridge, UK, 2005.

[12] A. J. Smola and B. Schölkopf, "A tutorial on support vector regression," *Statistics and Computing*, vol. 14, no. 3, pp. 199–222, 2004.

[13] A. J. Smola, *Learning with kernels*, Ph.D. thesis, Technische Universität Berlin, Berlin, Germany, 1998.

[14] B. Petrović, D. Pevec, T. Šmuc, and N. Urli, "FUMACS (FUel MAnagement Code System)," Rudjer Bošković Institute, Zagreb, Croatia, 1991.

[15] S. R. Gunn, "Support vector machines for classification and regression," Tech. Rep., Faculty of Engineering, Science and Mathematics, University of Southampton, Southampton, UK, May 1998.

[16] N. Aronszajn, "Theory of reproducing kernels," *Transactions of the American Mathematical Society*, vol. 68, no. 3, pp. 337–404, 1950.

[17] B. Üstün, W. J. Melssen, M. Oudenhuijzen, and L. M. C. Buydens, "Determination of optimal support vector regression parameters by genetic algorithms and simplex optimization," *Analytica Chimica Acta*, vol. 544, no. 1-2, pp. 292–305, 2005.

[18] R. Collobert and S. Bengio, "SVMTorch: support vector machines for large-scale regression problems," *The Journal of Machine Learning Research*, vol. 1, no. 2, pp. 143–160, 2001.

[19] C.-C. Chang and C.-J. Lin, "LIBSVM: a library for support vector machines," Manual, 2001.

[20] I. H. Witten and E. Frank, *Data Mining: Practical Machine Learning Tools and Techniques*, Morgan Kaufmann, San Fransisco, Calif, USA, 2nd edition, 2005.

Research Article

Use of Nuclear Data Sensitivity and Uncertainty Analysis for the Design Preparation of the HCLL Breeder Blanket Mockup Experiment for ITER

I. Kodeli

OECD/NEA Data Bank, 12 boulevard des Iles, 92130 Issy-les-Moulineaux, France

Correspondence should be addressed to I. Kodeli, ivo.kodeli@oecd.org

An experiment on a mockup of the test blanket module based on helium-cooled lithium lead (HCLL) concept will be performed in 2008 in the Frascati Neutron Generator (FNG) in order to study neutronics characteristics of the module and the accuracy of the computational tools. With the objective to prepare and optimise the design of the mockup in the sense to provide maximum information on the state-of-the-art of the cross-section data the mockup was pre-analysed using the deterministic codes for the sensitivity/uncertainty analysis. The neutron fluxes and tritium production rate (TPR), their sensitivity to the underlying basic cross-sections, as well as the corresponding uncertainties were calculated using the deterministic transport codes (DOORS package), the sensitivity/uncertainty code package SUSD3D, and the VITAMINJ/ COVA covariance matrix libraries. The cross-section reactions with largest contribution to the uncertainty of the calculated TPR were identified to be (n,2n) and (n,3n) reactions on lead. The conclusions of this work support the main benchmark design and suggest some modifications and improvements. In particular this study recommends the use, as far as possible, of both natural and enriched lithium pellets for the TRP measurements. The combined use is expected to provide additional and complementary information on the sensitive cross-sections.

1. INTRODUCTION

The future fusion experimental reactor ITER will be based on the fusion reaction of deuterium and tritium (D-T reaction). Unlike deuterium which is stable and readily available in nature (oceans), tritium is a radioactive isotope with a relatively short half life of about 12.3 years and it will have to be produced in the fusion reactor plant locally. The tokamak will be therefore surrounded by lithium blanket and tritium will be produced by bombardment of lithium atoms with neutrons escaped from the D-T reaction in plasma. For tritium production (breeding), two blanket concepts are considered within the EU fusion technology programme, the helium-cooled pebble bed (HCPB) blanket with lithium ceramics pebbles (Li_4SiO_4 or Li_2TiO_3) as breeder material and beryllium pebbles as neutron multiplier, and the helium-cooled lithium-lead (HCLL) blanket with the Pb-Li eutectic alloy plays the role of breeder and neutron multiplier. Both blanket designs will use helium as coolant.

The two breeding-blanket modules are candidates for the blanket module design for a fusion power demonstration reactor (DEMO) to be constructed after ITER. To validate the engineering designs and the viability of the fusion plant, the test blanket modules (TBM) of both designs will be installed in ITER.

Tritium self-sufficiency which will be needed for DEMO reactor is still to be demonstrated, taking into account both the losses of the tritium inventory as well as the uncertainties in the tritium production. Experimental studies involving irradiation of the two proposed blanket designs were therefore undertaken at the Frascati Neutron Generator (FNG) 14 MeV facility [1–3] in cooperation between the Ente per le Nuove tecnologie, l'Energia e l'Ambiente (ENEA), Frascati; Forschungszentrum Karlsruhe (FzK); Technische Universität Dresden (TUD); and Institut Jožef Stefan, Ljubljana (IJS). NEA Data Bank also participates in this study to perform transport and sensitivity studies as well as to assure the final integration of the experimental results and
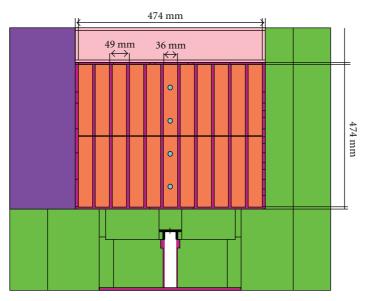
FIGURE 1: Schematic diagram of the TBM-HCLL mockup showing steel (dark red) and LiPb (orange) layers. The detectors are placed on the central axis.

their evaluation into the shielding benchmark experiments database (SINBAD) in order to make these data easily available to the international community. The objective of these experiments is to assess the uncertainty on tritium production rate (TPR) due to the uncertainty in the relevant nuclear data. The FNG experiments in particular contribute to the validation of the computational tools and nuclear data needed for the neutronics analysis. The helium-cooled pebble bed (HCPB) breeder blanket mockup benchmark experiment was performed in 2005 and consists of a metallic beryllium setup with two double layers of breeder material (Li_2CO_3 powder). The reaction rate measurements include the Li_2CO_3 pellets for the tritium breeding monitoring and activation foils, inserted at several axial and lateral locations in the block. The experiment and the results of the analysis using the Monte Carlo and deterministic transport, sensitivity, and uncertainty code system were presented in [4, 5].

The tritium breeding-module helium-cooled lithium-lead benchmark experiment (TBM HCLL) is under preparation and will be performed in 2008. The aim of the present work is the preanalysis and the optimisation of the benchmark experiments design using the deterministic transport, sensitivity, and uncertainty code system. The analysis includes the calculation of the tritium production rate (TPR) in LiPb layers and the neutron reaction rates, which will be measured in the benchmark, their sensitivity to the underlying cross-sections, as well as the corresponding uncertainty estimations. The SUSD3D cross-section sensitivity and uncertainty code package together with the two- and three-dimensional (2D/3D) deterministic transport codes DORT/TORT are used for the analysis of the experiment. Based on the sensitivity analyses, the most important nuclear reactions and energy ranges in the particular reaction rate measurements can be identified. This information will be

used to anticipate the benefits obtained from the experiment and thus guide and optimise its design and to assess the nuclear data needs.

2. TBM-HCLL EXPERIMENTAL MOCKUP

The experimental geometry which will be irradiated in the FNG facility consists of a block of 45 cm × 47.4 cm side view and 34.6 cm long, placed 5.3 cm in front of the 14 MeV FNG neutron source (Figure 1). The block is composed of 12 stainless steel layers, 0.65 cm thick each, and 3.6 cm high layers (11 in total) composed of LiPb bricks, between them. Seven detector positions are planned between 3.7 cm and 27.7 cm in the block to measure the tritium production rate (TPR) using Li_2CO_3 pellets.

The modelling of the TBM HCLL mockup geometry requires full 3D description; a 2D approximate model often used in the previous studies is not applicable. Like in the previous HCPB tritium breeder module mockup benchmark experiment, the 3D calculational procedure was used based on the following codes:

 (i) TORT [6] discrete ordinates transport code for 3D geometries,

 (ii) GRTUNCL-3D [7] code to prepare uncollided and 1st collision neutron source for TORT,

(iii) SUSD3D [8] code for the cross-section sensitivity and uncertainty analysis.

SUSD3D code performs the sensitivity/uncertainty analysis and assessment of uncertainties in calculations using discrete ordinate approach based on the first-order perturbation theory where sensitivity coefficients are derived from the direct and adjoint flux moments calculated by the discrete ordinates codes.
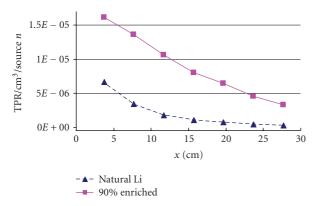
FIGURE 2: Tritium production rate for the natural and enriched Li pellets.

TABLE 1: Calculated Tritium production rates. (TORT/FENDL-2.1: S-16,P-5)

	$^{6+7}$Li(n,t) reaction rate	
Y (cm)	Natural Li	90% enriched
3.7 (P1)	$6.70 \cdot 10^{-6}$	$1.61 \cdot 10^{-5}$
7.7 (P2)	$3.46 \cdot 10^{-6}$	$1.36 \cdot 10^{-5}$
11.7 (P3)	$1.81 \cdot 10^{-6}$	$1.06 \cdot 10^{-5}$
15.7 (P4)	$1.08 \cdot 10^{-6}$	$8.06 \cdot 10^{-6}$
19.7 (P5)	$7.70 \cdot 10^{-7}$	$6.43 \cdot 10^{-6}$
23.7 (P6)	$4.93 \cdot 10^{-7}$	$4.54 \cdot 10^{-6}$
27.7 (P7)	$3.43 \cdot 10^{-7}$	$3.30 \cdot 10^{-6}$
Ratio (P7/P1)	19.5	4.9

On the other hand, the 3D calculations are much more time consuming than the 2D analyses which were used in the past, for simpler benchmarks, such as the FNG-ITER Blanket Bulk Shield, Neutron Streaming, SiC and W benchmarks modelled in 2-dimensional geometry using the codes DORT and TWODANT. TORT calculations required several days of CPU on a Linux computer, comparing to a few minutes for 2D DORT analysis. For testing and studies of different effects and computational approximations, a simpler and approximate 2-dimensional model was therefore prepared. In the case of the HCPB tritium breeder module mockup benchmark [5] the comparison of the results obtained using the 3D code system with the results of the standard well-established 2D system based on GRTUNCL/DORT/DUSD3D codes already revealed few problems and inconsistencies in the TORT/GRTUNCL-3D code system requiring some modifications in our SUSD3D sensitivity code. Consistent use of both methods contributes in this way to better confidence in the results.

The preparation of cross-section for deterministic codes is case dependent, in particular due to theself-shielding phenomena, which are of course different than those in the previous experiments and require explicit treatment. Among the available multigroup cross-section libraries for deterministic codes, the FENDL-2 and -2.1 libraries [9] are dedicated to the fusion applications and were found the most

TABLE 2: Contribution of the uncollided flux. (TORT/FENDL-2.1: S-16,P5)

	Uncollided and 1st collision contribution	
Y (cm)	$^{6+7}$Li(n,t)-natural	$^{6+7}$Li(n,t)-90%
3.7	56%	6%
7.7	37%	2%
11.7	21%	0.8%
15.7	12%	0.4%
19.7	8%	0.2%
23.7	5%	0.1%
27.7	4%	0.1%

suitable. The latest version, FENDL-2.1, was used in these analyses.

The responsefunctions from IRDF-90 to the recent IRDF-2002 [10] data were processed.

The covariance matrices of lead were needed for the uncertainty analyses in addition to those already processed for the previous experiments. The most recent data were found to be available in the ENDF/B-VI.8 evaluation and were processed using the NJOY-99 code [11].

3. RESULTS OF TRANSPORT CALCULATION

The 3D transport calculations using the TORT code required up to several days of CPU. Both direct and adjoint calculations were performed, adjoint ones being even more time consuming (~2 days runs). The calculated TPR from the ^{6}Li(n,t) and ^{7}Li(n,nt) reactions at the 7 planned detector positions are shown in Table 1 and Figure 2. The results are consistent with those reported in [1], obtained using the MCNP Monte Carlo code. Likewise the recommendation given in [1] to use enriched Li instead of the natural one is confirmed, leading to smaller gradients between the front and back detector positions and in this way assuring that the TPR is above the detector limit for the deep detector positions.

Table 2 shows, furthermore, the fraction of the TPR produced by the direct source neutrons (uncollided flux). It is shown that the uncollided flux contribution to the TPR is important in the first detector positions in case of using natural Li. This is due to the TPR from the high energy ^{7}Li(n,nt) reaction, as demonstrated in Table 3 presenting the ratio between the TPR from the reactions on ^{6}Li and ^{7}Li. In the case of enriched Li most of tritium is as expected produced by the ^{6}Li(n,t) reactions sensitive to thermal neutrons.

4. RESULTS OF CROSS-SECTION SENSITIVITY/UNCERTAINTY ANALYSIS

The cross-section sensitivity and uncertainty calculations were performed using the SUSD3D code, which requires as input quantities the direct and adjoint angular moment fluxes calculated by the discrete ordinates codes (DORT or TORT), as well as the transport cross-sections, and covariance matrices for therelevant materials and reactions.

TABLE 3: Contribution of ^{6}Li(n,t) and ^{7}Li(n,nt).

Y (cm)	^{6}Li(n,t)/$^{6+7}$Li(n,t)	
	Natural	90% enriched
3.7	19%	96%
7.7	32%	98%
11.7	48%	99%
15.7	62%	99%
19.7	69%	100%
23.7	77%	100%
27.7	80%	100%

TABLE 4: Sensitivity of the TPR to cross-sections for the detector position D7 (SUSD3D results based on the TORT 3D neutron fluxes).

^{6}Li(n,t) D7 (~27 cm)	Sensitivity (%/%)				
Reaction	^{206}Pb	^{207}Pb	^{208}Pb	^{6}Li	^{7}Li
Total	0.27	0.25	0.42	0.96	0.07
Elastic	0.16	0.16	0.37	0.004	0.06
Inelastic	0.08	0.06	0.002	$-5 \cdot 10^{-4}$	
(n,2n)	0.03	0.02	0.06		
(n,3n)	$7 \cdot 10^{-5}$	$4 \cdot 10^{-5}$	$6 \cdot 10^{-4}$		
(n,t)				0.96	0.01
(n,γ)	-0.004	-0.003	-0.001		
Uncertainty	2.1%	2.0%	6.4%	0.2%	0.1%

Both 3D and 2D sensitivity and uncertainty analyses were performed, using, respectively, fluxes calculated by the TORT code and from DORT simplified geometry calculations. Good consistency between the 2D and 3D calculations can be observed, demonstrating again that the sensitivity analyses do not require extremely precise models, which can be explained by the fact that the sensitivities are derivatives and as such relative quantities.

The sensitivities and uncertainties in the calculated TPR for two detector positions are presented in Tables 4 and 5, calculated, respectively, using 2D and 3D computational model. The sensitivities at the D2 position correspond to the use of natural and 90% enriched Li, and those at the D7 position are relevant both for case of natural or enriched Li.

Comparison of results in Tables 4 and 5 proves good consistency between the 2D and 3D calculations, as already mentioned above.

We can furthermore observe that the sensitivities to the Pb cross-sections are relatively low, below 1% of change in TPR per 1% of change in cross-section. The most sensitive reaction was found to the elastic scattering on Pb. Controversially, this is not the reaction causing the largest uncertainty, since the corresponding cross-section uncertainty is relatively low. On the other hand, the precision in the (n,2n) and (n,3n) reactions on Pb isotopes is rather low, consequently most of the overall uncertainty in the calculated TPR is caused by the uncertainty in these cross-section reactions.

TABLE 5: Sensitivity of the TPR to cross-sections for two detector positions. Both natural and 90% enriched Li were considered (SUSD3D results based on the DORT 2D neutron fluxes).

(a)

$^{6+7}$Li(n,t) Li-natural D2 (~7 cm)	Sensitivity (%/%)				
Reaction	^{206}Pb	^{207}Pb	^{208}Pb	^{6}Li	^{7}Li
Total	0.02	0.02	0.01	0.31	0.69
Elastic	0.04	0.04	0.09	1E-3	0.01
Inelastic	0.01	0.01	-0.003	-3E-4	-1E-3
(n,2n)	-0.03	-0.03	-0.08		
(n,3n)	$2 \cdot 10^{-5}$	$1 \cdot 10^{-5}$	$2 \cdot 10^{-4}$		
(n,t)				0.31	0.68
Uncertainty	0.9%	0.8%	3.0%	0.9%	0.1%

(b)

$^{6+7}$Li(n,t) Li-90% enr. D2 (~7 cm)	Sensitivity (%/%)				
Reaction	^{206}Pb	^{207}Pb	^{208}Pb	^{6}Li	^{7}Li
Total	0.29	0.25	0.50	0.97	0.06
Elastic	0.13	0.13	0.28	$3 \cdot 10^{-3}$	0.04
Inelastic	0.07	0.05	0.03	$7 \cdot 10^{-5}$	0.01
(n,2n)	0.10	0.08	0.19		
(n,3n)	$1 \cdot 10^{-4}$	$6 \cdot 10^{-5}$	$1 \cdot 10^{-3}$		
(n,t)				0.97	0.02
Uncertainty	2.0%	1.8%	9.7%	0.3%	0.1%

(c)

^{6}Li(n,t) D7 (~7 cm)	Sensitivity (%/%)				
Reaction	^{206}Pb	^{207}Pb	^{208}Pb	^{6}Li	^{7}Li
Total	0.31	0.27	0.48	0.96	0.07
Elastic	0.17	0.17	0.37	0.004	0.06
Inelastic	0.09	0.07	0.01	$-3 \cdot 10^{-4}$	
(n,2n)	0.05	0.04	0.10		
(n,3n)	$7 \cdot 10^{-5}$	$4 \cdot 10^{-5}$	$6 \cdot 10^{-4}$		
(n,t)				0.96	0.01
(n,γ)	-0.004	-0.003	-0.001		
Uncertainty	1.9%	1.8%	6.5%	0.2%	0.1%

Comparison of the sensitivities at the front detector positions (D2) for the natural and 90% enriched Li in Table 5 indicates rather large differences in the sensitivities. In particular, in case of using natural Li in the front positions the sensitivity to the (n,2n) reaction on Pb is negative, and positive in case of using enriched as well as for deep positions (both for natural or enriched Li). This has an important and very beneficial consequence for the cross-section validation studies. Use of both enriched and natural Li would provide different (and complementary) information on the cross-sections

and would contribute to validate the data at different energy ranges and for different nuclear reactions.

5. CONCLUSIONS

DORT and TORT/GRTUNCL-3D/SUSD3D computational schemes were used in the preanalysis of FNG-HCLL benchmark mock-up. The following conclusions and recommendation concerning the experimental setup can be summarised from this study.

(i) Using the ENDF/B-VI.8 covariance matrices, the uncertainties in TPR due to cross-section uncertainties were estimated to be between 5–10%. According to these covariance data the reactions (n,2n) and (n,3n) on lead were found to cause the highest uncertainty, although the corresponding sensitivities are not particularly high. The TPRs are most sensitive to the Pb elastic scattering cross-sections which are on the other hand known with much higher accuracy. Inelastic cross-sections were also found to be important for some isotopes of lead.

(ii) Large and potentially advantages differences in the sensitivities of TPR to the Pb cross-sections between natural and enriched Li pellets in the front detector positions were observed. This is due to the strong spectral-dependence of tritium production in different Li isotopes. The tritium production cross-section from ^{6}Li is high at low energies, while tritium production in ^{7}Li is a threshold reaction. In particular, in the front positions the sensitivity to the (n,2n) reaction on Pb is negative in case of using natural Li, and positive in case of using enriched Li. For deep positions the sensitivity is positive both for natural or enriched Li. This has an important and very beneficial consequence for the cross-section validation studies. Use of both enriched and natural Li would provide complementary information on the cross-sections and would permit to validate the data at different energy ranges and for different nuclear reactions. Combined use of natural and enriched Li pellets is therefore strongly recommended for the TPR measurements at the front detector positions, as far as the neutron flux level (and the experimental setup) permits it.

(iii) In addition to measurements on the axis of the experimental setup, off-axis measurements would provide additional information on the angular distributions, as well as on TPR generated at different energy spectra. The feasibility of placing the detectors at off-axis positions in the experimental setup should be investigated.

ACKNOWLEDGMENTS

REFERENCES

[1] P. Batistoni, "Design of a HCLL Mock-up for Neutronics Studies," FUS TEC MA-NE-R-015, December 2005.

[2] P. Batistoni and R. Villari, "Task TTMN-002, pre-analysis of the TBM-HCLL benchmark experiment," in *Proceedings of the JEFF/EFF Working Group Meeting*, Paris, France, May 2006.

[3] I. Kodeli, "Benchmark experiments collection and analysis: news on the SINBAD project; FNG-HCLL benchmark pre-analysis," in *Proceedings of the EFF Meeting*, November 2006, OECD/NEA, EFF-DOC-996.

[4] P. Batistoni, M. Angelone, L. Bettinali, et al., "Neutronics experiment on a helium cooled pebble bed (HCPB) breeder blanket mock-up," *Fusion Engineering and Design*, vol. 82, no. 15–24, pp. 2095–2104, 2007.

[5] I. Kodeli, "Deterministic 3D transport, sensitivity and uncertainty analysis of TPR and reaction rate measurements in HCPB breeder blanket mock-up benchmark," in *Proceedings of the International Conference on Nuclear Energy for New Europe*, Portorož, Slovenia, September 2006.

[6] W. A. Rhoades and R. L. Childs, "DOORS 3.2, one-, two-, three-dimensional discrete ordinates neutron/photon transport code system," Tech. Rep. CCC-650, Radiation Safety Information Computational Center, Oak Ridge National Laboratory, Oak Ridge, Tenn, USA, 1998.

[7] J. O. Johnson, Ed., "GRTUNCL3D, code to calculate semi-analytic first collision source and uncollided flux," Tech. Rep., Oak Ridge National Laboratory, Oak Ridge, Tenn, USA, July 2004.

[8] I. Kodeli, "Multidimensional deterministic nuclear data sensitivity and uncertainty code system: method and application," *Nuclear Science and Engineering*, vol. 138, no. 1, pp. 45–66, 2001.

[9] H. Wienke and M. Herman, "FENDL/MG-2.0 and FENDL/MC-2.0, the processed cross-section libraries for neutron-photon transport calculations, version 1," Tech. Rep. IAEA-NDS-176 Rev. 1, International Atomic Energy Agency, Vienna, Austria, February 1998.

[10] International Atomic Energy Agency, *International Reactor Dosimetry File 2002 (IRDF-2002)*, Technical Reports Series, no. 452, International Atomic Energy Agency, Vienna, Austria, 2006.

[11] R. E. MacFarlane and D. W. Muir, "The NJOY nuclear data processing system," Version 97, LA-12740-M, 1994.

Research Article

Theoretical and Numerical Study of Heat Transfer Deterioration in High Performance Light Water Reactor

David Palko and Henryk Anglart

Department of Reactor Technology, Albanova University Center, Royal Institute of Technology (KTH), 106 91 Stockholm, Sweden

Correspondence should be addressed to David Palko, palko@kth.se

A numerical investigation of the heat transfer deterioration (HTD) phenomena is performed using the low-Re k-ω turbulence model. Steady-state Reynolds-averaged Navier-Stokes equations are solved together with equations for the transport of enthalpy and turbulence. Equations are solved for the supercritical water flow at different pressures, using water properties from the standard IAPWS (International Association for the Properties of Water and Steam) tables. All cases are extensively validated against experimental data. The influence of buoyancy on the HTD is demonstrated for different mass flow rates in the heated pipes. Numerical results prove that the RANS low-Re turbulence modeling approach is fully capable of simulating the heat transfer in pipes with the water flow at supercritical pressures. A study of buoyancy influence shows that for the low-mass flow rates of coolant, the influence of buoyancy forces on the heat transfer in heated pipes is significant. For the high flow rates, buoyancy influence could be neglected and there are clearly other mechanisms causing the decrease in heat transfer at high coolant flow rates.

1. INTRODUCTION

High performance light water reactor (HPLWR) is one of the six Gen-IV reactor concepts, based on the existing boiling and pressurized water reactors. Water at high pressures ($p > 22.1$ MPa), used as a cooling medium, allows significant increase of the system thermal efficiency. As the reactor is designed to operate at supercritical pressure, there is no phase change between liquid and vapor phase and, therefore, the boiling crisis is inherently avoided. However, close to the pseudocritical point, where the thermophysical properties vary significantly, the heat transfer shows unusual behavior. Enhanced, normal, or deteriorated heat transfer regime may exist depending on the flow parameters and the applied heat flux.

In the deteriorated region, the heat transfer coefficient decreases causing the increase in wall temperature. As shown by several experiments (Shitsman [1], Kirillov et al. [2], or Ornatskij et al. [3]), the increase in wall temperature is not as rapid as in case of boiling crisis in classical light water reactors. Due to the relatively mild increase in wall temperature, the onset of HTD is not well defined. Many different definitions are used in the literature. For example, Koshizuka et al. [4] defined the onset of HTD as the following ratio:

$$D_r = \frac{\alpha}{\alpha_0} < 0.3, \tag{1}$$

where α_0 is the heat transfer coefficient calculated numerically by Jones-Launder's k-ε model using constant properties at bulk liquid temperature. Heat transfer is considered to be deteriorated when $D_r < 0.3$.

The modified Koshizuka's criterion for the onset of the HTD is frequently used. Here, α_0 is calculated using the Dittus-Boelter [5] correlation:

$$\text{Nu} = 0.023\,\text{Re}^{0.8}\text{Pr}^{0.4} \tag{2}$$

with thermophysical properties evaluated at the bulk liquid temperature. Differences in the definition of the onset of the HTD could lead to the relevant differences in its prediction. However, for the present study the exact definition is not relevant, as all the simulations are performed in the highly deteriorated region.
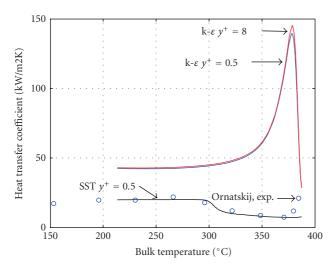
FIGURE 1: Comparison of SST turbulence model, k-ε model and experiment by Ornatskij et al. [3]. Flow conditions: $p = 25.5$ MPa, $d = 3$ mm, $G = 1500$ kg/m^{2}s, $q = 1810$ kW/m^2, vertical upward flow in a pipe.

FIGURE 2: Sensitivity analysis on the grid size for the SST turbulence model, comparison with the experiment by Ornatskij et al. [3]. Flow conditions: $p = 25.5$ MPa, $d = 3$ mm, $G = 1500$ kg/m^{2}s, $q = 1810$ kW/m^2, vertical upward flow in a pipe.

2. NUMERICAL MODELING ISSUES

The effect of buoyancy and its influence on the heat transfer is simulated numerically, using the Ansys-CFX 11.0 computational code, for steady-state flow within heated pipes. Computational domain consists of 30 degree slide of a pipe and the mesh is a standard hexahedral with approximately 2500000 grid points with refinement close to the wall, such as the nondimensional distance from the wall y^+ is below 1. All simulations which include heat transfer require proper resolution of the boundary layer. The standard k-ε turbulence model offers very robust and reliable modeling of turbulence for the bulk flow. However, for the near wall region ($y^+ < 30$), the flow is approximated by wall functions. This means that the whole viscous sublayer and part of the buffer layer is not resolved numerically with the k-ε model.

The standard k-ω turbulence model, as developed by Wilcox [6], allows resolving the viscous sublayer. However, this model is known to be sensitive to the free stream conditions. Strong variations of final results could occur depending on the value of the turbulent frequency specified at the inlet.

The shear stress transport (SST) model, as developed by Menter [7], combines the robustness of the k-ε model for the bulk flow and the low-Re treatment of the boundary layer using the modified Wilcox k-ω model.

As the validation of different cases against the experimental data proves, the low-Re SST model is fully capable of modeling the heat transfer to supercritical water (including the deteriorated region) and the calculated results are in a very good agreement with the experimental data. This is demonstrated in Figure 1, where the comparison of SST and k-ε turbulence models is shown for the experiment by Ornatskij et al. [3] (described later). The heat transfer coefficient is plotted against the bulk fluid temperature.
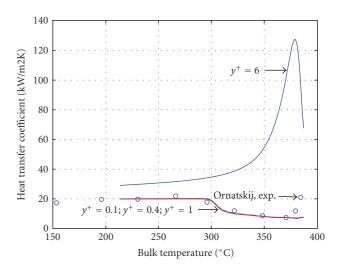
The k-ε model fails to calculate the heat transfer to supercritical fluid in deteriorated region. The SST model predicts the heat transfer coefficient in a very good agreement with the experimental results. The main reason for the substantial difference in results for these two turbulence models is the near wall treatment. SST model allows resolving the boundary layer numerically. Standard k-ε turbulence model approximates the boundary layer by wall functions (for coarse grid, $y^+ > 5$), which are not suitable for the flows where the thermophysical properties changes rapidly close to the wall. For the very fine grids ($y^+ < 1$), the nonlinear damping functions, required for the k-ε model, cause the loss of accuracy and so the final results differ substantially from the experimental values.

Sensitivity analysis for the grid size is also made for the SST model. In order to resolve the boundary layer, the nondimensional distance of the first computational cell from the wall (y^+) should be kept below 1. Figure 2 proves that if this condition is fulfilled, the results are insensitive to the grid size. This behavior results from the implementation of the wall treatment by SST turbulence model in Ansys CFX-11.0 computational software. Here, if the nondimensional distance of the first computational cell y^+ is bigger than 1, the near wall region is approximated by wall functions, which leads to the similar behavior of results as in the case of k-ε model. If the distance is smaller than $y^+ = 1$, boundary layer is resolved numerically leading to the correct solution.

3. INFLUENCE OF BUOYANCY ON HEAT TRANSFER

Once the correct numerical results are obtained, the influence of buoyancy on heat transfer could be studied by the comparison of the solution obtained with and without the buoyancy terms in the governing equations. The expected

influence of buoyancy can be examined by the ratio of Grashof and Reynolds numbers

$$\frac{\text{Gr}}{\text{Re}^2} = \frac{g\beta L \Delta T}{U^2}, \tag{3}$$

where g is the gravitational constant, β is the thermal expansion coefficient, L is the characteristic length, ΔT is the temperature change, and U is the velocity of coolant. For the normal operating conditions in the pressurized water reactors (PWRs), this ratio is small due to the very high flow velocities, relatively small change in temperature and the low value of the thermal expansion coefficient. Therefore, the buoyancy influence on heat transfer could be neglected in conditions typical for PWRs.

However, for the HPLWR conditions, even though, the flow velocity is relatively high, there is a strong change in thermophysical properties, namely, density and thermal expansion coefficient, thus the ratio of Grashof and Reynolds numbers may be relevant. It should be pointed out that the buoyancy is not the only phenomenon causing the HTD. Its influence strongly depends on the flow conditions. Several resources show that other effects, such as the streamwise acceleration (McEligot and Jackson [8]) or the direct change of the thermophysical properties (Koshizuka et al. [4]), could cause the heat transfer to deteriorate.

In the vertical pipes with upward flow, the buoyancy accelerates the flow close to the wall, where there is the highest density difference. The increase of velocity causes the decrease of the velocity gradient and thus the decrease of the turbulent kinetic energy. Loss of the turbulence close to the wall then decreases the heat transfer coefficient. In order to examine this effect, Mikielewicz et al. [9] proposed the following nondimensional number:

$$\text{Bo} = \frac{\text{Gr}^* \delta_{M+}(\nu_w/\nu_b)(\rho_w/\rho_b)^{0.5}}{2\text{Nu}_{\text{Dh}}\text{Re}_{\text{Dh}}^3(f_\tau/2)^{1.5}\text{Pr}^{0.4}} \tag{4}$$

which applies for arbitrary heated surfaces in a vertical duct (δ_{M+} is a distance near the edge of the viscous layer, Jackson [10] proposed 26). Gr^* is defined as:

$$\text{Gr}^* = g\beta q_{\text{wall}}'' D_h^4/k\nu^2. \tag{5}$$

Here, $g = 9.81\,\text{ms}^{-2}$ is the gravitational constant, ν is the kinematic viscosity, ρ is density, subscripts w and b correspond to the wall and bulk conditions, respectively, Nu_{Dh} is the Nusselt number, Re_{Dh} is the Reynolds number, Pr is the Prandtl number and f_τ is the friction factor. All of these nondimensional quantities are evaluated at bulk conditions.

According to Mikielewicz et. al. [9], $\text{Bo} > 0.1$ corresponds to the onset of significant buoyancy effects. When applying the Dittus-Boelter correlation (2) and Blasius correlation for the friction factor, (4) can be written as follows (neglecting the differences between wall and bulk densities, resp., viscosities):

$$\text{Bo}^* = \frac{\text{Gr}^*}{\text{Re}_{\text{Dh}}^{3.425}\text{Pr}^{0.8}}, \tag{6}$$

where $\text{Bo}^* = \text{Const}^*\text{Bo}$. Then the onset of significant buoyancy influence is expressed as

$$\text{Bo}^* > 6.10^{-7}. \tag{7}$$

4. NUMERICAL RESULTS AND DISCUSSION

Two different experiments are numerically simulated with Ansys CFX-11.0 computational software, using the SST turbulence model in order to examine the influence of buoyancy on the heat transfer. Experiments by Shitsman [1] and Ornatskij et al. [3] were chosen due to the following reasons.

Both experiments measure the heat transfer in the highly deteriorated region. The experiment by Ornatskij et al. [3] is performed for very high-coolant flow rate, where the buoyancy force should have no effect on the heat transfer according to (7). On the other hand, experimental data by Shitsman [1] are in the region of high-buoyancy influence.

4.1. Heat transfer at low-coolant flow rates

Flow simulation at low-coolant flow rate is demonstrated in the experiment by Shitsman [1]. This experiment is performed with supercritical water at $p = 233$ bar in a pipe with inner diameter $d = 8$ mm. The pipe is uniformly heated with a heat flux of $319.87\,\text{kW/m}^2$ and the coolant flow rate is $G = 430\,\text{kg/m}^2\text{s}$. For these flow parameters, Mikielewicz condition for the influence of buoyancy is fulfilled.

These flow conditions are modeled on a 30 degrees slice of pipe geometry with approximately 2500000 computational hexahedral cells. Boundary conditions consist of specification of constant pressure at the outlet, mass flow rate, respectively, velocity at the inlet and no slip + constant heat flux boundary conditions at the walls. Symmetry b.c is applied at the symmetry walls.

Comparison of the numerical results with the experimental data is shown in Figure 3, where the wall temperature is plotted against the bulk enthalpy. There is a very good agreement between CFX-11.0 results and experimental data. The solver is capable of capturing also the deteriorated region represented by the two peaks in the wall temperature.

Solving the same equations on an identical numerical grid without the buoyancy terms in the NS equations leads to substantial underprediction of the wall temperature. This means that the buoyancy terms in Navier-Stokes equations are responsible for the increase in the wall temperature and hence the heat transfer deterioration is caused by the buoyancy force, as was predicted by (7). A possible explanation of this phenomenon is that the buoyancy accelerates the flow close to the wall leading to the more flat velocity profile, decrease in the velocity gradient and decrease of turbulence. Decrease in turbulence then leads to the decrease of the heat transfer coefficient, and thus to the increase in wall temperature.

The Dittus-Boelter correlation (2) prediction of the wall temperature is plotted to visualize how the heat transfer regime differs from the normal regime.
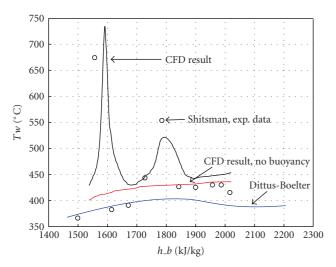
FIGURE 3: Comparison of the numerical results with the experiment by Shitsman [1] and the correlation by Dittus-Boelter. Flow conditions: $p = 23.3$ MPa, $d = 8$ mm, $G = 430$ kg/m^{2}s, $q = 319.87$ kW/m^2, vertical upward flow in a pipe.

FIGURE 4: Comparison of the numerical results with the experiment by Ornatskij [3] and the correlation by Dittus-Boelter. Flow conditions: $p = 25.5$ MPa, $d = 3$ mm, $G = 1500$ kg/m^{2}s, $q = 1810$ kW/m^2, vertical upward flow in a pipe.

4.2. Heat transfer at high coolant flow rates

For the high flow rates, when the condition Bo$^* > 6.10^{-7}$ is not fulfilled, the buoyancy could be neglected according to Mikielewicz et al. [9]. Such a flow is demonstrated by the experiment of Ornatskij et al. [3]. Here, the flow parameters of supercritical water at $p = 255$ bar are measured in a pipe with inner diameter $d = 3$ mm. The pipe is uniformly heated with heat flux of 1810 kW/m^2 and the coolant flow rate is $G = 1500$ kg/m^{2}s.

Even though the buoyancy should not be relevant, heat transfer is still deteriorated (as measured by Ornatskij et al. [3]) according to the definition:

$$D_r = \frac{\alpha}{\alpha_0} < 0.3, \qquad (8)$$

where α_0 is an ideal heat transfer coefficient calculated with the Dittus-Boelter correlation (2) with the properties evaluated at the bulk temperature.

Numerical results and the comparison with the experiment and Dittus-Boelter correlation are shown in Figure 4. The influence of buoyancy is small and there are clearly other mechanisms which cause the decrease in heat transfer. According to Koshizuka et al. [4], change in the thermophysical properties, such as viscosity and thermal conductivity, may lead to the decrease in heat transfer coefficient. The influence of these phenomena could be demonstrated in the same way as the influence of buoyancy, if numerical simulations with constant and variable properties are compared.

5. CONCLUSIONS

The present work demonstrates the ability of the low-Re RANS turbulence treatment to model the heat transfer under supercritical pressure. Proper grid resolution of the bound-

ary layer and the accuracy in thermophysical properties show very high influence on final results.

Buoyancy influence on the heat transfer deterioration was demonstrated. The results proved that under some conditions, buoyancy is the phenomenon that governs the heat transfer deterioration, mainly for relatively low coolant flow rates and high heat fluxes. However, for high coolant flow rates, there exist clearly other mechanisms which have to be identified and examined in order to be able to successfully predict the onset of HTD.

ACKNOWLEDGMENT

REFERENCES

[1] M. E. Shitsman, "Impairment of the heat transmission at supercritical pressures," *High Temperatures*, vol. 1, no. 2, pp. 237–244, 1963.

[2] P. Kirillov, R. Pomet'ko, A. Smirnov, et al., "Experimental study on heat transfer to supercritical water flowing in 1-and 4-m-long vertical tubes," in *Proceedings of the International Conference on Nuclear Energy Systems for Future Generation and Global Sustainability (GLOBAL '05)*, pp. 1–8, Tsukuba, Japan, October 2005, paper 518.

[3] A. P. Ornatskij, L. F. Glushchenko, and S. I. Kalachev, "Heat transfer with rising and falling flows of water in tubes of small diameter at supercritical pressures," *Thermal Engineering*, vol. 18, no. 5, pp. 137–141, 1971.

[4] S. Koshizuka, N. Takano, and Y. Oka, "Numerical analysis of deterioration phenomena in heat transfer to supercritical water," *International Journal of Heat and Mass Transfer*, vol. 38, no. 16, pp. 3077–3084, 1995.

[5] F. W. Dittus and L. M. K. Boelter, *Heat Transfer in Automobile Radiators of the Tubular Type*, vol. 2 of *University of California Publications in Engineering*, University of California Press, Berkeley, Calif, USA, 1930.

[6] D. C. Wilcox, "Multiscale model for turbulent flows," in *Proceedings of the 24th AIAA Aerospace Sciences Meeting*, pp. 1311–1320, American Institute of Aeronautics and Astronautics, Reno, Nev, USA, January 1986.

[7] F. R. Menter, "Multiscale model for turbulent flows," in *Proceedings of the 24th AIAA Fluid Dynamics Conference*, pp. 1311–1320, American Institute of Aeronautics and Astronautics, Orlando, Fla, USA, July 1993.

[8] D. M. McEligot and J. D. Jackson, ""Deterioration" criteria for convective heat transfer in gas flow through non-circular ducts," *Nuclear Engineering and Design*, vol. 232, no. 3, pp. 327–333, 2004.

[9] D. P. Mikielewicz, A. M. Shehata, J. D. Jackson, and D. M. McEligot, "Temperature, velocity and mean turbulence structure in strongly heated internal gas flows. Comparison of numerical predictions with data," *International Journal of Heat and Mass Transfer*, vol. 45, no. 21, pp. 4333–4352, 2002.

[10] J. D. Jackson, "Consideration of the heat transfer properties of supercritical pressure water in connection with the cooling of advanced nuclear reactors," in *Proceedings of the 13th Pacific Basin Nuclear Conference (PBNC '02)*, pp. 21–25, Shenzen City, China, October 2002.

Research Article

Simulation of Boiling Flow Experiments Close to CHF with the Neptune_CFD Code

Boštjan Končar and Borut Mavko

Reactor Engineering Division, Jožef Stefan Institute, Jamova cesta 39, 1000 Ljubljana, Slovenia

Correspondence should be addressed to Boštjan Končar, bostjan.koncar@ijs.si

A three-dimensional two-fluid code Neptune_CFD has been validated against the Arizona State University (ASU) and DEBORA boiling flow experiments. Two-phase flow processes in the subcooled flow boiling regime have been studied on ASU experiments. Within this scope a new wall function has been implemented in the Neptune_CFD code aiming to improve the prediction of flow parameters in the near-wall region. The capability of the code to predict the boiling flow regime close to critical heat flux (CHF) conditions has been verified on selected DEBORA experiments. To predict the onset of CHF regime, a simplified model based on the near-wall values of gas volume fraction was used. The results have shown that the code is able to predict the wall temperature increase and the sharp void fraction peak near the heated wall, which are characteristic phenomena for CHF conditions.

1. INTRODUCTION

In the case of offnormal operation of the pressurized water reactor (increase of coolant inlet temperature at full power and full pressure), a nucleate flow boiling on the surface of the fuel rods may occur, which influences the operating and accident conditions in several ways. The increase of vapour content due to the boiling in narrow flow passages between the fuel rods increases the pressure drop through the reactor core and reduces the moderation ability of the coolant (effect on the core reactivity). When the applied heat flux reaches the CHF value, the departure from nucleate boiling (DNB) may be observed, resulting in rapid reduction of the heat removal ability. Overheating and consequently damaging of the fuel rods may occur. A better understanding of this phenomenon is a basis for optimization of fuel elements and for planning of appropriate safety measures in the case of fuel rods overheating.

In this study, the capability of the three-dimensional code Neptune_CFD to simulate the local boiling flow processes over a wide range of operating conditions, including those close to CHF, has been assessed. This work has been carried out within the scope of NURESIM project (NUclear REactor SIMulations, 6th EURATOM FP).

The main objective of the NURESIM activity related to CHF is to use two-phase computational fluid dynamics (CFD) as a tool for understanding boiling flow processes. Numerical simulations of boiling flows up to CHF conditions should help new fuel assembly design and contribute to better local predictions of CHF phenomenon [1].

The three-dimensional two-fluid code Neptune_CFD [2] is developed within the framework of the Neptune project, financially supported by Commissariat à l'Énergie Atomique (CEA), Électricité de France (EDF), Institut de Radioprotection et de Sûreté Nucléaire (IRSN) and AREVA-NP. It has been more specifically designed for simulation of transients in nuclear power plants and it is currently used and further developed within the NURESIM project. To validate the code, relevant benchmark experiments have to be used, which provide useful local information about distributions of flow parameters (e.g., cross-sectional profiles of void fraction, phase velocities, temperature, bubbles size, etc.). Nucleate boiling processes in the subcooled boiling regime were studied on ASU experiments. Boiling flow close to CHF conditions was investigated on the selected experiments performed in DEBORA facility located at Commissariat à l'Énergie Atomique (CEA), Grenoble.

TABLE 1: ASU [3] and DEBORA [4, 5] experimental conditions.

Exp. No.	$p_{m.p.}$ (bar)	q_w (kW/m²)	G (kg/m²s)	T_{sat} (°C)	T_{inlet} (°C)
ASU1	2.69	95	568	80.5	42.7
ASU2	2.69	95	784	80.5	50.2
ASU3	2.69	116	784	80.5	50.2
DEB1 [4]	26.15	73.89	2064	86.65	68.52
DEB2 [5]	30.06	58.26	994.9	94.14	72.65
DEB3 [5]	30.06	58.26	1007.4	94.14	58.39

2. EXPERIMENTAL DATA

The ASU and DEBORA boiling flow experiments were used to validate the boiling model of the Neptune_CFD code. Considered experimental facilities differ in the geometry of the test channel (annulus, pipe) and also in working fluids. In ASU experiments the refrigerant R-113 is used, while DEBORA facility uses the refrigerant R-12 as a working fluid. Density ratios and other scaling numbers are therefore different.

The measurement section of the ASU experimental facility [3] consists of a vertical annular channel with the heated inner tube with outer diameter of 15.8 mm and insulated outer tube with inner diameter of 38.02 mm. The total length of the annulus is 3.66 m and the 2.75 m long upper part of the inner tube is heated by the direct current. The 0.91 m long lower part of the annulus is not heated. The local measurements of transversal profiles of void fraction, phase velocities, velocity fluctuations, and liquid temperature were performed at a single axial location located 1.99 m downstream from the beginning of the heated section. The measurement probes and measurement techniques used in ASU experiments are described in the original paper of Roy et al. [3].

The DEBORA experiments (performed at CEA [4, 5]) were selected to analyze boiling processes close to CHF. The refrigerant R-12 at the pressure conditions of about 30 bar has been used as the working fluid to simulate steam-water flow at pressurized water reactor (PWR) conditions. The test section consists of a vertical pipe with internal diameter of 19.2 mm, divided into three axial parts: the adiabatic inlet section (1 m length), the heated section (3.5 m length), and the adiabatic outlet section (≈ 0.5 m length). At the end of the heated section, the radial profiles of void fraction, gas velocity, and bubble diameter were measured by the optical probe. ASU and DEBORA experimental conditions are presented in Table 1.

3. PHYSICAL MODELLING IN THE NEPTUNE_CFD CODE

The basic model of Neptune_CFD is the classical six-equation two-fluid model together with k-ε transport equations used for modelling of the liquid phase turbulence [2]. The version V.1.0.6 has been used to perform numerical simulations. Only some most relevant models and new model improvements used for the computations presented in this study are described.

3.1. Turbulence modelling

The turbulent stress tensor for the liquid phase is modelled using the Boussinesq approximation

$$
\begin{aligned}
\underline{\tau}_l^{\text{turb}} &= -\rho_l \left\langle \vec{u}_l' \vec{u}_l' \right\rangle \\
&= \mu_l^{\text{turb}} \left(\nabla \vec{u}_l + \left(\nabla \vec{u}_l \right)^T \right) - \frac{2}{3} \underline{I} \left(\rho_l k_l + \mu_l^{\text{turb}} \nabla \cdot \vec{u}_l \right),
\end{aligned}
\tag{1}
$$

where $\vec{u}_l'$ is the fluctuating part of liquid velocity, $\vec{u}_l$ is the liquid velocity in axial direction, k_l is the turbulent kinetic energy of liquid phase $k_l = 0.5 \langle \vec{u}_l' \vec{u}_l' \rangle$, $\underline{I}$ is identity tensor, and μ_l^{turb} is the eddy viscosity

$$
\mu_l^{\text{turb}} = C_\mu \rho_l \frac{k_l^2}{\varepsilon_l}.
\tag{2}
$$

Eddy viscosity in (2) is defined by the turbulent kinetic energy k_l and its dissipation rate ε_l, both calculated from the two-equation k-ε model. Parameter C_μ is set to 0.09. The effect of wakes behind the bubbles on the liquid turbulence is taken into account by additional terms in k-ε transport equations. These additional source terms represent the turbulent contribution of the gas phase on liquid and are modelled as follows [4]:

$$
\begin{aligned}
S_l^k &= -\left(\vec{M}_D + \vec{M}_{AM} \right) \cdot \left(\vec{u}_g - \vec{u}_l \right), \\
S_l^\varepsilon &= C_{\varepsilon 3} \frac{S_l^k}{\tau},
\end{aligned}
\tag{3}
$$

where $\vec{M}_D$ and $\vec{M}_{AM}$ are interfacial drag and added mass volumetric forces and τ is a characteristic time for bubble induced turbulence, which depends on bubble departure diameter d_b and dissipation rate ε_l:

$$
\tau = \left(\frac{d_b^2}{\varepsilon_l} \right)^{1/3}.
\tag{4}
$$

3.2. Interfacial transfer terms

The interfacial transfer of momentum is modelled by interfacial forces per unit volume, which include drag force

$\vec{M}_D$, added mass force $\vec{M}_{AM}$, lift force $\vec{M}_L$, and turbulent dispersion force $\vec{M}_{TD}$. The interfacial drag force is calculated according to the Ishii correlation [6] and the added mass force is calculated by Zuber model [7]. Turbulent dispersion force, which considers the diffusion of the vapour phase due to the liquid phase turbulence, is calculated as

$$\vec{F}_{TD} = -C_{TD}\rho_l k_l \nabla \alpha, \qquad (5)$$

where C_{TD} is the turbulent dispersion coefficient.

The bubble diameter in the bulk d_b determines the interfacial momentum transfer and interfacial heat and mass transfer. In the present work, constant values for bubble diameter have been used. The approximate values (1.2 mm for ASU and 0.3 mm for DEBORA experiments) were estimated from the available experimental data. The interfacial heat and mass transfer due to condensation in the subcooled bulk flow is modelled by Ranz-Marshall correlation [8]. Description of mass and heat transfer models is given in the code manual [2].

3.3. Wall to fluid transfer model at conditions close to CHF

To take into account the phenomenon of temperature excursion at CHF conditions, the standard heat flux partitioning model of Kurul and Podowski [9] is extended by additional heat transfer to the gas phase. To distribute the wall heat flux between different phases, a phenomenological function $f_{\alpha 1}$ is introduced. The function $f_{\alpha 1}$ depends on liquid volume fraction α_1 and takes care of the numerically smooth transition between nucleate boiling regime and DNB regime. In the Neptune_CFD, the transition to DNB regime is determined by an arbitrary value for liquid volume fraction in the near-wall cell, set to $\alpha_{1cr} = 0.2$

$$
\begin{aligned}
f_{\alpha 1} &= 1 - 0.5 \cdot \exp\left[-20(\alpha_1 - \alpha_{1cr})\right] \quad \text{for } \alpha_1 \geq \alpha_{1cr}, \\
f_{\alpha 1} &= 0.5 \cdot \left(\frac{\alpha_1}{\alpha_{1cr}}\right)^{20 \cdot \alpha_{1cr}} \quad \text{for } \alpha_1 < \alpha_{1cr}.
\end{aligned}
\qquad (6)
$$

The wall heat flux is then split into four different components

$$\Phi_w = f_{\alpha 1}(\Phi_{C1} + \Phi_Q + \Phi_E) + (1 - f_{\alpha 1})\Phi_{C2}, \qquad (7)$$

where Φ_{C1} denotes the single-phase convection heat flux to the liquid, Φ_Q denotes quenching heat flux that transfers cold liquid from the bulk flow to the wall periodically, Φ_E is the heat flux component needed to generate vapor bubbles, and Φ_{C2} denotes the heat flux used to preheat the vapor phase in the DNB regime. The first three heat flux components are extensively described in the code manual [2] and in our previous references [10, 11]. The convective heat flux to the vapor phase Φ_{C2} is modelled by a single-phase heat transfer at the wall:

$$\Phi_{C2} = h_{\log}^g (T_w - T_g), \qquad (8)$$

where $h_{\log}^g$ is the convective heat transfer coefficient in the laminar regime [2], T_w is the wall temperature, and T_g is the temperature of the vapor phase. In the case of standard nucleate boiling model the function $f_{\alpha 1}$ is equal to one, leading to zero value of Φ_{C2}. The proposed approach does not have the ambition to predict the CHF triggering mechanism, but it is a promising attempt how to model the transition to DNB conditions. Local CHF triggering mechanisms are much more complex and depend on the microscale conditions, which cannot be resolved by CFD codes. Recently, Le Corre and Yao [12] have proposed a high resolution CHF model based on local wall hot spot mechanism, which has a potential to bridge the gap between local modelling of CHF mechanisms and implementation in the CFD codes.

3.4. Two-phase wall law for boiling flows

At nucleate flow boiling, the liquid velocity profile in the boiling boundary layer is significantly disturbed by the bubble formation and detachment mechanisms on the heated wall. The use of single-phase log law for boiling flow calculations may lead to significant overprediction of liquid and gas velocities in the boundary region near the heated wall [10, 13, 14]. In our previous work, [10] a modified wall law following the formulation of Ramstorfer et al. [15] has been proposed. The main idea of the new wall function is that nucleating bubbles on the wall disturb the boundary layer flow in a similar way as the surface roughness. As a basis, a logarithmic law for turbulent flows over rough walls is used:

$$u^+ = \frac{1}{\kappa}\ln(y^+) + B - \Delta u^+, \qquad (9)$$

where velocity $u^+ = u_t/u_w$ and distance from the wall $y^+ = \rho_l u_w \Delta y/\mu_l$ are written in nondimensional wall units scaled by wall friction velocity $u_w = \sqrt{\tau_w/\rho_l}$ (τ_w is the wall shear stress). Here u_t is the known velocity tangential to the wall and Δy is the distance from the wall. Coefficients κ and B are standard single-phase constants with the values of 0.41 and 5.3, respectively. The last term in (9) represents the offset of u^+ due to the wall roughness:

$$\Delta u^+ = \begin{cases} \frac{1}{\kappa}\ln(1 + C_{kr}k_r^+), & k_r^+ > 11.3, \\ 0, & k_r^+ \leq 11.3, \end{cases} \qquad (10)$$

where C_{kr} is a roughness constant, which depends on the type of roughness ($C_r = 0.5$ for sand-grain roughness) and k_r^+ is the roughness Reynolds number:

$$k_r^+ = \frac{\rho_l k_r u_\tau}{\mu_l}. \qquad (11)$$

The quantity k_r represents the physical roughness height of the surface. For $k_r^+ > 11.3$, the wall is considered to be smooth, otherwise the wall is rough. Although Ramstorfer et al. [15] have studied the flow boiling in a horizontal channel this type of log-law may be applied to all boiling flows where the flow motion along the wall is dominant.
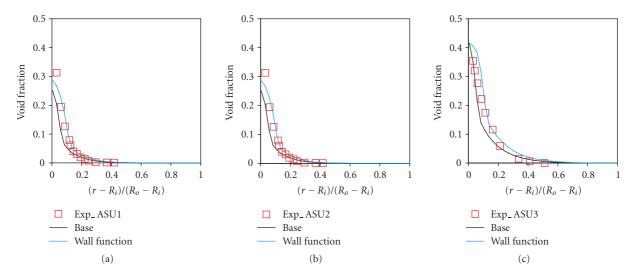
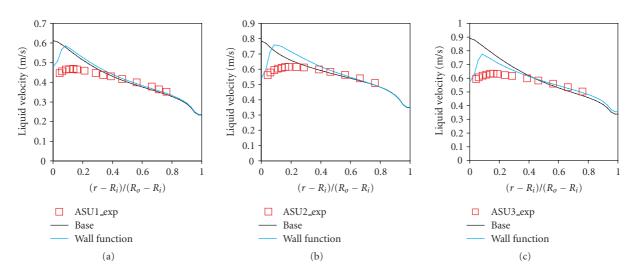FIGURE 1: ASU experiments: void fraction profile.

FIGURE 2: ASU experiments: liquid velocity profile.

The model assumes that the roughness height can be represented by a functional dependence on the bubble departure diameter d_{bw} and by the contribution of nucleate boiling heat flux q_{nb} to the total heat flux q_w:

$$k_r = \eta d_{bw} \left(\frac{q_{nb}}{q_w} \right)^{\varsigma} = \eta d_{bw} \left(1 - \frac{q_{1\phi}}{q_w} \right)^{\varsigma}. \tag{12}$$

In this study, bubble departure diameter is calculated according to extended Unal model [14]. The ratio of the nucleate boiling component to the total heat flux Φ_{nb}/Φ takes into account the thickening of the boiling boundary layer with increasing boiling activity. The coefficients η and ζ in (12) are empirical parameters set to the values $\eta = 0.5$ and $\zeta = 0.174$ for the considered experimental cases. The proposed "boiling" law of the wall is implemented

in the Neptune_CFD code in the form of blended linear-logarithmic wall function as follows:

$$u^+ = \min \left(y^+, \frac{1}{\kappa} \ln \left(y^+ \right) + B - \Delta u^+ \right). \tag{13}$$

From this wall law the wall friction velocity is computed, which is used as a "near-wall" boundary condition for the liquid momentum equations.

4.   RESULTS

Experiments presented in Table 1 were simulated. The calculations for ASU and DEBORA experiments were performed on 2D numerical meshes (19×220 for ASU and 20×220 for DEBORA), where the lower number denotes the number of cells in radial direction. These meshes were selected as a reasonable compromise between the numerical accuracy and the computational effort [4, 10].
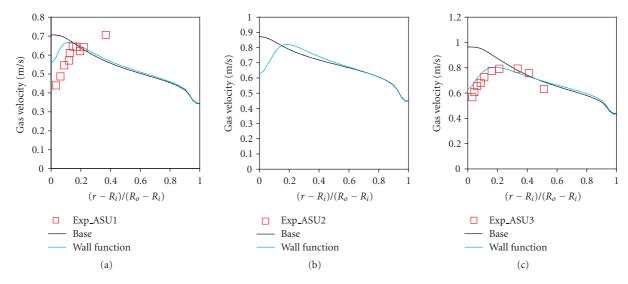
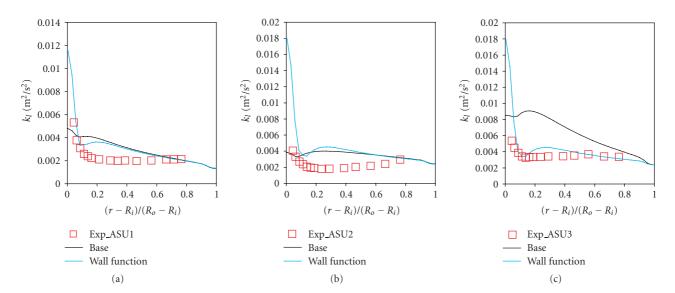Figure 3: ASU experiments: gas velocity profile.

Figure 4: ASU experiments: turbulent kinetic energy profile.

The heat transfer regime in ASU experiments is sub-cooled nucleate boiling, significantly below the CHF conditions. In this regime local nucleate boiling processes governing the lateral distribution of flow parameters were studied. In Figures 1 to 5 two different Neptune_CFD calculations are validated against ASU experiments. The calculations differ in wall function models. The "base" calculation uses standard single-phase law of the wall, whereas "wall func" calculation uses modified wall function model as described in Section 3.4. Other models, described in Section 3, are the same for both calculations.

Radial void fraction profiles are shown in Figure 1. The "wall func" simulation predicts somewhat wider boiling region comparing to the base calculation. The calculation of the axial gas velocity depends on the model for interfacial drag and interfacial area density (e.g., bubble size) whereas the axial liquid velocity profile in the wall boundary layer mainly depends on the wall friction, determined by the velocity wall function. Other influencing parameters are nondrag forces. The liquid and gas axial velocities are compared in Figures 2 and 3. The "base" calculation significantly overpredicts measured phase velocities for all experimental cases. In the calculation with the new wall function model, the liquid velocity adjacent to the wall is significantly decreased and is closer to the measured data, but overprediction somewhat away from the wall is still notable. Due to the coupling through the interfacial drag, a similar trend of decreased velocity near the heated wall may be observed also for the gas phase (Figure 3). In this case, the agreement between the "wall func" calculation and experiments is significantly improved over the entire gas velocity profile.
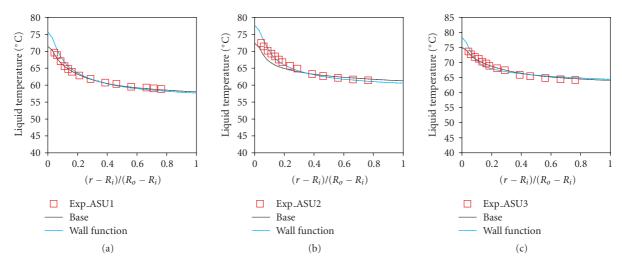
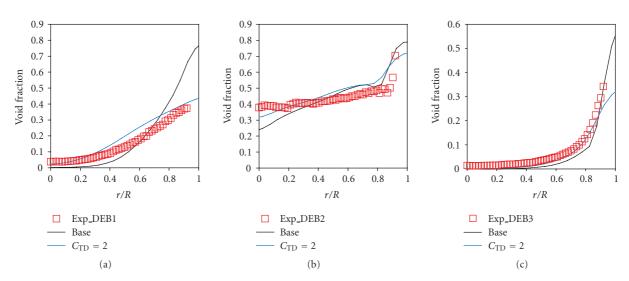Figure 5: ASU experiments: liquid temperature.

Figure 6: DEBORA experiments: void fraction profile.

Turbulent kinetic energy profiles are presented in Figure 4. The measurements showed that turbulent kinetic energy is the highest in the boiling region near the inner wall and then rapidly decreases towards centre of the channel. This trend was not adequately reproduced by the "base" calculation, whose k_l profile tends to be more gradual. The "base" calculation also significantly overpredicts the k_l values for ASU3 experiment. The "wall func" calculation gives improved prediction of the k_l profile for the experiment ASU3 over the entire channel cross-section but still overestimates measured data for the other two experiments. Due to the new wall function model, the calculated values of k_l are very high near the wall. In spite of discrepancies between the measured and simulated results, "wall func" calculations and measurements show similar trend-most of the turbulent kinetic energy production occurs in the boiling region close to the inner wall.

The liquid temperature profiles are compared in Figure 5. For both calculations, a reasonable agreement with exper-

iments may be observed for all cases. The temperature profile is somewhat steeper in the case of "wall func" calculation.

The simulation results for DEBORA experiments are presented in Figures 6, 7, 8, and 9. The calculation denoted as "base" includes the models described in Section 3; the wall function is standard single-phase log law. In the calculation "$C_{TD} = 2$," the turbulent dispersion coefficient C_{TD} in (4) is increased to the value of 2. Three different experimental cases (see Table 1) with significantly different operating conditions are simulated. According to the measured void fraction profile, the experiment DEB2 is supposed to be close to DNB, since a sharp increase of void fraction is observed near the heated wall. Radial void fraction profiles in Figure 6 are best predicted by the modified calculation with turbulent dispersion coefficient, though the profiles are smoother and underpredict the near-wall values. Especially in the case of DEB1 experiment, the "base" calculation strongly overpredicts measured void fraction on
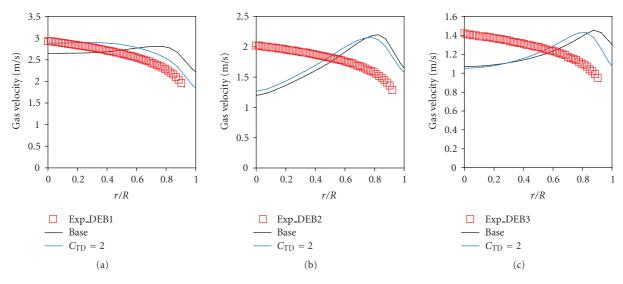
FIGURE 7: DEBORA experiments: gas velocity profile.
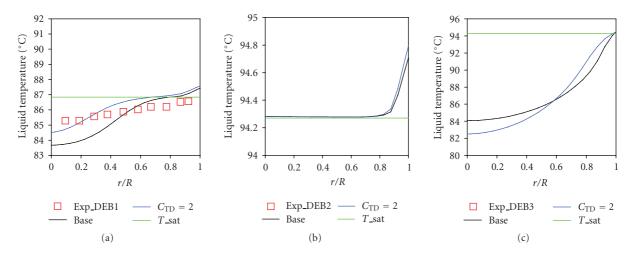
FIGURE 8: DEBORA experiments: liquid temperature profile.

the heated wall, whereas the calculated void fraction in the centre of the pipe is too low. Both calculations are able to predict a void fraction jump near the wall at DEB2 experiment.

Gas velocity profiles are presented in Figure 7. In general, both calculations tend to overpredict the measured gas velocities in the near-wall region. A better agreement can be observed in for DEB1 experiment, which has a higher mass flow rate and heat flux than the other two experiments. The experiments DEB2 and DEB3 differ only in the inlet temperature. The simulations with increased C_{TD} give profiles closer to measured data. The measured liquid temperature profile is available only for DEB1 experiment. Like in the case of other flow parameters, the calculation with increased C_{TD} predicts smoother temperature profiles closer to experimental data.

Distribution of heat flux components for DEB2 case is presented in Figure 9. Heat fluxes are multiplied by function $f_{\alpha1}$ according to (6). The liquid single-phase convection

component Φ_{C1} decreases with increasing evaporation heat flux Φ_E. Towards the end of the heated channel the convective heat flux to the gas phase Φ_{C2} is activated, which denotes the onset of CHF conditions. According to (6), the incipience of CHF is defined by function $f_{\alpha1}$ and predefined near-wall void fraction value 0.8 (Figure 10). Although the wall temperature shows fluctuating behavior along the wall after the onset of CHF, the temperature excursion at CHF is fair predicted (Figure 10).

5. CONCLUSIONS

The set of ASU and DEBORA boiling flow experiments have been calculated with the version V1.0.6 of the Neptune_CFD code. The distribution of flow parameters in the subcooled boiling regime was studied on ASU experiments. Within this scope, a new wall function model based on the

FIGURE 9: DEBORA experiments: distribution of heat flux components.

FIGURE 10: DEBORA experiments: axial distribution of near-wall void fraction, $f_{\alpha 1}$, wall temperature, saturation temperature.

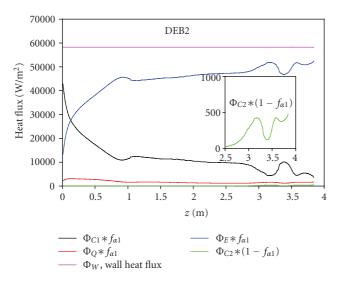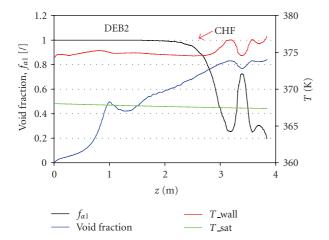surface roughness analogy has been implemented, leading to improved agreement of flow parameters with measured data.

The capability of the code to predict boiling flow phenomena close to CHF conditions was tested on the selected DEBORA experiment. Though the simplified model for the onset of CHF was used, it was demonstrated that the code is able to predict the wall temperature increase and the sharp void fraction peak characteristic for CHF conditions. However, it should be emphasized that more generic CHF criteria based on physical mechanisms need to be developed. Further investigations of critical heat flux mechanisms are therefore necessary, both experimentally and numerically.

ACKNOWLEDGMENTS

REFERENCES

[1] D. Bestion, D. Caraghiaur, H. Anglart, et al., "Deliverable D2.2.1: Review of the Existing Data Basis for the Validation of Models for CHF," NURESIM-SP2-TH D2.2.1., 2006.

[2] J. Laviéville, E. Quemerais, S. Mimouni, M. Boucker, and N. Mechitoua, Neptune CFD V1.0 Theory Manual, EDF, 2005.

[3] R. P. Roy, S. Kang, J. A. Zarate, and A. Laporta, "Turbulent subcooled boiling flow—experiments and simulations," *Journal of Heat Transfer*, vol. 124, no. 1, pp. 73–93, 2002.

[4] C. Morel, W. Yao, and D. Bestion, "Three dimensional modelling of boiling flow for the Neptune code," in *Proceedings of the 10th International Topical Meeting on Nuclear Reactor Thermal Hydraulics (NURETH '03)*, Seoul, Korea, October 2003.

[5] J. Garnier and F. François, DEBORA data bank (CD), 2006.

[6] M. Ishii and N. Zuber, "Drag coefficient and relative velocity in bubbly, droplet or particulate flows," *AIChE Journal*, vol. 25, no. 5, pp. 843–855, 1979.

[7] N. Zuber, "On the dispersed two-phase flow in the laminar flow regime," *Chemical Engineering Science*, vol. 19, no. 11, pp. 897–917, 1964.

[8] W. E. Ranz and W. R. Marshall Jr., "Evaporation from drops—part I," *Chemical Engineering Progress*, vol. 48, no. 3, pp. 141–146, 1952.

[9] N. Kurul and M. Z. Podowski, "Multidimensional effects in forced convection subcooled boiling," in *Proceedings of the 9th International Heat Transfer Conference*, vol. 2, pp. 21–26, Jerusalem, Israel, August 1990.

[10] B. Končar and E. Krepper, "CFD simulation of convective flow boiling of refrigerant in a vertical annulus," *Nuclear Engineering and Design*, vol. 238, no. 3, pp. 693–706, 2008.

[11] B. Končar, E. Krepper, and Y. Egorov, "CFD modelling of subcooled flow boiling for nuclear engineering applications," in *Proceedings of the International Conference on Nuclear Energy for New Europe*, Bled, Slovenia, September 2005.

[12] J. M. Le Corre and S. C. Yao, "A mechanistic model of critical heat flux under subcooled flow boiling conditions for application to one and three-dimensional computer codes," in *Proceedings of the 12th International Topical Meeting on Nuclear Reactor Thermal Hydraulics (NURETH '07)*, Pittsburgh, Pa, USA, September-October 2007.

[13] B. Končar, B. Mavko, and Y. A. Hassan, "Two-phase wall function for modeling of turbulent boundary layer in subcooled boiling flow," in *Proceedings of the 11th International Topical Meeting on Nuclear Reactor Thermal Hydraulics (NURETH '05)*, Avignon, France, October 2005.

[14] C. Morel, S. Mimouni, J. M. Laviéville, and M. Boucker, "R113 boiling bubbly flow in an annular geometry simulated with the Neptune code," in *Proceedings of the 11th International Topical Meeting on Nuclear Reactor Thermal Hydraulics (NURETH '05)*, Avignon, France, October 2005.

[15] F. Ramstorfer, B. Breitschädel, H. Steiner, and G. Brenn, "Modelling of the near-wall liquid velocity field in subcooled boiling flow," in *Proceedings of the ASME Summer Heat Transfer Conference (HT '05)*, vol. 2, pp. 323–332, San Francisco, Calif, USA, July 2005.

Research Article

CFD Code Validation against Stratified Air-Water Flow Experimental Data

F. Terzuoli, M. C. Galassi, D. Mazzini, and F. D'Auria

Department of Mechanics, Nuclear, and Production Engineering, University of Pisa, Via Diotisalvi 2, 56126 Pisa, Italy

Correspondence should be addressed to F. Terzuoli, f.terzuoli@ing.unipi.it

Pressurized thermal shock (PTS) modelling has been identified as one of the most important industrial needs related to nuclear reactor safety. A severe PTS scenario limiting the reactor pressure vessel (RPV) lifetime is the cold water emergency core cooling (ECC) injection into the cold leg during a loss of coolant accident (LOCA). Since it represents a big challenge for numerical simulations, this scenario was selected within the European Platform for Nuclear Reactor Simulations (NURESIM) Integrated Project as a reference two-phase problem for computational fluid dynamics (CFDs) code validation. This paper presents a CFD analysis of a stratified air-water flow experimental investigation performed at the Institut de Mécanique des Fluides de Toulouse in 1985, which shares some common physical features with the ECC injection in PWR cold leg. Numerical simulations have been carried out with two commercial codes (Fluent and Ansys CFX), and a research code (NEPTUNE CFD). The aim of this work, carried out at the University of Pisa within the NURESIM IP, is to validate the free surface flow model implemented in the codes against experimental data, and to perform code-to-code benchmarking. Obtained results suggest the relevance of three-dimensional effects and stress the importance of a suitable interface drag modelling.

1. INTRODUCTION

The European Platform for Nuclear Reactor Simulations (NURESIM) Integrated Project aims at developing a common European Standard Software Platform for modelling, recording, and recovering computer simulation data for current and future nuclear reactor systems [1]. NEPTUNE [2] is the thermal-hydraulics tool of NURESIM, and is designed to simulate two-phase flow in all situations encountered in nuclear reactor power plants. The present work is aimed at the validation and benchmarking of NEPTUNE_CFD, the two-phase CFD tool of the NEPTUNE platform [3, 4].

Since PTS has been identified as one of the most important aspects related to nuclear reactor safety, some relevant PTS scenarios were chosen as reference test cases for CFD code validation within the NURESIM IP [5, 6]. A severe PTS scenario limiting the reactor pressure vessel (RPV) lifetime is the cold water emergency core cooling (ECC) injection into the cold leg during a loss of coolant accident (LOCA). Complex phenomena take place during this scenario, such as turbulent mixing in the jet region

and downstream of the impingement zone, stratified two-phase flows, phase change at the steam water interface. This paper deals with the study of a stratified air-water flow experiment performed at the Institut de Mécanique des Fluides de Toulouse in 1985 [7, 8]; this flow configuration is likely to share common physical features with the chosen PTS scenario.

To validate the two-phase models implemented in NEPTUNE_CFD V1.0.6, numerical simulation results were compared with both experimental data and predictions from two commercial CFD codes, namely, ANSYS CFX 10.0 and FLUENT 6.1.

2. EXPERIMENTAL FACILITY AND TESTS

The experimental facility (see Figure 1) consists of a quasi-horizontal channel with rectangular cross-section (0.1 m high, 0.2 m wide, and 13.0 m long), with an inclination of 0.1° with respect to the horizontal plane. The rectangular channel is connected to the water and air inlet and outlet volumes. Desired mass flow rates are granted by a recirculation pump and all the facility walls are adiabatic.
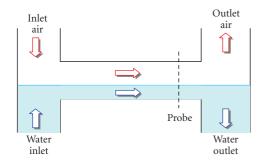
FIGURE 1: Experimental facility—conceptual scheme.

The facility is equipped with sensors located at 7.05 m, 9.10 m, and 11.10 m from the inlet section, which provide the measurements of mass flow rates, local instantaneous water height (by capacitance wire sensors), local mean and fluctuating values of horizontal and vertical velocity components, as well as Reynolds stress tensor (by a laser Doppler anemometer in water and by hot wire anemometer in air). Documentation is available [7] for three test cases conducted at ambient pressure and temperature, characterized by constant water mass flow rate and different air mass flow rates. This work deals only with one of these tests, namely, the "T250" experiment, in which water and air bulk velocities are 0.395 m/s and 3.66 m/s, respectively. Under this condition, mean water depth is measured to be 38 mm.

3. EXPERIMENTAL TEST SIMULATION WITH ANSYS CFX AND FLUENT

3.1. Preliminary results of two-phase calculations

Since the width of the duct is large compared to the height, a two-dimensional velocity field has been assumed in order to perform preliminary calculations. These analyses, carried out with the ANSYS CFX 10.0 code [9], adopted a 1-mm wide one-cell thick grid since it does not allow assuming a real two-dimensional domain. A spatial discretization of the channel has been created using ANSYS ICEM CFD 10.0 code, counting $\sim$20 k hexahedral elements ($\sim$40 k computational nodes). Elements refinement has been provided near the walls and at the expected height of interface between fluids; anyway it is worth noting that in more realistic applications, the interface is moving in the domain, so that such grid refinement could be obtained only with dynamic meshing adaptation.

The "inhomogeneous" two-phase flow model was selected, since some interface instability has been observed in all preliminary simulations. This model solves one velocity field for each phase (resulting in two different coexisting fields in the domain); while the "homogeneous" setting has been adopted for turbulence together with the k-ω shear-stress transport (SST) model, providing only one field shared by the phases. Moreover, the code default interface treatment model has been used, the so-called "standard free surface" [9].

A uniform velocity for both air and water has been assumed at the inlet. Air constant pressure and water hydrostatic profile have been imposed at the outlet section according to measured water height. Finally, adiabatic upper and lower walls with no slip and symmetric lateral faces of the domain have been selected.

Figure 2 shows the calculated velocity in the test section compared with experimental data. Air-water stratification has been correctly predicted, but relevant differences can be observed: water level is calculated about 24% lower, while the maximum air velocity is reduced by 10% and it is no longer placed between the top wall and the interface (66 mm), but closer to the wall (81 mm, $\sim$20% higher). These relevant mismatches suggest that the modelling of the frictional drag between the phases is overestimated, and a deeper understanding of the experimental data is needed. In order to investigate these problems, single-effect analyses have been carried out as described in the following Sections, together with some sensitivity analyses on the most relevant parameter.

3.2. Experimental data understanding

All performed experimental tests assume the same value of water flow rate. Different water heights are measured into the channel depending on the different equilibrium conditions between the forces acting on the fluids, that is, the drag force between air and water, the longitudinal component of the gravitational force due to the inclination of the duct, and the friction forces acting on walls. Except for the gravitational force, the others depend on fluid velocity, thus changing their values flowing into the channel: the drag force increases while the interface friction force decreases up to reaching the equilibrium condition. An incorrect prediction of one of them can justify the mismatch between calculated profiles and experimental data.

Furthermore, it is worth noting that water average velocity resulting from measured data at probe section (calculated by means of the trapezes rule, thus underestimating the real value) is >4% greater than the value provided in [7] for the water bulk velocity. The same occurs for the air. Since the flow rate is constant along the channel, this mismatch could be due to the development of a 3D profile. In fact, in a real 3D geometry, the velocity profile measured at the symmetry plane (as shown in all the plots) is the maximum profile of a developed 3D flow (see Figure 3). It is possible to conclude that considering a 2D computational domain implies a loss of information related to the flow development.

3.3. Single-phase analysis

In this analysis, the computational domain was splitted into two separate parts along the experimental interface level. Spatial discretizations have been created for each phase channel in both two- and three-dimensional configurations. Different node distributions have been employed to evaluate the grid requirements for CFD simulation to correctly reproduce near-wall effect and flow developing. The most relevant grid details are reported in Table 1 for both FLUENT
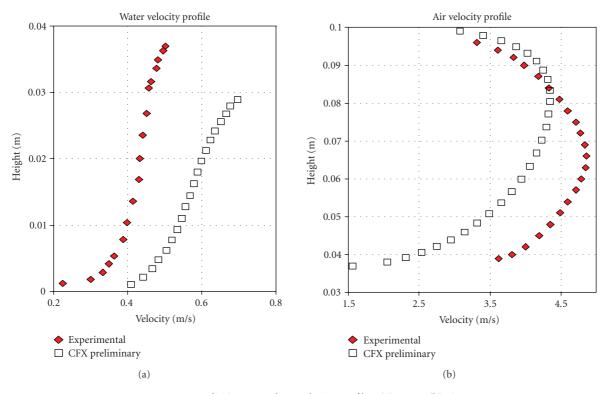
Figure 2: Preliminary results—velocity profiles: (a) water; (b) air.

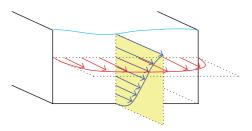Figure 3: Three-dimensional water domain.

Table 1: Details of grids for single-phase analysis.

Code	Domain	2D	3D
FLUENT 6.1	Air	320×35 and 640×70	$320 \times 35 \times 40$
	Water	320×27 and 320×54	$320 \times 27 \times 40$
CFX 10.0	Air	520×34	$520 \times 34 \times 38$
	Water	520×23	$520 \times 23 \times 44$

6.1 [10] and CFX 10.0 [9] codes. These characteristics have been established following the main findings of preliminary mesh sensitivity investigations.

In single-phase calculations, the interface has been modelled as a wall moving at the expected velocity of the free surface. Since this value is not available, it has been imposed in the range 0.50–0.65 m/s, according to the top measured water velocity, 0.502 m/s, which is the available data closer to the interface. The boundary conditions have been imposed according to the preliminary calculation documented in Section 3.1.

Direct numerical simulation (DNS) and large eddy simulation (LES) of stratified flows [11] were used in the framework of the NURESIM Integrated Project to derive some closure laws for interfacial momentum, turbulence, and heat transfer. Future work is still necessary to implement these laws in CFD codes as well as to compare predictions with DNS-LES studies on the same flow conditions [12] and to validate them against experimental data. Anyway, this subject is beyond the aim of the present article.

3.3.1. Single-phase water flow

In Figure 4, the obtained results are shown in terms of longitudinal water velocity profile at the test section located at 9.1 mm from the inlet. The experimental profile is correctly predicted from a qualitative point of view by both CFX and FLUENT codes. No relevant improvements are obtained varying the interface velocity except for the region closer to the moving wall in both two- and three-dimensional calculations. However, two-dimensional calculations underestimate the velocity values by about 10% than three-dimensional ones. Thus, domain three dimensionality has a great relevance on water velocity profile and cannot be neglected in the simulations. Moreover, grid sensitivity analysis has shown that limited improvement is obtained by increasing the number of cells.

Figure 5 shows the comparison between calculated turbulent kinetic energy and experimental data both for two- and three-dimensional simulations. The third dimension
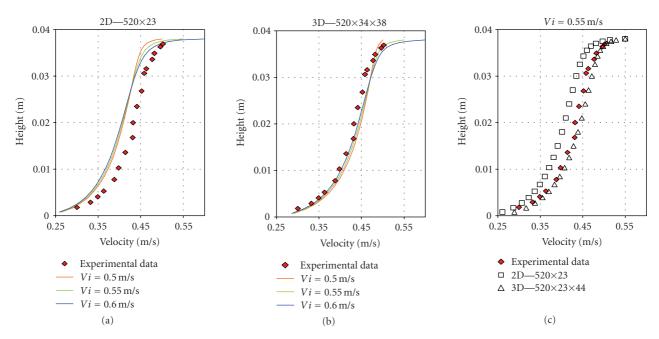
FIGURE 4: Water velocity: (a) 2D grid with different interface velocities; (b) 3D grid with different interface velocities; (c) 3D versus 2D grids.
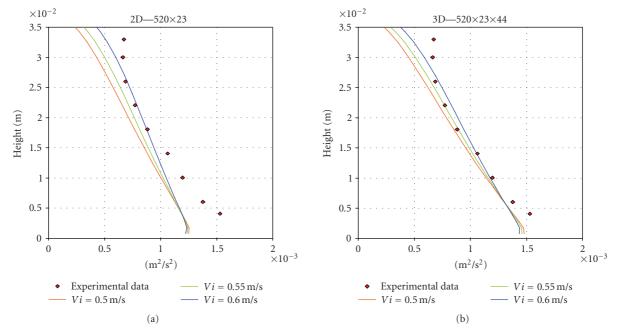
FIGURE 5: Water turbulent kinetic energy: (a) two-dimensional simulations; (b) three-dimensional simulations.

has great relevance on near-wall values, increasing them by about 20%. Calculated values in the region near the interface have a different behavior from experimental data owing to the presence of a solid wall. Turbulence produced by the contact between fluids at the interface is not included in the model. Although these differences in shape and local values, predicted turbulent kinetic energy is in good agreement with measurements, especially for three-dimensional calculations.

3.3.2. Single-phase air flow

Figure 6(a) shows the transversal air velocity profiles at the test section in three-dimensional simulations calculated with CFX, which is predicted with relevant differences on both shape and values. Negligible effects on the results are obtained varying the interface velocity. Two-dimensional calculations show the same behavior as well as results obtained using FLUENT. Moreover, as shown in Figure 6(b),

Figure 6: Air velocity: (a) 3D grid with different interface velocities; (b) 3D versus 2D.
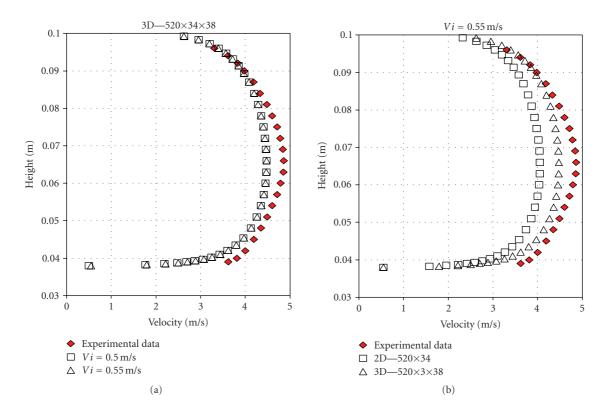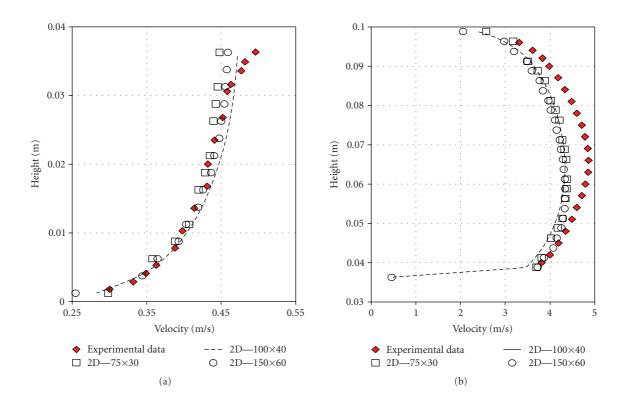

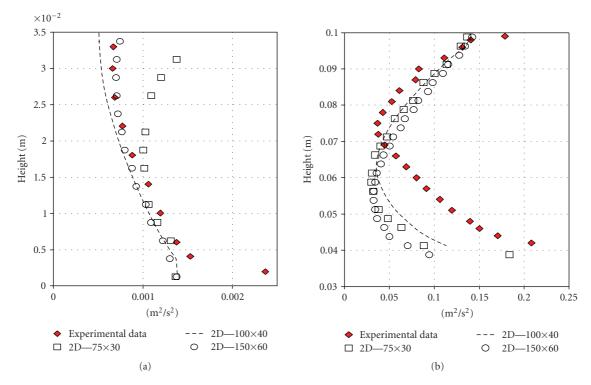Figure 7: Velocity profiles: (a) water; (b) air.

Figure 8: Turbulent kinetic energy: (a) water; (b) air.

the experimental data provide a greater maximum velocity with respect to both two-dimensional (15.8% higher), and three-dimensional simulations (11.4% higher). This is a further confirmation of the three-dimensional flow structure supposed in Section 3.2. However, the systematic underestimation of the velocity needs further investigations.

Finally, from sensitivity analysis performed with FLU-ENT, no relevant advantages are obtained by increasing the cell number or changing the turbulence near-wall treatment.

4. T250 EXPERIMENTAL TEST SIMULATION WITH NEPTUNE_CFD

In the hypothesis of planar symmetry, the computational domain is constituted by a 2D section of the channel; it has been modelled with three successively refined 2D grids built up with the ANSYS ICEM code: 75×30, 100×40 and 150×60 cells, respectively. All imposed boundary conditions were as for CFX calculations (Section 3.1); initially a stratified air/water flow was established and parabolic velocity profiles were imposed for both water and air flows at inlet. Calculations were run with NEPTUNE_CFD V1.0.6 by means of an input deck kindly provided by Mr. Pierre COSTE (CEA/Grenoble). The k-ε model was considered for both air and water turbulence together with interface turbulence production, "Pierre Coste Large Interface Model" [13] was selected for the drag coefficient.

As Figure 7 shows, water velocity profile is quite well predicted in all three cases (maximum error $\sim$7%), while

air velocity profile is appreciably underestimated, especially in the bulk region between wall and free surface (maximum error $\sim$12% for the coarser grid and $\sim$10% for the finer one). It seems that mesh refinement does not produce important improvements, except for the air velocity profile in the region near the interface.

Figures 8(a) and 8(b) show the turbulent kinetic energy profile at probe location for water and air flow, respectively. As in the previous case, the profile is qualitatively well predicted for the water flow, while for the air flow, it is significantly underestimated in the bottom region and overestimated in the upper one. It can be observed that calculated values with refined grids better match experimental data in the upper region of the water stream, with some underestimation near the wall (maximum error $\sim$45%). It is worth noting that the code is able to catch the increase of water turbulence near the free surface due to the air stream, but not due to the presence of solid walls. On the contrary, air turbulent kinetic energy profile does not get significantly better with mesh refinement; results are underestimated near the interface (maximum error $\sim$66%) and slightly overestimated elsewhere.

Calculations were also run considering the "separated phases model" for the interphase drag coefficient. The resulting velocity profiles seem to be very similar to that predicted by ANSYS CFX and shown in Figure 2. In both cases, the interface level is underestimated and the maximum air velocity is reached in the region near the upper wall instead of the air stream core. This could be due to an

incorrect modelling of the drag coefficient. Taking into account results presented in Section 3.3, a 3D simulation was also set up considering a $100 \times 40 \times 20$ grid and the "Pierre Coste Large Interface Model" for the drag coefficient. Unfortunately, only 29 seconds were calculated after one-week run on two processors, but preliminary results were encouraging.

5. CONCLUSIONS

A Computational fluid dynamic analysis of a stratified air-water flow experimental investigation performed at the Institut de Mécanique des Fluides de Toulouse in 1985 [7] was performed. The aim was the comprehension of the experimental data and of the role played by some fundamental parameters. The simulation has been performed by means of three different CFD codes: NEPTUNE_CFD V1.0.6, FLUENT 6.1, and CFX 10.0. The spatial discretizations have been modelled with GAMBIT 1.0 and ANSYS ICEM 10.0 softwares.

Preliminary results of two-phase CFD calculations with a two-dimensional domain suggested that three-dimensional effects are not negligible, so that 2D simulations are not suitable to correctly predict this stratified fluid flow. To better understand the physics of the problem, single-phase analyses were conduced with FLUENT and ANSYS CFX comparing 2D and 3D simulations for both air and water single-phase domain. As a result, relevant improvements of both water and air velocity profile were achieved with 3D simulations. It is worth noting that in such single-phase analyses , the water level was not calculated but fixed according to experimental data.

Two-phase simulations by means of NEPTUNE_CFD code, despite taking into consideration a 2D domain, showed better agreement with measured data when considering the new "Pierre Coste Large Interface Model" for the drag coefficient: water level was correctly predicted and error in velocity profiles decreased, even if some underestimation of the air velocity is still present. Moreover, CFX and NEPTUNE_CFD standard models gave similar results, putting in evidence the fundamental role played by the drag coefficient modelling. Nevertheless, a systematic underestimation of the air medium velocity suggests that further information on the experiment and boundary conditions is needed.

REFERENCES

[1] C. Chauliac, J. M. Aragonés, D. Bestion, D. G. Cacuci, P. Coddington, and L. Dada, "NURESIM: a European platform for nuclear reactor simulation," in *Proceedings of the 14th International Conference on Nuclear Engineering (ICONE-14)*, Miami, Fla, USA, July 2006.

[2] A. Guelfi, D. Bestion, M. Boucker, et al., "NEPTUNE: a new software platform for advanced nuclear thermal hydraulics," *Nuclear Science and Engineering*, vol. 156, no. 3, pp. 281–324, 2007.

[3] J. Laviéville, E. Quémérais, S. Mimouni, and N. Méchitoua, NEPTUNE CFD V1.0 theory manual, EDF, 2006.

[4] J. Laviéville, E. Quémérais, M. Boucker, and L. Maas, NEPTUNE CFD V1.0 User Guide, EDF, 2005.

[5] D. Lucas, Ed., "NURESIM-TH Deliverable D2.1.1: identification of relevant PTS-scenarios, state of the art of modelling and needs for model improvements," European Commission 6th Euratom framework programme 2005–2008, integrated project (IP): NURESIM, nuclear reactor simulations, subproject 2: thermal hydraulics, 2005.

[6] D. Lucas, Ed., "NURESIM-TH Deliverable D2.1.2: review of the existing data basis for the validation of models for PTS," European Commission 6th Euratom framework programme 2005–2008, integrated project (IP): NURESIM, nuclear reactor simulations, sub-project 2: thermal hydraulics, 2005.

[7] J. Fabre, L. Masbernat, and C. Suzanne, "Stratified flow—part I: local structure," *Multiphase Science and Technology*, vol. 3, no. 1–4, pp. 285–301, 1987.

[8] C. Suzanne, *Structure de l'écoulement stratifié de gaz et de liquide en canal rectangulaire*, M.S. thesis, INP, Toulouse, France, 1985.

[9] ANSYS Europe Ltd., "Theory and Modelling Book," ANSYS CFX 10:0 Documentation, 2005.

[10] Fluent Inc., User's Guide, FLUENT 6:1 Documentation, Vol. 10, 2003.

[11] D. Lakehal, "Deliverable D2.1.7.1: turbulence structure at interfacial two-phase flow," European Commission 6th Euratom framework programme 2005–2008, integrated project (IP): NURESIM, nuclear reactor simulations, 2006.

[12] M. Fulgosi, D. Lakehal, S. Banerjee, and V. De Angelis, "Direct numerical simulation of turbulence in a sheared air-water flow with a deformable interface," *Journal of Fluid Mechanics*, no. 482, pp. 319–345, 2003.

[13] P. Coste, "Deliverable D2.1.1.2b: modelling and validation of Nuresim-CFD code about turbulence and friction in an adiabatic stratified flow," European Commission 6th Euratom framework programme 2005–2008, integrated project (IP): NURESIM, nuclear reactor simulations, sub-project 2: thermal hydraulics, 2007.

Research Article

Decay Heat Removal and Transient Analysis in Accidental Conditions in the EFIT Reactor

Giacomino Bandini,[1] Paride Meloni,[1] Massimiliano Polidori,[1] Maddalena Casamirra,[2] Francesco Castiglia,[2] and Mariarosa Giardina[2]

[1] *Dipartimento Fusione, Tecnologie e Presidio Nucleari, ENEA Centro Ricerche "Ezio Clementel," Via Martiri di Monte Sole, 4, 40129 Bologna, Italy*
[2] *Dipartimento di Ingegneria Nucleare, Università degli Studi di Palermo, Viale delle Scienze-Parco d'Orleans, 90128 Palermo, Italy*

Correspondence should be addressed to Giacomino Bandini, giacomino.bandini@bologna.enea.it

The development of a conceptual design of an industrial-scale transmutation facility (EFIT) of several 100 MW thermal power based on accelerator-driven system (ADS) is addressed in the frame of the European EUROTRANS Integral Project. In normal operation, the core power of EFIT reactor is removed through steam generators by four secondary loops fed by water. A safety-related decay heat removal (DHR) system provided with four independent inherently safe loops is installed in the primary vessel to remove the decay heat by natural convection circulation under accidental conditions which are caused by a loss-of-heat sink (LOHS). In order to confirm the adequacy of the adopted solution for decay heat removal in accidental conditions, some multi-D analyses have been carried out with the SIMMER-III code. The results of the SIMMER-III code have been then used to support the RELAP5 1D representation of the natural circulation flow paths in the reactor vessel. Finally, the thermal-hydraulic RELAP5 code has been employed for the analysis of LOHS accidental scenarios.

1. INTRODUCTION

Within the EURATOM Sixth Framework Program (FP6), the EUROTRANS integrated project [1] is expected to provide a significant contribution to the demonstration of the industrial transmutation through the accelerator-driven system route. The goal will be reached through two phases: the realization of a detailed design for an experimental facility of 50 to 100 MWth power which shows the technical feasibility of transmutation in an ADS (XT-ADS), and at the same time, the development of a conceptual design of a generic European Transmutation Demonstrator (ETD) of several hundreds of MWth, to be realized in the long term (EFIT).

The EFIT reactor should be able to produce energy at reasonable costs with enhanced transmutation performances, maintaining as much as possible the high safety level. Modifications introduced in the plant layout with respect to smaller facilities contribute for a more compact primary system and a higher core power density: the elimination of

intermediate loops by installation of steam generators inside the primary vessel and the implementation of mechanical pumps for forced circulation.

In order to assure a high safety level, a DHR system provided with four independent inherently safe loops is installed in the primary vessel to remove the decay heat by natural convection circulation under accidental conditions which are caused by a loss of heat removal by the secondary side through the steam generators.

In the present study, performed in the frame of a collaboration between ENEA and the University of Palermo, the multi-D SIMMER-III code has been applied to confirm the adequacy of the DHR system design and for the calibration of the 1D RELAP5 model to be used for T/H transient analysis of EFIT.

2. THE EFIT REACTOR

The EFIT reactor [2] is a pool-type reactor which uses pure melted lead as primary coolant in forced circulation by
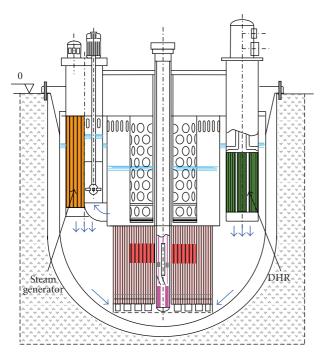
FIGURE 1: Scheme of the EFIT reactor block.

FIGURE 2: Functional scheme of one DHR loop.

means of 4 mechanical pumps placed in the hot collector zone. The reactor thermal power, which is approximately 400 MW, is removed in normal operation by 8 helical-coil tube bundle steam generators, which are located in the upper part of the primary vessel to enhance natural circulation in case of loss of primary pumps. The scheme of the EFIT reactor block is depicted in Figure 1.

The main thermal-hydraulic parameters of the EFIT reactor are given in Table 1. The core power is removed by 32.3 tons of lead working between 673 K and 753 K. The primary coolant at the core outlet is sucked by pumps straight inside the steam generators, then comes out and flows towards the vessel bottom for coming back and cooling the core. So the vessel will be in contact with the coolant at its minimum temperature (673 K), avoiding mechanical stresses due to high lead temperature at core outlet.

In the upper annular space between the inner cylindrical vessel and the main reactor vessel, the heat exchangers of the DHR system are placed for core decay heat removal under accidental conditions.

2.1. The decay heat removal system

The DHR system is conceived for inherently safe decay heat removal in accidental conditions by means of natural circulation and with passive mode actuation. The system consists of 4 independent loops filled with organic diathermic fluid (oil) that dissipate the decay heat to the atmosphere by natural convection circulation. The functional scheme of one DHR loop is depicted in Figure 2. Each loop consists of a dip cooler (decay heat eXchanger, (DHX)) immersed in the lead, where the oil partially vaporizes (oil boiling point determined by superimposed pressure of inert gas), and an air-vapour

TABLE 1: Main EFIT thermal-hydraulic parameters.

Reactor power (MW)	384
Core lead mass flow rate (kg/s)	32300
Core lead temperature (inlet/outlet, K)	673/753
Primary circuit total pressure drop (MPa)	About 0.08
Core pressure drop (MPa)	About 0.04
Secondary steam pressure (MPa)	14
Secondary steam temperature (K)	723
Feedwater temperature (K)	608
DHR system power (4 units, MW)	26.6

condenser with stack chimney and interconnecting piping. The lead enters radially the DHX through a window in the cylindrical shell and leaves axially the DHX through the open bottom end of the shell.

At normal operating conditions, the oil is below its boiling point and the DHR system removes the heat losses from steam generators and inner vessel (a few 100 kW) to keep cold the upper part of the reactor vessel. In accidental conditions (e.g., LOHS), when the lead temperature increases in the annular space where the DHXs are located, the oil starts to boil enhancing heat transfer in the DHR and thus favouring natural circulation on both primary and secondary sides. Each DHX is rated at approximately 6.7 MW in decay heat removal conditions.

3. SIMULATION OF DHR OPERATION WITH THE SIMMER-III CODE

The SIMMER-III code [3], jointly developed by JNC (J), FZK (D), and CEA (F), is an advanced safety analysis computer code originally developed to investigate postulated core disruptive accidents in liquid-metal fast reactors. SIMMER-III is a two-dimensional, three-velocity field, multiphase, multicomponent, Eulerian, fluid-dynamics code coupled with a space-dependent neutron kinetics model. By integrating all the original physical models, SIMMER-III is now applicable to a large variety of reactor calculations and other complex multiphase flow problems. The code is provided with a turbulent diffusion model to evaluate the effects of recirculating flows. This model, which is simpler than classical turbulent models of CFD codes, has been applied in the present analysis.

The EFIT reactor has been modelled in 2D cylindrical geometry with SIMMER-III (see Figure 3). The core is represented by 6 radial fuel rod rings plus the reflector and bypass zones, and discretized in 14 axial nodes. The primary pump section, the steam generators, and the DHR heat exchangers are represented by annular zones with equivalent cross flow area. The simulation of DHR loops is limited to the in-vessel heat exchangers, and the power removal is calculated as a function of the temperature difference between the primary flowing lead and the boiling oil in the secondary side. As a conservative assumption in the accident analysis, the DHR system is considered in degraded conditions with 3 out of 4 loops in service.

A protected LOHS scenario has been simulated with the SIMMER-III code in order to evaluate the capability of the DHR system for decay heat removal in transient conditions by natural circulation in the primary system. Stagnant lead is assumed inside the primary vessel at transient initiation with simultaneous loss of primary pumps and steam generator heat removal function. Initial lead and core temperatures (clad and fuel) are set according to RELAP5 steady-state results for reactor operation at 384 MW nominal power.

The distribution of lead temperature in the primary vessel calculated by SIMMER-III is represented in Figure 4 from the beginning up to 1 hour transient. Initially, the release of heat from hot fuel rods leads to lead heatup and strong recirculation in the upper plenum. Due to the different density and gravity effect, hot lead flowing down at the steam generator outlet moves upward in the annular external region between the inner cylindrical vessel and the reactor vessel where the DHR heat exchangers are located. A natural circulation then starts inside the DHX where the lead is cooled by efficient heat transfer to the boiling oil of the secondary circuit. A mixing region of cold and hot fluids is evidenced below the DHX and the steam generator resulting in temperature increase of the cold lead flowing down at the DHX outlet towards the core inlet. Enhanced temperature stratification is evidenced after 1 hour transient when quasi steady-state conditions are reached, and the core decay power is efficiently removed by natural circulation through the core and the DHR system with limited lead temperature increase.
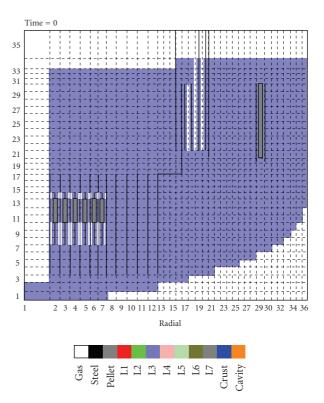
FIGURE 3: SIMMER-III nodalization scheme of the EFIT reactor.

At present, the SIMMER-III code is not validated for this kind of analysis. The results of lead-bismuth natural circulation experiments, which are foreseen in the integral CIRCE facility at ENEA/Brasimone research centre, could be used to confirm the capabilities of the code in this area and propose possible and beneficial code model improvements.

4. CALIBRATION OF THE RELAP5 MODEL ON SIMMER-III RESULTS

The RELAP5 code [4], developed by INEEL for the US-NRC, is a lumped parameter code used for best-estimate thermal-hydraulic (T/H) transient analysis in light water reactors. The RELAP5 code has been modified by ANSALDO (including lead properties) to be used for lead-cooled ADS analysis. Lead thermophysical property data and heat transfer correlations for heavy liquid metal in different geometries have been taken from the literature and available studies and introduced in the modified code [5]. Conservative assumptions have been considered for heat transfer in core bundle geometry, and new correlations have been developed for helical tube geometry of SGs [6]. The so modified RELAP5 code has been applied in previous ADS plant transient analysis such as PDS-XADS [7], and the results have been successfully compared with other codes. Furthermore, the code has been validated against experimental data from tests conducted on the CHEOPE and CIRCE facilities at ENEA/Brasimone Centre [8, 9]; a new experimental program to be conducted on the large-scale integral facility CIRCE will provide further valuable data for code validation and
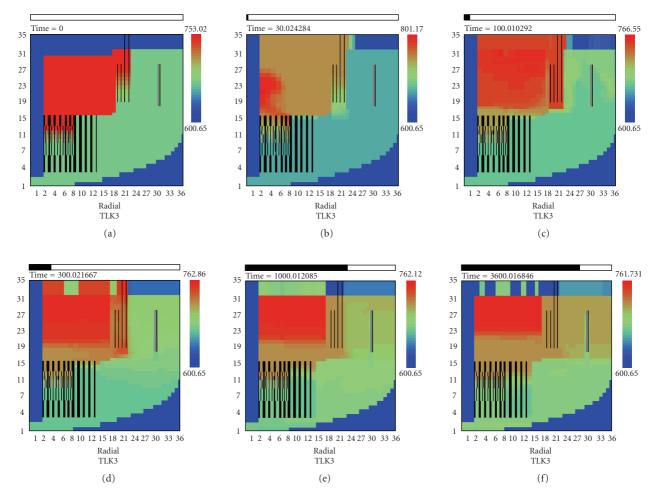
Figure 4: Time evolution of lead temperature (K) distribution in the primary vessel.

verification. This modified version of RELAP5 code is used in the framework of a collaboration between ENEA Centre and the Department of Nuclear Engineering (DIN) of the University of Palermo for T/H transient analysis of EFIT.

The RELAP5 nodalization scheme of the EFIT reactor employed for T/H transient analysis is shown in **Figure 5**. In the model, the lead mass inventory distribution and the major flow paths are represented. The core is discretized in three zones, each one represented with average and hot channel with equivalent flow area coupled with corresponding pin thermal structures. The reflector and bypass zone is represented by an equivalent hydraulic channel, while the target unit is not simulated. Primary pumps are modelled according to preliminary EFIT pump design. Steam generator primary (shell) and secondary side (straight and helical tubes) are modelled in details, while just boundary conditions are used for the secondary loop. The DHR system model is limited to the DHX primary side imposing the exchanged power as a function of the lead temperature at the DHX inlet.

In case of loss of primary pumps and LOHS scenario with operation of the DHR system, the natural circulation flow paths in the 1D RELAP5 representation of EFIT are arbitrarily defined in the input nodalization scheme. Therefore, mixing effects at steam generator and DHX outlets and inside plenum recirculation phenomena, observed with more detailed SIMMER-III analysis, are not taken into account. These phenomena may tend to reduce the lead mass flow rate in natural circulation through the core and the DHR system in accidental conditions, as demonstrated by comparing SIMMER-III and RELAP5 results under the same transient conditions. As expected, RELAP5 predicts larger lead mass flow rate than SIMMER-III through the core and the DHR system.

The RELAP5 model has been calibrated in order to reproduce as close as possible the SIMMER-III results. According to nomenclature in **Figure 5** (green characters), fluid mixing in the volume below steam generator and DHX is defined by the fraction of lead mass flow rate ($x = 17\%$) entering this volume from the DHX outlet. This fraction is deduced from SIMMER-III results by mass and energy balances for the volume according to

$$y = \frac{m_C(T_{Ci} - T_{Do})}{(T_{Di} - T_{Do})}, \qquad x = y + m_D - m_C, \qquad (1)$$
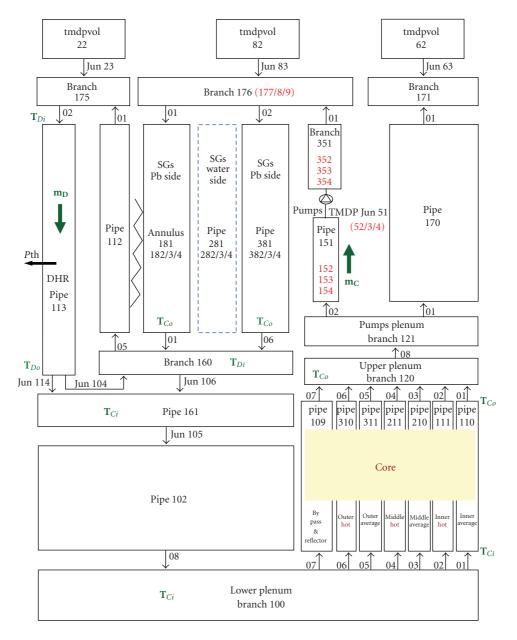
FIGURE 5: RELAP5 nodalization scheme of EFIT reactor.

where C and D denote, respectively, core and DHX parameters (inlet/outlet temperatures and mass flow rate of lead).

Additional pressure drop coefficients have been implemented in the revised RELAP5 model of the primary system (at pump and DHX outlet locations) to reproduce the natural circulation mass flow rates calculated by the SIMMER-III code in the medium term.

The lead mass flow rate and decay heat removal in the DHR system calculated by the two codes are presented in Figure 6. Both codes predict efficient removal of decay power after about 2000 seconds. Mass flow rates through the core and the DHR heat exchangers are equivalent in the medium term. Code results differ in the initial transient owing to the different modelling.

5. LOHS ACCIDENT ANALYSIS WITH RELAP5

The LOHS accidental transient has been analysed with the revised RELAP5 model. The initiating event is the total loss of feedwater of secondary loops. The following lead temperature increase in the primary circuit is supposed to lead to reactor trip on high core outlet temperature signal by the protection system. Reactor trip, consisting in the proton beam switch-off, is assumed with 1 second delay after the average core outlet temperature exceeds 773 K (20 K above the nominal outlet temperature). As a conservative assumption, primary pumps trip is assumed to occur at the same time as the reactor trip and no pump inertia is considered (pump design is not precisely defined yet), in

(a)

(b)
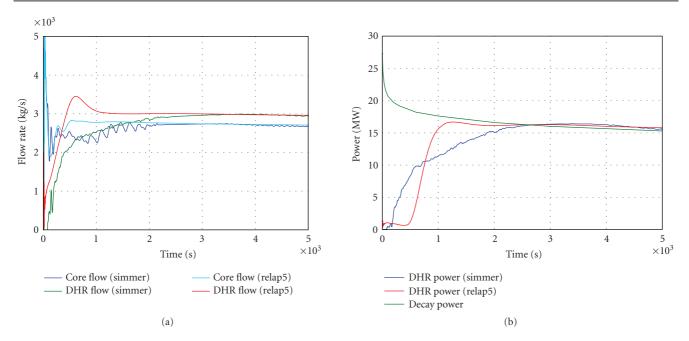
Figure 6: Lead mass flow rates (core and DHR) and heat removal in the DHR system (3 units).

(a)

(b)
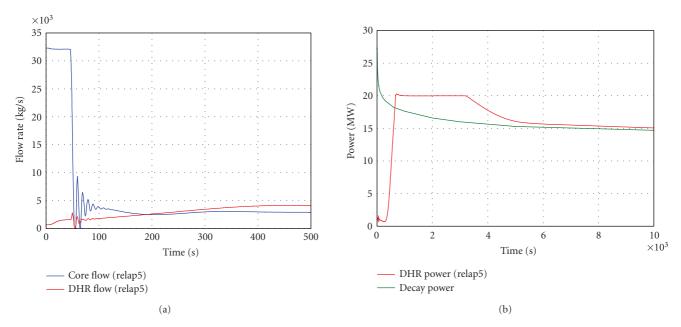
Figure 7: Lead mass flow rates (core and DHR) and heat removal in the DHR system (3 units).

order to maximize core peak temperature just after reactor trip.

The results of the analysis are presented in Figures 7 and 8. Reactor trip is calculated by RELAP5 at 46 seconds. After some initial oscillations induced by free level movements (see Figure 7), the lead mass flow rates through the core and the DHR system become stable and the DHR attains maximum performance (20 MW for the 3 units supposed to be in operation) after about 700 seconds.

The peak clad temperature reaches 862 K in the hottest channel of outer core zone as shown in Figure 8 (the clad safety limit in normal operation of 823 K is exceeded for few seconds only), then all temperatures stabilize starting from 5000 seconds at acceptable values. The reactor vessel wall temperature reaches a maximum value of 724 K around 2200 s during the transient, then it stabilizes at 713 K in the medium term, below the maximum acceptable value of 723 K. This vessel temperature limit has been defined to assure the vessel integrity for the entire life of the plant. The vessel wall temperature peak of 724 K is not a critical issue, because its duration is limited in time. Furthermore, an improved DHX solution now implemented in the EFIT

(a)

(b)
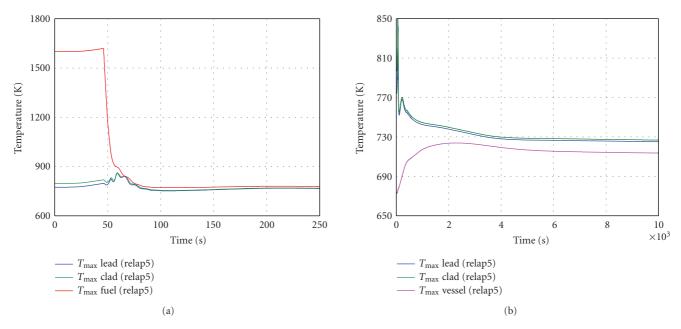
FIGURE 8: Maximum core (lead, clad, and fuel) and vessel wall temperatures.

design, with increased length of the external wall and reduced pressure drops, which facilitate the natural circulation of lead through the DHX, foresees an increase of about 15% of the lead mass flow rate, thus reducing significantly the thermal load on the vessel wall.

The flow path imposed in the RELAP5 model accelerates the startup of natural circulation through the DHX with respect to the SIMMER-III simulation (see comparison of mass flow rates calculated by the two codes in Figure 6); however, the integral power removed by the DHR system at 2200 seconds calculated by SIMMER-III is consistent with the RELAP5 value, therefore, no appreciable increase of the peak vessel wall temperature is exhibited at that time by SIMMER-III with respect to RELAP5 analysis.

6. CONCLUSIONS

The performances of the DHR system provided in the EFIT reactor have been confirmed by SIMMER-III and RELAP5 analyses of accidental conditions with complete loss of heat removal by the secondary system. In particular, natural circulation in the primary circuit through the core and the DHR system stabilises in less than one hour, and three out of four DHR units are sufficient to adequately remove the core decay power under LOHS transient conditions.

The 1D RELAP5 model of EFIT has been successfully calibrated on the basis of the SIMMER-III results by evaluating the amplitude of hot and cold lead mixing at steam generator and DHX outlets and the effects of turbulence phenomena and recirculating flows in the upper and lower plena of the reactor vessel. Except for the initial transient, the results obtained with the revised RELAP5 model are close to the SIMMER-III results. However, code validation for this kind of applications is still in progress, and limited for SIMMER-III code. Therefore, the results of the DHR system

performance analysis will be precised after further validation of the codes at the CIRCE facility or other appropriate facilities.

Finally, the application of RELAP5 to the LOHS accident analysis has shown that the DHR system is able to face up accidental situations with sudden total loss of heat removal by the secondary side with limited increase in core temperature and brings the plant in safe conditions in the medium term. Also the vessel wall temperature increase is limited below acceptable value in the medium term with adequate margin, taking into account more recent DHX design improvements not addressed in this study.

REFERENCES

[1] J. U. Knebel, H. A. Abderrahim, L. Cinotti, et al., "European research programme for the transmutation of high level nuclear waste in an accelerator driven system (EUROTRANS)," in *Proceedings of the 9th International Exchange Meeting on Partitioning & Transmutation*, pp. 1–21, Nîmes, France, September 2006.

[2] L. Cinotti, "Engineering solutions and thermal-hydraulic issues for a promising safe ADS system," in *Proceedings of the 6th International Conference on Nuclear Thermal Hydraulics, Operations and Safety (NUTHOS '04)*, pp. 1–18, October 2004, Nara, Japan.

[3] H. Yamano, S. Fujita, Y. Tobita, et al., "SIMMER-III: a computer program for LMFR core disruptive accident analysis," Tech.

Rep. JNC TN9400 2003-071, Japan Nuclear Cycle Development Institute, Ibaraki, Japan, August 2003.

[4] S. M. Sloan, R. R. Schultz, and G. E. Wilson, "RELAP5/MOD3 code manual," Tech. Rep. NUREG/CR-5535, INEL-95/0174, Nuclear Regulatory Commission, Washington, DC, USA, June 1995.

[5] F. Bianchi, S. Bocci, G. Forasassi, et al., "Implementation and preliminary verification of the RELAP5/PARCS code for Pb-Bi cooled subcritical system," in *Proceedings of the International Conference on Accelerator Applications (AccApp '01)*, Reno, Nev, USA, November 2001.

[6] M. Casamirra, F. Castiglia, M. Giardina, and P. Meloni, "RELAP5 modification for CHEOPE simulations," in *Proceedings of the International Conference on Nuclear Energy for New Europe*, Bled, Slovenia, September 2005.

[7] F. Bianchi, P. Meloni, and F. Mattioda, "Accident analysis of an experimental accelerator driven system," in *Proceedings of the 13th International Conference on Nuclear Engineering (ICONE-13)*, Bejing, China, May 2005.

[8] W. Ambrosini, N. Forgione, F. Oriolo, et al., "Natural circulation of lead-bismuth in a one-dimensional loop: experiments and code predictions," in *Proceedings of the 10th International Conference on Nuclear Engineering (ICONE-10)*, vol. 2, pp. 755–761, Arlington, Va, USA, April 2002.

[9] P. Meloni, A. D. Wagner, F. Castiglia, M. Casamirra, P. Agostini, and G. Bertacci, "Investigation of RELAP capability to simulate the LBE cooling system thermal-hydraulic," in *Proceedings of the 8th Information Exchange Meeting on Actinide and Fission Product Partitioning & Transmutation*, pp. 637–647, Las Vegas, Nev, USA, November 2004.

Research Article

RELAP5/MOD3.3 Code Validation with Plant Abnormal Event

Andrej Prošek and Borut Mavko

Reactor Engineering Division, Jožef Stefan Institute, Jamova cesta 39, 1000 Ljubljana, Slovenia

Correspondence should be addressed to Andrej Prošek, andrej.prosek@ijs.si

Measured plant data from various abnormal events are of great importance for code validation. The purpose of the study was to validate the RELAP5/MOD3.3 Patch 03 computer code with the abnormal event which occurred at Krško Nuclear Power Plant (NPP) on April 10, 2005. The event analyzed was a malfunction, which occurred during a power reduction sequence when regular periodic testing of the turbine valves was performed. Unexpected turbine valve closing caused safety injection signal, followed by reactor trip. The RELAP5 input model delivered by Krško NPP was used. In short term, the calculation agrees very well with the plant measured data. In the long term, this is also true when operator actions and special plant systems are modeled. In the opposite, the transient would progress quite differently. Finally, the calculated data may be supplemental to plant measured data when the information is missing or the measurement is questionable.

1. INTRODUCTION

Usually the validation has been performed using experimental data from scaled-down test facilities. Several code assessments of best estimate codes using experimental data were reported in the literature [1, 2]. An overview on the use of experimental data in nuclear reactor thermal hydraulics is given in [3]. Validation activities for thermal-hydraulic system codes and scaling issues are concisely described in [4]. It is stated that for validation purposes are important especially validation matrices of separate effects test and integral test facilities. It is also noted that the data from NPP can be used, if available, and that the data obtained are the ones recorded by the system of control of the plant. Typically, real plant data are limited mostly to operational events such as malfunction of valves, pumps, or other components, resulting in complex plant response [5–8]. However, real plant data are full scale and have true geometry; therefore they are of great importance for code validation and for better understanding of the unit response to deviations from normal operation.

In this paper an abnormal event, which occurred at Krško Nuclear Power Plant (NPP) on April 10, 2005, has been studied with the RELAP5/MOD3.3 Patch 03 computer code [9]. For the analysis the RELAP5 input model delivered by Krško NPP was used. This is a full two-loop plant model including major components of the primary and secondary system. The limitations of the delivered model for this transient were that the secondary side was modeled up to the turbine only and that no auxiliary systems consuming steam after transient were included. Namely, the steam flow is very important for the behavior of the secondary pressure and consequently the primary pressure. Both pressures dictate the operation of the control and safety systems. The analysis was performed for uprated power conditions (2000 MWt) with new steam generators and cycle 21 settings, corresponding to the plant state after outage and refuelling in September 2004.

A malfunction occurred during a power reduction sequence when regular periodic testing of the turbine valves was performed. This caused plant trip, while all the safety systems responded according to the design specification, so the event caused no hazard to the environment or plant staff and did not challenge the plant safety. The scope of the analysis was to analyze the transient and compare the results with calculations.

The analysis was divided into five phases. The first four phases were performed to obtain steady-state conditions. In the first phase steady state at 100% power level was demonstrated. In the second phase the power was reduced from 100% to 91.72% level. In the third phase one cycle of turbine governor valve closing and opening was simulated
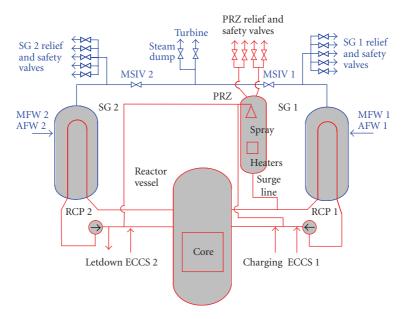
FIGURE 1: Krško NPP simplified scheme.

in order to obtain as close as possible initial conditions. In the fourth phase the steady state at 91.72% was verified by comparing calculated initial conditions with plant data, which were available for 53 seconds before the transient start. Finally, in the last phase the transient was analyzed for 1825 seconds as the measurement was stopped at that time.

2. INPUT MODEL, EVENT, AND ANALYSIS SCENARIO DESCRIPTION

For the abnormal event analysis the RELAP5/MOD3.3 Patch 03 computer code released in April 2006 was used. The basic RELAP5/MOD3.3 thermal-hydraulic model uses six equations: two mass conservation equations, two momentum conservation equations, and two energy conservation equations. The system of basic equations is enclosed with empirical correlations. For more details the reader is referred to [9].

2.1. RELAP5 input model description

To perform the analysis, Krško NPP has provided the qualified base RELAP5 input model, so-called "master input deck," which has been used for several analyses, including reference calculations for Krško full scope simulator verification [10–12]. The simplified scheme of the Krško NPP nodalization is presented in Figure 1. A full two-loop plant model, delivered by Krško NPP, has been used for the analysis. It includes the new Siemens-Framatome replacement steam generators type SG 72 W/D4-2. The analysis was performed for uprated power conditions (2000 MWt) with new steam generators (SGs) and cycle 21 settings, corresponding to the plant state after outage and refuelling in September 2004.

The model consists of 469 control volumes, 497 junctions, and 378 heat structures with 2107 radial mesh points. Modelled are important components as the reactor vessel, pressurizer surge line, pressurizer (PRZ) vessel, pressurizer

spray lines and spray valves, pressurizer power operated relief valves (PORV), and safety valves. Primary piping includes hot leg, primary side of steam generator by inlet and outlet plenum, among which a single pipe is representing the U-tube bundle, intermediate leg and cold leg with reactor coolant pump (RCP). Loops are symmetrical except for the pressurizer surge line and chemical and volume control system connections layout (charging and letdown). Modeled is emergency cooling system (ECCS) with high-pressure injection system (HPIS), accumulators, and low-pressure injection system (LPIS).

The parts of the steam generator secondary side are represented by riser, separator and separator pool, downcomer, and steam dome. Main steamlines have main steam isolation valves (MSIVs), SG relief, and safety valves. Turbine valve and steam dump flow are regulated by corresponding logic. Main feedwater (MFW) piping is modelled till the MFW pump, which is modelled as time-dependent junction. Auxiliary feedwater (AFW) is injecting above the SG riser.

Besides, a considerable number of control variables and general tables are part of the model. They represent protection, monitoring, and simplified control systems used only during steady-state initialization, as well as main plant control systems: rod control system, pressurizer pressure control system, pressurizer level control system, steam generator level control system, and steam dump.

The plant protection systems defined using trip logic include reactor trip, safety injection (SI) signal, turbine trip, steamline isolation, main feedwater isolation, and auxiliary feedwater start.

2.2. Event description

The Krško NPP technical specifications required that the turbine overspeed protection system will be demonstrated

Table 1: Subdivision of analysis.

Part of analysis	Phase of analysis	Description of phase with the time of analysis duration
Part 1	Phase 1	Steady state at 100% power (1000 seconds)
	Phase 2	Power reduction from 100% to 91.72% for valve testing (1000 seconds)
	Phase 3	Cycling of one turbine governor valve (1500 seconds)
	Phase 4	Steady state at 91.72% power (500 seconds)
Part 2	Phase 5	Turbine governor valve closure with reactor trip (1900 seconds)*

*measured data available for 1825 seconds.

operable at least once per 31 days by cycling each of the high pressure turbine governor and stop valves trough at least one complete cycle from the running position. The test procedure consists of two steps. In the first step the turbine (and by this reactor power) must be reduced below 92% to fulfil the test conditions. In the second step the test of turbine governor and stop valves is performed.

In the first step the turbine power is reduced until governor valve number 4 is closed. Then the turbine power is reduced for another 7% until the nuclear power is less than or equal to 92%. Then the closure of governor valves is changed from sequential to single mode of operation. The position of governor valves is checked to be less than or equal 35% of opening. On the opposite, the power should be additionally reduced before the test start.

In the second step of testing turbine valves, the allowed maximum position of governor valves is defined to be 55% of opening. To fulfil this, "valve position limit display" button is pushed to read "flow demand" and "valve position limit." Then the valve position limit is raised to 160% and valves are tested one by one. The valve is first closed and then opened to its initial value. When all valves are tested, the valve position limit is decreased to the value at test start (less than or equal 35% of opening). When lowering valve position limit, the value should not be below "flow demand" value. On the opposite, the governor valves start to close. In the case of the above-described event these really happened. The valves were closing for 5 seconds from 35.5% to 12.2% position, then stabilized for 12 seconds, and after that the position starts to increase to 14%, followed by full valve closure. The valve positions indicate that the operator sets the valve position limit below flow demand and after 16 seconds he tried to restore the turbine flow. This resulted in reactor trip in next 2 seconds or less (it should be noted that data were available for each 2 seconds). Setting the valve position limit below the flow demand was the first operator error. When operator noticed decreased electrical power output he tried to correct the setpoint to the desired (higher) value but he was not aware of the steam dump operating. The increased steam flow demand resulted in the high steam flow causing the steam generator pressure drop, therefore the SI signal was generated on low steamline pressure. On SI signal the reactor trip signal was generated followed by turbine trip. SI signal started also both AFW pumps with 25 seconds delay.

The measured data were available for 1878 seconds and were sampled every 2 seconds. The data for the first 52 seconds represent the steady state while at 54 seconds the governing valves were already closing indicating that the transient started. Therefore, it was assumed that governor valves started to close at 53 seconds. This time is transient start time ($t = 0$). The remaining data up to 1878 seconds represent the transient, lasting 1825 seconds.

2.3. Analysis scenario description

The RELAP5/MOD3.3 Patch 03 analysis was divided into two parts. In the first part, the power was reduced and closing and opening of governor valve was simulated. The purpose of simulating this part was to obtain the RELAP5 initial conditions as close as possible to the plant initial conditions before the reactor trip. It consists of four phases as shown in Table 1. In the first phase, steady state at 100% power level was demonstrated. In the second phase, the power was reduced from 100% to 91.72% level and steady state at reduced level was demonstrated. In the third phase, one cycle of turbine governor valve closing and opening was simulated in order to obtain as close as possible initial conditions. In total, there are four turbine governor valves. The stop valves were not simulated as they close when governor control valve is fully closed. When the governor valve starts to open, the stop valves open too. Also for the third phase, the steady state was demonstrated. When at time −500 seconds the time dependent junction component was replaced by valve component this caused some transient in the steam flow. Therefore, steady-state calculation with valve component was performed in the fourth phase at 91.72% power level, giving slightly different plant condition because of replacing time dependent junction. This steady state was compared with the plant data, which were available for 53 seconds before the transient start. By simulating part 1 there was no need to use artificial controls to achieve steady-state condition at 91.72% level. It should be also noted that during real testing of turbine governor valve, the position of other three governor valves is adjusted automatically to keep the reduced power constant. Also, the plant data were not available at 100% power to verify initial conditions before power reduction. The novel feature of the above approach is that the initial conditions were obtained by just maneuvering the plant, that is, opening and closing the turbine governor valve.

In the second part, which is the fifth phase, the transient leading to reactor trip and plant response to turbine and reactor trip was simulated. The time zero was denoted for the transient start. This means that part 1 analysis lasted from −4000 seconds to 0 second, while the transient was analyzed from 0 second till 1900 seconds.
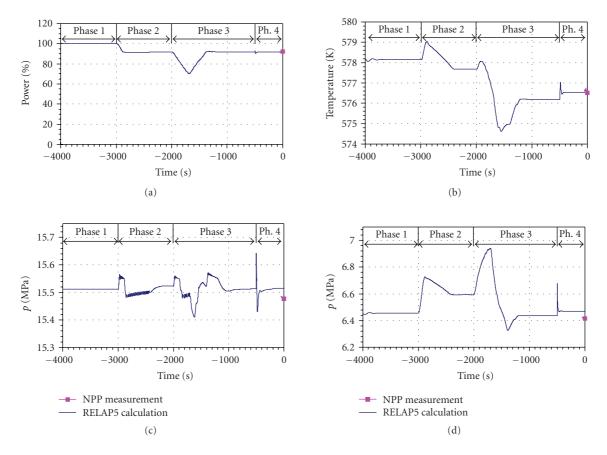
(a)

(b)

NPP measurement
RELAP5 calculation

(c)

NPP measurement
RELAP5 calculation

(d)

FIGURE 2: Achieving steady state at 91.72%: (a) core power, (b) RCS average temperature, (c) PRZ pressure, (d) SG 1 pressure.

3. RESULTS

Figure 2 shows the results for part 1 analysis, while Figures 2 and 3 present short and long term results for part 2 analysis. In part 1 analysis, the power was reduced from nominal value (100%) to test conditions at around 91.72% and opening of turbine governor valve was simulated. In part 2 analysis, the turbine governor valve closure with reactor trip at 91.72% power level, and associated operator actions were simulated.

3.1. Part 1 analysis—achieving steady state at 91.72% level

Figure 2 shows some important calculated variables during simulated governor valve opening and closing and explains how initial condition at 91.72% power level was obtained. The calculated data (labelled "RELAP5 calculation") are shown in the time interval (−4000 seconds–0 second) while the measured steady-state data (labelled "NPP measurement") were available for interval (−53 seconds–0 second) only. The power reduction scheme was such that flow was reduced from nominal value 1086 kg/second to 991 kg/second simulating the turbine valve test initial conditions. Then the simulation of closing and opening of one governor valve was performed without operating other turbine governor valves. This caused rod insertion

and withdrawal. For closing and opening, 5 minutes were assumed for 25% power reduction from 91.72% power level and 5 minutes for power increase. This is less than 5% of nominal power per minute load reduction. In this way, the steam dump operation was prevented. When the VALVE component was introduced back into the input model at −3500 seconds, short oscillation is introduced which quickly stabilizes during the fourth phase.

The obtained initial conditions are shown in Table 2. The first two columns describe the plant variables and their units. The third column shows average value of plant measured initial condition. The data were averaged in the time interval (−53 seconds–0 second) because the measured values were slightly oscillating for some variables. The time 0 second was chosen as start of reactor trip transient. For this time, the plant measured initial conditions are given in the fourth column, which in some cases differ from average steady-state values. In the fourth column is given design accuracy for the measured channels. The design accuracy can be obtained by calibrating the channels. The real accuracy is lower as time drift and environmental effect should be taken into account too. Finally, in the last three columns steady-state values at the end of the second, the third, and the fourth phases are given. In the sixth column are given calculated initial conditions after initial power reduction below 92% (rod insertion at time −2000 seconds), in the seventh initial conditions after rods withdrawal (at time −500 seconds), and in the last
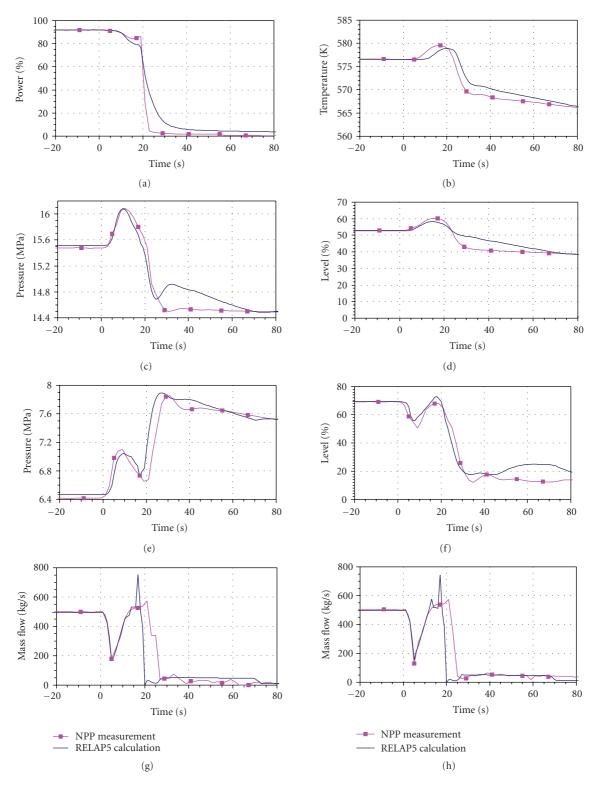
FIGURE 3: Transient with reactor trip—short term: (a) core power, (b) RCS average temperature, (c) PRZ pressure, (d) PRZ level, (e) SG 1 pressure, (f) SG 1 NR level, (g) SG1 steam flow, (h) SG 2 steam flow.

column the initial conditions at the time of transient start ($t = 0$). When comparing the RELAP5 initial conditions with measured initials conditions, with the exception of feedwater flow for loop 2, all values are within design accuracy.

Please note that for power reduction, the turbine flow was modeled by RELAP5 component TMDPJUN, with which linear flow decrease and increase can be prescribed. The benefit of having linear power decrease was to see

TABLE 2: Initial conditions for reactor trip transient.

Variables	Unit	Measured (average)	Measured ($t = 0$ second)	Design accuracy	Calculated ($t = -2000$ seconds)	Calculated ($t = -500$ seconds)	Calculated ($t = 0$ second)
Pressurizer pressure	MPa	15.48	15.48	± 0.37 %	15.52	15.51	15.52
SG 1 pressure	MPa	6.42	6.42	± 0.37 %	6.59	6.43	6.47
SG 2 pressure	MPa	6.40	6.40	± 0.37 %	6.57	6.42	6.45
Feedwater 1 mass flow rate	kg/s	499.0	504.0	± 0.38 %	495.2	495.4	495.5
Feedwater 2 mass flow rate	kg/s	503.6	500.6	± 0.38 %	497.7	498.1	498.1
Main steamline 1 mass flowrate	kg/s	493.9	492.6	± 0.46 %	495.2	495.4	495.4
Main steamline 2 mass flowrate	kg/s	501.6	501.5	± 0.46 %	497.8	498.1	498.1
Pressurizer liquid level	%	53.02	52.95	± 0.37 %	56.10	51.88	52.63
Steam generator 1 NR level	%	69.25	69.15	± 0.37 %	69.34	69.26	69.28
Steam generator 2 NR level	%	69.06	69.40	± 0.37 %	69.34	69.25	69.28
Nuclear power	%	91.72	91.94	± 0.26 %	91.63	91.78	91.77
Cold leg 1 temperature	K	559.41	559.36	± 0.29 %	560.74	559.15	559.51
Cold leg 2 temperature	K	559.57	559.53	± 0.29 %	560.59	558.99	559.35
Hot leg 1 temperature	K	593.92	593.73	± 0.29 %	594.64	593.23	593.55
Hot leg 2 temperature	K	594.58	594.62	± 0.29 %	594.64	593.23	593.55
Average RCS 1 temperature	K	576.63	576.52	± 0.32 %	577.69	576.19	576.53
Average RCS 2 temperature	K	577.05	577.05	± 0.32 %	577.62	576.11	576.45
Programed Tavg	K	576.90	576.90	± 0.39 %	576.97	576.97	577.00

how the plant would respond to linear power decrease, what would be very difficult with the VALVE component (valve opening is not linear with the steam flow). It should be noted, that this does not happened in the plant, but was just the tactics for achieving steady-state conditions. The nonlinear closing and opening could be performed by VALVE component too, but it would require more time as 5%/minute decrease is the maximum allowed load reduction. Another steady state had to be calculated when TMDPJUN component was replaced by VALVE component representing turbine governor valves.

The reason why simple power reduction scheme was not performed to reduce the power from 100% to 91.72% was that in the case of just lowering the power to 91.72% by inserting rods due to power mismatch between reactor power and turbine power some initial conditions are different from initial conditions when withdrawing rods (see Figures 2(b) and 2(d)). The reason is the deadband in the temperature error signal (between the reference temperature and the auctioneered average reactor coolant system (RCS) temperature). The difference when the rods stop to move in and start to move out is 1.4 K. Such a difference causes difference in the

pressure on the secondary side too (1 K temperature change corresponds to 0.125 MPa pressure change).

Due to rod movement, the reactor power changes as it is shown in Figure 2(a), following the turbine power, which is modelled as a linear function of turbine flow. The RCS average temperature did not decrease immediately as expected when power was decreased but increased in the initial 150 seconds of the second phase (till −2850 seconds) due to delay caused by a combination of loop transport time, resistance temperature detectors manifold arrangement, and instrument processing time (see Figure 2(b)). Then the temperature started to linearly drop to new steady-state value. Same phenomenon repeated at the beginning of the third phase (temperature increase with later decrease). When power is increased the opposite happened. The temperature first decreased and then started to increase at −1530 seconds (the turbine governor valve starts to open at −1700 seconds).

Proportional heaters compensate the pressurizer pressure during power changes. During power decrease, the pressure initially increases and then returns to its nominal value, and vice versa during power increase (see Figure 2(c)). Finally, the steam generator 1 pressure shown in Figure 2(d)

TABLE 3: Time sequence of main events during transient.

Event	Measurement	Calculation
Turbine flow reduction	0 second–5 seconds	0 second–5 seconds
Operator action (start of governor valve opening)	16 seconds	16 seconds
SI signal on low steamline pressure	17 seconds*	16.7 seconds
SI pump injection start	21 seconds	22 seconds
SG power operated relief valve (PORV) opening	27 seconds	31 seconds
AFW flow actuation	42 seconds	42 seconds

*based on 25 seconds delay of AFW actuation.

is increasing during turbine valve closing and decreasing during turbine valve opening. When the turbine valve stops to move, the SG pressure changes the direction and stabilizes at certain value depending on the value of RCS average temperature.

3.2. Part 2 analysis–transient with reactor trip

The time sequence of main events during the transient is shown in Table 3. This time sequence was determined based on the measured data of plant variables. The measured data showed that the turbine governor valves were closing for 5 seconds from 35.5% to 12.2% position, and then stabilized for 12 seconds. When the position starts to increase to 14% (opening caused by operator), there was full closure of turbine valves. The power level showed that the reactor was tripped. The reason for the reactor trip was low steamline pressure generating SI signal. The low steamline pressure signal resulted from the turbine flow increase. As at 15 seconds, the valve position was 12.2% and at 17 seconds was already 14.1% it was assumed that operator starts to open the turbine governor valves at 16 seconds. On SI signal also main feedwater isolation and main steamline isolation valve signal are generated, SI pump is actuated, and letdown and charging are isolated.

It should be noted that the sequence of events was determined from the measured data, which were used for the plots; therefore the values are rounded to seconds. For example, the core power starts to drop after 19 seconds. The exact time of reactor trip could not be determined because delay in signals and rod drop time is not exactly known.

To obtain the correct time sequence of events in short term, it was needed to model the operator actions, resulting in closure and subsequent opening of turbine governor valve. How this influences the steam mass flows from the steam generators number 1 and 2, is shown in Figures 3(g) and 3(h), respectively. Please note that steam flow in the calculations depends on the position of turbine valves and SG PORVs. In the calculation, the turbine valves were closed at 20 seconds while the SG PORVs open at 27 seconds. After the trip, the calculated steam flow was smaller than in the plant. From the measured data, it could be concluded that steam dump was operating after turbine governor valve closure. In the RELAP5 model these systems were not modelled in detail what resulted in small differences.

Figure 3(a) shows the power drop when the reactor is tripped. The measurement of power range channel is based on the neutron flux. After reactor shutdown, only a part of decay heat is due to neutron flux from delayed neutrons and spontaneous fission neutrons. Decay heat comes also from other sources as unstable fission products and unstable actinides. Therefore, the measured neutron flux is lower than in the reality and this is the major reason for disagreement with the calculation. The decay heat is simulated with RELAP5 while the measured data do not show correctly this decay.

The RCS average temperature is shown in Figure 3(b). After transient initiation, the temperature starts to increase until reactor is tripped in 17 seconds. Then the temperature is a function of cooling the primary system (by primary side injection) and the secondary heat sink.

In Figure 3(c) is shown pressurizer pressure. The initial pressure increase is calculated very well. The pressure is rapidly increasing until the pressurizer sprays are actuated. It can be seen that proportional sprays". very efficiently reduce the pressure increase before reactor trip. When the reactor is tripped, the pressurizer pressure further decreased. Initial agreement is very good including peak pressure. However, it can be seen that after 25 seconds the calculated pressure shows repressurization of the primary system. The reason is the difference between calculated and measured steam flows (see Figures 3(g) and 3(h)). It should be noted that in the calculation position of turbine governor valve was simulated till 17 seconds when the valve closed on turbine trip in 3 seconds, while from the plant measured data, the steam flows start to drop at 21 seconds. In the case of calculation termination of steam flow caused SG pressure increase what deteriorated cooling of the primary side resulting in repressurization. However, when secondary side cooling was re-established by SG PORV opening at 27 seconds, the RCS pressure starts to decrease again. In addition, some cooling on the primary side was established by HPIS injection, while in the calculation the injection started in 50 seconds. No adjustment was made in the input model to tune the HPIS injection, SG PORV operation, and steam flows.

The steam generator pressure was calculated very well as shown in Figure 3(e). The first SG pressure peak is due to governor valve closure and the second peak due to the turbine trip. When the operator opened the turbine governor valves, the SG pressure after first peak started to decrease;

TABLE 4: Quantitative results for different time intervals.

	Original FFTBM			FFTBM by signal mirroring		
	AA (−20 seconds– 0 second)	AA (0 second– 80 seconds)	AA (0 second– 1800 seconds)	AA (−20 seconds– 0 second)	AA (0 second– 80 seconds)	AA (0 second– 1800 seconds)
Core power	0.005	0.239	0.234	0.007	0.306	0.304
RCS average temperature	0.000	0.008	0.009	0.000	0.010	0.010
PRZ pressure	0.003	0.041	0.055	0.003	0.050	0.067
PRZ level	0.008	0.144	0.506	0.008	0.180	0.450
SG 1 pressure	0.010	0.087	0.079	0.010	0.115	0.106
SG 1 NR level	0.005	0.236	0.277	0.006	0.350	0.330
SG 1 steam flow	0.018	0.704	0.694	0.020	0.895	0.879
SG 2 steam flow	0.022	0.655	0.652	0.022	0.780	0.787

therefore, SI signal was generated on low steamline pressure. The second peak caused the SG PORV valve opening.

The steam generator levels also agree well initially as shown in Figure 3(f). The reactor trip caused turbine trip and main feedwater isolation. The closure of the turbine valves and core heat transferred to the steam generators resulted in the steam pressure increase (see Figure 3(e)), which had a shrink effect on the steam generator level instrumentation. On SI signal with 25 seconds delay, the AFW injection was started removing the decay heat and filling the steam generators. Following the main feedwater isolation, the steam generator level is affected by auxiliary feedwater and released steam. However, it was observed that in the time period from 26 seconds to 73 seconds, when SG PORV 1 is operated, the calculated level is higher than the measured data. An explanation for this behavior could be in the RELAP5 input model; the damping of the oscillating water flow between the downcomer and the riser in the steam generators is underpredicted.

In the long term, the secondary pressure dictates the transient progression. The measured data for AFW flow were used in the calculation to simulate the operation of AFW pumps. To obtain exact match of SG pressures, small steam flow was modeled also as indicated by the measured data (see Figures 4(g) and 4(h)). Namely, the plant is designed such that after the main steamline isolation after the turbine trip there is some steam flow to the gland steam system. The steam in the steam generators is generated based on the available heat (mostly decay heat). From Figure 4(h), it can be seen that the measured value of steam flow is much higher than the maximum value of generated steam for one steam generator (label "calculation limiting"). Therefore, the steam flow was tuned in such a way to obtain as much as possible good agreement of SG pressures. The value of steam flows in the calculation is physically feasible, but it is not known if it was so in the reality. Also, the transient is very sensitive to this variable. Without assuming any steam flow after reactor trip or assuming measured data for steam flow, the SG pressure would be overpredicted (requiring SG PORV opening) or underpredicted. In the case of tuning steam flows all other calculated variables are in excellent agreement with the measured variables as shown in Figure 4. The measurement

of power range channel is based on the neutron flux as already mentioned; therefore, the measured data are lower than the calculated power based on the decay heat (Figure 4(a)). Due to the steam generator pressure tuning (Figure 4(e)) also the RCS average temperature (Figure 4(b)) and SG level (Figure 4(f)) are closely matched. There is some discrepancy in the pressurizer pressure and level (Figures 4(c) and 4(d)) because the SI flow in the calculation was different from the measured data. It was decided not to tune the calculated SI flow to the measured data (SI pumps operated approx. 5 minutes). Later, the primary system is filled by operation of pressurizer sprays and charging flow.

Important was the finding that RELAP5 computer code calculation suggests some steam flow and later it was found out that there is some larger steam flow to the gland steam system in a special case of steamline isolation after turbine trip, which occurred in the analyzed event. Namely, the gland steam system was not included in the base RELAP5 input model.

3.3. Quantitative assessment

The obtained results shown in Figure 4 were quantitatively assessed using fast Fourier transform based method (FFTBM). Both the original FFTBM [13] and improved FFTBM by signal mirroring were used [14]. Simplified quantitative assessment by applying FFTBM was done to confirm the conclusions done based on the analysis above. The readers not familiar with FFTBM can refer to references [1, 14]. For the purpose of this paper, it is important to know that lower is the average amplitude (AA), higher is the accuracy and that total accuracy below 0.3 means very good calculation. For primary pressure the AA below 0.1 means acceptable accuracy. Table 4 shows the AA for three time intervals, the time interval (−20 seconds–0 second) for steady state, short-term (0 second–80 seconds), and long-term (0 second–1800 seconds) results.

The results for time interval (−20 seconds–0 second) showed that the initial condition is very well predicted. This confirms the results in Table 2, where it is shown that all variables shown in Table 4 are within design accuracy of measuring channels. For the short- and long-term calculation the
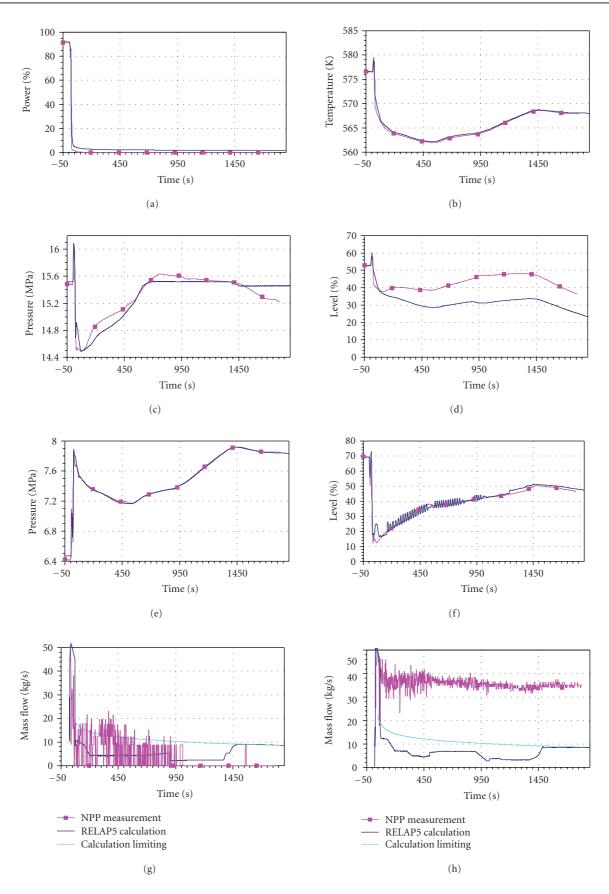
Figure 4: Transient with reactor trip—long term: (a) core power, (b) RCS average temperature, (c) PRZ pressure, (d) PRZ level, (e) SG 1 pressure, (f) SG 1 NR level, (g) SG1 steam flow, (h) SG2 steam flow.

accuracy is rather similar, indicating very good calculation. When comparing original FFTBM and improved FFTBM by signal mirroring, as expected the differences are due to the unphysical edge effect (difference between the first and last data point of the signal) contributing to frequency spectrum in the original FFTBM. When edge is present in the experimental (measured) signal, this gives lower AA in the case of original FFTBM, that is, core power and steam generator narrow range level. For information, how edge effect could be eliminated by signal mirroring, the reader can refer to [14].

4. CONCLUSIONS

In this study, plant measured data for abnormal event resulting in the reactor trip at Krško NPP were used for validation of the RELAP5/MOD3.3 Patch 03 computer code. The analysis was divided into two parts. In the first part, an approach by maneuvering the plant was proposed to achieve steady-state conditions. In the second part, the turbine governor valve closure with reactor trip and the associated operator actions were simulated.

The calculated initial conditions at 91.72% power level were achieved close to the plant initial conditions by just maneuvering the plant. These results suggest that the input model for RELAP5 code is a good representation of the plant. The results of the abnormal event analysis showed good agreement between the calculated and measured data in the short term. This is true also for long term when operator actions are properly modeled.

The limitation of the plant measured data for code validation is that some information was not available or reliable. Namely, the calculated results showed that the transient evolution is very sensitive to the steam flow after reactor trip. In the short term, it would be very valuable to have separate measurements of steam flow to steam dump and through SG relief valve. This would clarify differences in flow a few seconds after reactor trip. Important is the finding that in the long term the measured data indicate steam flow after main steamline isolation. To match the secondary pressure also RELAP5 computer code calculation suggests some steam flow. After investigating design documentation it was found out that there is some steam flow to the gland steam system in a special case of steamline isolation after turbine trip, which occurred in the analyzed event. Namely, the gland steam system was not included in the base RELAP5 input model. But, the study of maximum steam generated based on decay heat showed that measurement of steam flow was not reliable. Therefore, the steam flow was tuned in such a way to obtain close agreement between the calculated and measured steam generator pressure. In this way also all other plant variables agree very well with the plant measured data.

In general, the conclusion is that the RELAP5/MOD3.3 Patch 03 computer code is capable of simulating the abnormal event but it requires qualified input model. In the presented study, proper modelling of operator actions and gland steam system is needed to obtain good quantitative agreement. Finally, the calculated data may be supplemental to the plant measured data when the information is missing or the measurement is questionable.

REFERENCES

[1] A. Prošek, F. D'Auria, and B. Mavko, "Review of quantitative accuracy assessments with fast Fourier transform based method (FFTBM)," *Nuclear Engineering and Design*, vol. 217, no. 1-2, pp. 179–206, 2002.

[2] A. Prošek, F. D'Auria, D. J. Richards, and B. Mavko, "Quantitative assessment of thermal-hydraulic codes used for heavy water reactor calculations," *Nuclear Engineering and Design*, vol. 236, no. 3, pp. 295–308, 2006.

[3] F. D'Auria, "The role of experimental database in the validation of thermalhydraulic system codes," *International Journal of Heat and Technology*, vol. 21, no. 1, pp. 21–30, 2003.

[4] A. Petruzzi and F. D'Auria, "Thermal-hydraulic system codes in nulcear reactor safety and qualification procedures," *Science and Technology of Nuclear Installations*, vol. 2008, Article ID 460795, 16 pages, 2008.

[5] IAEA-TECDOC-1550, *Proceedings of a Technical Meeting on Deterministic Analysis of Operational Events in Nuclear Power Plants*, Dubrovnik, Croatia, May 2005.

[6] P. Groudev and A. Stefanova, "Validation of RELAP5/MOD3.2 model on trip off one main coolant pump for VVER 440/V230," *Nuclear Engineering and Design*, vol. 236, no. 12, pp. 1275–1281, 2006.

[7] A. Prošek, B. Kvizda, B. Mavko, and T. Kliment, "Quantitative assessment of MCP trip transient in a VVER," *Nuclear Engineering and Design*, vol. 227, no. 1, pp. 85–96, 2004.

[8] I. Parzer, "RELAP5/MOD3.3 simulation of MSIV closure events in a two-loop PWR," *Transactions of the American Nuclear Society*, vol. 87, pp. 202–203, 2002.

[9] Information Systems Laboratories, Inc., Nuclear Safety Analysis Division, "RELAP5/MOD3.3 Code Manual, NUREG/CR-5535 Rev. P3," Rockville, Maryland, Idaho Falls, Idaho, USA, March 2003.

[10] I. Parzar, B. Mavko, and B. Krajnc, "Simulation of a hypothetical loss-of-feedwater accident in a modernized nuclear power plant," *Journal of Mechanical Engineering*, vol. 49, no. 9, pp. 430–444, 2003.

[11] A. Prošek, I. Parzer, and B. Krajnc, "Simulation of hypothetical small-break loss-of-coolant accident in modernized nuclear power plant," *Electrotechnical Review*, vol. 71, no. 4, pp. 199–204, 2004.

[12] I. Parzer, "Break model comparison in different RELAP5 versions," in *Proceedings of the International Conference Nuclear Energy for New Europe*, pp. 217.1–217.8, Nuclear Society of Slovenia, Portorož, Slovenia, September 2003.

[13] F. D'Auria, M. Leonardi, and R. Pochard, "Methodology for the evaluation of thermal-hydraulic codes accuracy," in *Proceedings of International Conference on New Trends in Nuclear System Thermalhydraulics*, Pisa, Italy, May-June 1994.

[14] A. Prošek and M. Leskovar, "Improved FFTBM by signal mirroring as a tool for code assessment," in *Proceedings of International Congress on Advances in Nuclear Power Plants (ICAPP '07)*, pp. 7121-1–7121-9, Nice, France, May 2007.

Research Article

Simulation of MASPn Experiments in MISTRA Test Facility with COCOSYS Code

Mantas Povilaitis and Egidijus Urbonavičius

Lithuanian Energy Institute, Laboratory of Nuclear Installation Safety, Breslaujos Street 3, 44403 Kaunas, Lithuania

Correspondence should be addressed to Mantas Povilaitis, mantasp@mail.lei.lt

An issue of the stratified atmospheres in the containments of nuclear power plants is still unresolved; different experiments are performed in the test facilities like TOSQAN and MISTRA. MASPn experiments belong to the spray benchmark, initiated in the containment atmosphere mixing work package of the SARNET network. The benchmark consisted of MASP0, MASP1 and MASP2 experiments. Only the measured depressurisation rates during MASPn were available for the comparison with calculations. When the analysis was performed, the boundary conditions were not clearly defined therefore most of the attention was concentrated on MASP0 simulation in order to develop the nodalisation scheme and define the initial and boundary conditions. After achieving acceptable agreement with measured depressurisation rate, simulations of MASP1 and MASP2 experiments were performed to check the influence of sprays. The paper presents developed nodalisation scheme of MISTRA for the COCOSYS code and the results of analyses. In the performed analyses, several parameters were considered: initial conditions, loss coefficient of the junctions, initial gradients of temperature and steam volume fraction, and characteristic length of structures. Parametric analysis shows that in the simulation the heat losses through the external walls behind the lower condenser installed in the MISTRA facility determine the long-term depressurisation rate.

1. INTRODUCTION

Loss-of-coolant accidents from ruptures in the primary loop of light water reactors (LWRs) are generally fully controlled by the engineered safety systems. Nevertheless, there is a small probability that due to failure of designed emergency core cooling measures during accident, the reactor core could overheat and chemical reaction of steam and strongly overheated zircaloy could produce significant amounts of hydrogen. This hydrogen would then be released into the containment. Without counter measures, the flammable mixtures could then form and cause combustion loads that could threaten the integrity of the containment. The hydrogen combustion had occurred in the containment of Three Mile Island NPP and caused pressure spike of ∼2 bar [1].

Detailed experimental and analytical hydrogen mixing research has been performed at several laboratories and experiment facilities TOSQAN, MISTRA, and THAI in the frame of international standard problem (ISP-47) [2]. Performed analyses identified the phenomena, which should be

further addressed in the code development and what further experiments could be performed to enhance knowledge about hydrogen mixing in the containments.

The installed water sprays could enhance gas mixing in the containments and prevent local accumulation of hydrogen. In order to evaluate the ability of containment modelling codes to simulate the spray behaviour and the interaction with gas atmosphere, severe accident research network (SARNET) initiated the spray benchmark in two test facilities: TOSQAN and MISTRA [1]. Lithuanian Energy Institute participated in the benchmark by simulating MASPn tests performed in the MISTRA facility. The MISTRA spray tests MASP1 and MASP2 concern the depressurisation of the containment atmosphere by spray, while MASP0 is the reference case without spray.

The simulation of MASPn experiments was performed with the lumped-parameter code COCOSYS. Only the measured depressurisation rates during MASPn were available for the comparison with calculations at this stage of benchmark. In this work, most of the attention was concentrated

on MASP0 experiment simulation, since MASP0 is the less complex experiment than MASP1 and MASP2 (sprays are not used during MASP0). Therefore, it was decided to test developed nodalisation, defined initial and boundary conditions and selected modelling parameters by simulating this experiment. When the MASP0 test simulation was performed and acceptable agreement with measured depressurisation rate was achieved then the analyses of MASP1 and MASP2 experiments were performed to check the influence of sprays on the depressurisation rate.

This paper presents a short description of MISTRA facility, specification of MASPn tests performed in this facility, developed nodalisation for COCOSYS code and the obtained results. The performed analysis showed that a clear and detailed specification of initial and boundary conditions of the tests is essential in order to perform the correct simulation of the experiments. The performed parametric analysis revealed the importance of the conditions in the so-called "dead-end" volume behind the condensers, installed in MISTRA test facility.

2. EXPERIMENTS

There were three experiments—MASP0, MASP1, and MASP2—performed in MISTRA test facility. Each MASP experiment followed after an M5 experiment, during which the stratified atmosphere of the containment was created by a centred steam release into the facility and a high-thermal gradient of the temperatures of the condensers. Therefore, initial conditions of the MASP tests were the conditions of the M5 tests steady-states. Temperatures of the condensers during the MASP tests were the same as during the M5 tests.

MASP1 and MASP2 experiments can be divided into two phases—phase of the depressurisation due to the thermal losses (0 second–2100 seconds) and spray phase (2100 seconds–3900 seconds). During the first phase, the pressure of the containment is decreasing only due to thermal loses through the external walls of the facility and steam condensation on the lower condenser. During the second phase, water sprays are activated and the dominant processes affecting depressurisation is steam condensation on the water droplets and atmosphere mixing. MASP0 experiment is a reference case and only has one phase—depressurisation due to the thermal losses (0 second–3900 seconds). Detailed description of experiments can be found in [3].

2.1. MISTRA test facility

MISTRA facility is a vertical stainless steel cylindrical vessel with curved bottom (Figure 1). The free volume of the cylinder is $\sim$99.5 m^3, internal diameter -4.25 m, maximal internal height -7.38 m. Vessel is thermally insulated with 20 cm of rock wool. Three cylinders with controlled surface temperature, called condensers, are inserted inside the vessel. Inner diameter of every condenser is equal to 3.8 m. The condensate is collected by gutters. Condensers are situated between 1.285 m and 7.28 m of cylinder height. Condensation occurs only on surfaces of condensers facing the inside of MISTRA facility. Total condensing surface is about
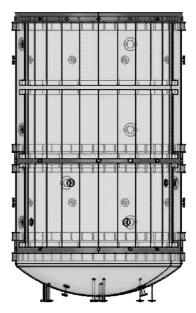

FIGURE 1: Schematics of MISTRA test facility [1].

69 m^2. Outside surfaces of the condensers are insulated with 2 cm synthetic foam layer. There is some space, the so-called "dead volume," between condensers and facility walls. Vertical spaces between condensers ($\sim$0.12 m) are partially hidden by gutters. Further description of MISTRA facility can be found in [3, 4].

2.2. Experimental results

During the MASP tests phase of the depressurisation due to thermal losses containment pressure dropped from the initial value of 2.4 bar to $\sim$2.2 bar in the first $\sim$500 seconds and then was slowly decreasing (Figure 2) [3]. At the end of MASP0 experiment ($\sim$4000 seconds) the pressure had decreased down to $\sim$2.03 bar. During MASP1 and MASP2 tests the sprays were activated after 2100 seconds. Until this time, the pressure behaviour in all three cases was very similar and small differences were caused by the different conditions that had appeared after each M5 test. After spray activation, a rapid depressurisation was observed. In the MASP1 experiment, the pressure after 4000 seconds was $\sim$1.6 bar and in the MASP2 experiment it was $\sim$1.45 bar. The different final pressures of the MASP1 and MASP2 experiments spray phase were due to the different temperatures of injected water (Table 1). Lower spray water temperature induced a larger containment pressure decrease.

3. NODALISATION SCHEME, INITIAL AND BOUNDARY CONDITIONS

Experiments were simulated with lumped-parameter code COCOSYS version V2.3v11 [5]. Developed nodalisation scheme of the MISTRA test facility (Figure 3) consisted of 31 nodes, which were connected by 50 atmospheric junctions. Water film flow along condensers was modelled with 4 junctions. Condensers were simulated by 14 structures, walls of
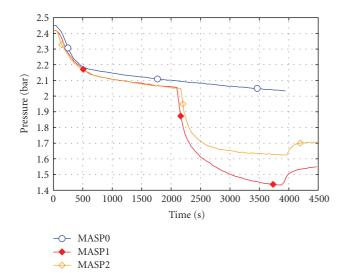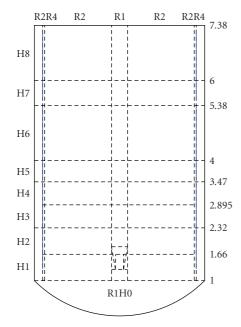
FIGURE 2: Experimental results [3].

FIGURE 3: Nodalisation scheme for COCOSYS code.

TABLE 1: Benchmark specifications—Part A [1].

Parameter	MASP0	MASP1	MASP2
Pressure	2.4 bar	2.4 bar	2.4 bar
Mean gas temperature	124°C	124°C	124°C
Steam volume fraction	0.45	0.45	0.45
Air mass	~115 kg	~115 kg	~115 kg
Water temperature in the nozzle	—	40°C	60°C
Droplets mass flow-rate	—	0.87 kg/s	0.87 kg/s
Temperature of lower condenser	80°C	80°C	80°C
Temperature of medium and upper condensers	140°C	140°C	140°C

Nodalisation scheme includes 3 radial nodes in the central part of the containment and one in the "dead volume" behind the condensers. There are 8 vertical levels with detailed radial subdivision. A single node defined below the lower condenser simulates the sump. The heat transfer through convection, radiation, and condensation is considered. Outer sides of the facility walls in the model were kept at room temperature during whole simulations. COCOSYS code is capable of calculating gradients of temperature inside the wall from this external condition and conditions in the control node the wall is facing.

For the simulation of MASP1 and MASP2 experiments, several paths of the falling spray droplets were identified according to nodalisation. Fraction of the total water inlet mass flow of the spray system related to each spray path was calculated according to the part of the base area of the cone, which corresponds to a given path. The spray droplet size distribution was not given in the specification; a value of around 1 mm was specified [3]. The spray model, which is implemented in COCOSYS code, simulates only monodisperse droplets, that is, does not allow defining a droplet size distribution.

4. CALCULATIONS

Simulations of the experiments in the MASPn benchmark were performed in two parts: (1) part A, where only mean values of gas temperature and steam volume fraction were specified (Table 1), and (2) part B, where the steam content and temperature stratification conditions were specified.

At first, the initial and boundary conditions for the base case calculations were set according to the part A specification [1], where the gas stratification was not identified. Temperature of the external sides of the facility walls was set equal to 20°C. When using mean gas temperature and mean steam volume fraction as homogenous initial conditions for vessel volume, the calculated pressure drop in MASP0 case was too high compared to the experimental results (Figure 4). Calculations showed that after 4000 seconds the pressure would drop to almost 1.8 bar, but in experiment it was still higher than 2 bar. This result shows that it is not possible to model MASP tests using homogenous initial

containment—11 structures. This nodalisation scheme was developed on the basis of the MISTRA facility nodalisation, which was used in the frame of ISP-47 [2]. In order to simulate the temperature and steam fraction gradients in more detail the previous nodalisation was refined. In the current nodalisation, there are four vertical subdivisions at the level of lower condenser instead of two in the previous ISP-47 nodalisation because the level of lower condenser corresponds to a region between 1 m and 4 m of the facility height and the gradients of both temperature and steam volume fraction are created in this region. Regions of middle and upper condensers were left subdivided into two vertical parts.

FIGURE 4: Pressure evolution using homogenous initial conditions.

FIGURE 6: Relative humidity obtained with conditions from part B specification.
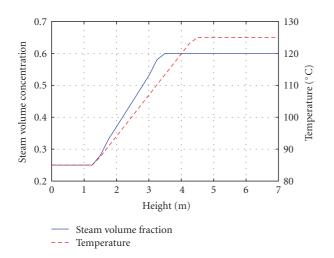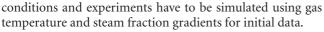
FIGURE 5: Additional experimental data in part B specification [6].
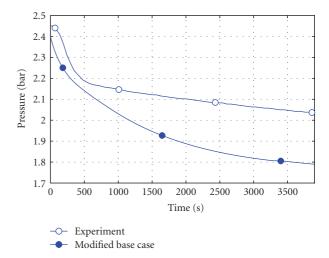
FIGURE 7: Pressure evolution with decreased steam volume fraction at low elevation.

conditions and experiments have to be simulated using gas temperature and steam fraction gradients for initial data.

Stratifications of steam content and gas temperature specified in part B are presented in Figure 5 [6]. One can see that after M5 test the temperature gradient is created between elevations of 1.25 m and 4.5 m. Temperature difference in this region is 40°C. The stratification of steam volume fraction changes from 0.25 at elevation of 1.25 m to 0.6 at elevation of 3.5 m.

Therefore, MISTRA nodalisation was modified to include gradients from the part B specification (Figure 5) [6]. But it was not possible to perform calculations using these conditions because they correspond to the relative humidity greater than 100% at low elevations of the facility (Figure 6). Nevertheless, it should be noted that with such temperature and steam volume fraction distribution, the calculated mass of air in the facility was 115.7 kg and corresponded to the test specification (see Table 1).

Considering that better definition of experimental boundary conditions was not available at the moment, when
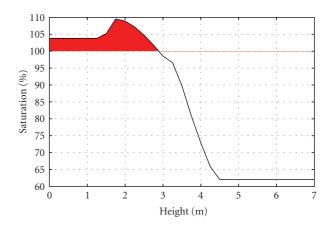
analysis was performed it was decided to perform parametric analyses with slightly modified conditions in order to start calculations and study the effect of these conditions on the results. As well there were performed several analyses to study the effect of modelling assumptions.

At first, it was chosen to reduce the steam volume fraction at lowest elevations of the facility from 25% to 20%. This reduced saturation in the lower part of the facility below 100% and allowed to start calculations but the obtained depressurisation rate (Figure 7) was not much different from the one received assuming homogeneous mixture in the facility (Figure 4), that is, they are significantly different from the experimental values.

The next step was to investigate the influence of modelling parameter—loss coefficient in junctions—on the depressurisation rate. In COCOSYS code, the atmospheric junctions are described by junction area, hydraulic length, and loss coefficient. Area of the junction is unambiguously defined by dividing volume of the facility into the calculation nodes. Hydraulic length is selected as distance between the

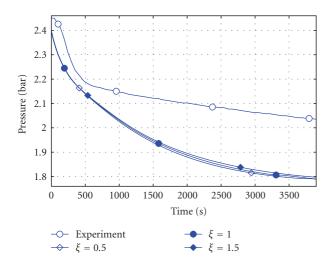Figure 8: Pressure evolutions with different loss coefficients.

Figure 9: Pressure evolutions with different initial parameters.

Figure 10: Pressure evolutions with different characteristic length values.

centres of the nodes connected by the junction. The loss coefficient was selected equal to the value of 1.0 in the base case for all junctions. The loss coefficient is not very well defined in this model because there are no obstacles for gas flow and mass transfer takes place between virtually divided volumes. With the purpose of evaluating the influence of this parameter additional calculations were made, where the value of the loss coefficient was changed to 0.5 and 1.5 as different variants. The results showed that variation of the loss coefficient in junctions does not influence the results significantly (Figure 8) and could not be the reason for large differences between calculations and experiments.

Later it was decided to perform variation of initial temperature and steam volume fraction at lower and upper elevations since these measurements of these parameters include some uncertainty. At first the temperature in the lower part of the containment was defined to be 85°C instead of 87°C, then the steam fraction at low elevations was defined to be 18% instead of 20% and then the steam fraction at high elevations was defined to be 55% instead of 60%. These values were taken considering the measurement errors. Only results of the variant with 55% of steam volume fraction at high elevations showed more different pressure evolution (Figure 9). But the containment pressure was still too low compared with experiment and, furthermore, such change of the gas content changed the air mass of the facility and it became noncompliant with the test specification.

Structures of the facility in the developed model are described by the area of the structure, applicable models of the heat transfer (convection, condensation, and radiation), composition of the structure, and the characteristic height and length. The characteristic length of the structure is not well defined in the modelling methodology. According to COCOSYS user's manual [5], it is defined as $1 = A/U$, where A is an area of the structure, and U is its perimeter, but for the vertical walls the characteristic length should be equal to the height of the wall. Also, according to this user's manual, for the simulation of real power plants the value of 0.01 can be used for all vertical walls. During simulations
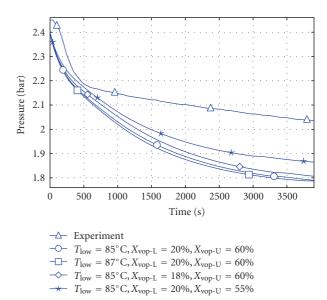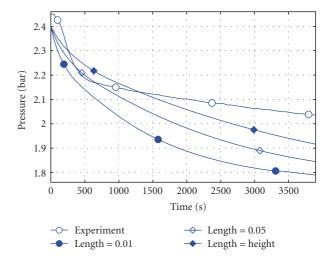
of aerosol deposition in the KAEVER experimental facility, the value of 0.05 for all vertical walls was determined as best for simulation of aerosol deposition [7]. Since the value of the characteristic length is not very clear, it was varied to investigate its influence on the calculation results. The performed analysis showed that this parameter had significant influence on results, but the calculated pressure was still too low compared to experiment (Figure 10). The variation of this parameter led to 0.1 bar pressure difference at the end of calculations. As well it should be noted that changing this parameter does not give initial faster pressure drop and slower decrease after 500 seconds.

The last tested assumption was simulation of the external walls of the test facility. The calculations were performed assuming that there are no external walls, that is, the depressurisation in the MASP0 case is determined only by
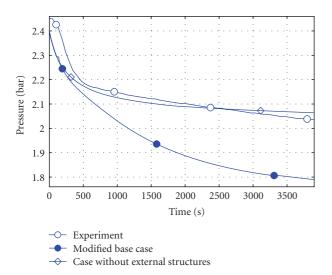
FIGURE 11: Comparison of pressure evolutions calculated from base case and calculated without external structures, MASP0.

FIGURE 12: Pressure evolutions calculated with decreased junction area behind lower condenser.

the heat transfer to the lower condenser. The obtained results showed that the calculated depressurisation rate is similar to the measured (Figure 11). After further examinations, it was determined that only structures behind the lower condenser, which is colder than the other condensers, determined the heat loss through external structures and the depressurisation rate in the long-term.

For the final analysis of all MASPn experiments, it was decided to simulate all structures, but to decrease the area of the junction behind the lower condenser. This leads to a decrease of gas flow and, consequently, the heat transfer at this part of the facility. The area of the junction was selected in such a way that the calculated depressurisation rate due to heat loses, that is, MASP0 test, comply with the measured results best. The characteristic length of all structures was assumed 0.01 m. In the case of the MASP0 experiment, pressure reaches ~2.2 bar at ~500 seconds and stays a bit over 2 bar at ~4000 seconds (Figure 12), that is, results are similar to the experimental. When this MASP0 test simulation was performed and acceptable agreement with measured depressurisation rate was achieved (Figure 12), simulation of MASP1 and MASP2 experiments was performed to check the influence of the sprays. The same modelling assumptions and conditions as in MASP0 test simulation were used. Sprays were modelled with previously described assumptions. Mass flow rate of the droplets and water temperature in the nozzle were set according to specification (Table 1). Results of the calculations showed that at the end of the spray phases obtained pressure values are similar to the experimental ones in both tests, but in the beginning of the spray phase the pressure decreases too slow compared to the experiment and, accordingly, too fast in the second part of the phase. The performed analyses show that more modelling efforts and clear definition of initial and boundary conditions of experiments are required even for lumped parameter codes in order to perform a detailed and reliable modelling of the experiments. In the future, the calculations of tests will be
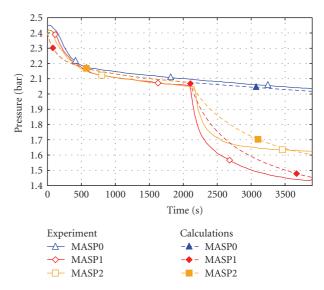
performed by modelling M5 experiment, which preceded MASPn tests. When the M5 experiment is simulated and calculated stratification conditions fit the measured values then the detailed analysis of sprays on the destruction of atmosphere stratification could be estimated.

5. CONCLUSIONS

The analysis of MASPn experiments was performed using the lumped-parameter code COCOSYS. The influence of different experimental parameters and modelling assumptions was investigated in order to determine the most important parameters that influence the depressurisation rate during the MASP0 experiment performed in the frames of spray benchmark in MISTRA test facility.

The performed analysis showed that a clear definition of the initial and boundary conditions, including developed gas stratification, of the experiment is required in order to develop a nodalisation, which could be used for simulation of experiments.

None of the considered modelling parameters (loss coefficient in the junctions, characteristic length of structure) had major influence on the calculated results.

Variation of the atmosphere stratification conditions could not reproduce the measured depressurisation rate.

The performed simulations of MASPn experiments and obtained results show that the calculated heat losses through the external walls behind the lower condenser installed in the MISTRA facility determines the long-term depressurisation rate.

REFERENCES

[1] J. Libmann, *Elements of Nuclear Safety*, EDP Sciences, Les Ulis Cedex, France, 1997.

[2] "International Standard Problem ISP47 on containment thermal-hydraulics, Final report," Nuclear Energy Agency, NEA/CSI/R(2007)10, September 2007.

[3] D. Abdo, R. Tomassian, J. Brinster, D. Roumier, I. Tkatschenko, and J. L. Wid-Loecher, "M5-MASP MISTRA experimental results," SFME/LTMF/RT/06-006/A, 2006.

[4] J. Malet, E. Porcheron, J. Vendel, L. Blumenfeld, and I. Tkatschenko, "SARNET spray benchmark: TOSQAN and MIS-TRA specification report," 2006.

[5] H.-J. Allelein, S. Arndt, W. Klein-Heßling, S. Schwarz, C. Spengler, and G. Weber, "COCOSYS: status of development and validation of the German containment code system," *Nuclear Engineering and Design*, vol. 238, no. 4, pp. 872–889, 2008.

[6] L. Blumenfeld and I. Tkatschenko, "Benchmarking of CFD and LP codes for spray systems in containment applications: MASP tests PART_HYDRO_B: Complementary information," 2006.

[7] S. Schwarz, "Impact of the heat transfer on the aerosol results," COCOSYS Tips & Tricks, Tip 2003-001, Revision 1, Gesellschaft für Anlagen- und Reaktorsicherheit (GRS) mbH, September 2003.

Research Article

Analysis of TROI-13 Steam Explosion Experiment

Mitja Uršič and Matjaž Leskovar

Reactor Engineering Division, Jožef Stefan Institute, Jamova cesta 39, 1000 Ljubljana, Slovenia

Correspondence should be addressed to Mitja Uršič, mitja.ursic@ijs.si

The prediction of steam explosion inducing loads in nuclear power plants must be based on results of experimental research programmes and on simulations using validated fuel-coolant interaction codes. In this work, the TROI-13 steam explosion experiment was analysed with the fuel-coolant interaction MC3D computer code. The TROI-13 experiment is one of several experiments performed in the TROI research program and resulted in a spontaneous steam explosion using corium melt. First, the TROI-13 premixing simulations were performed to determine the initial conditions for the steam explosion simulations and to evaluate the melt droplets hydrodynamic fragmentation model. Next, a number of steam explosion simulations were performed, varying the steam explosion triggering position and the melt droplets mass participating in the steam explosion. The simulation results revealed that there is an important influence of the participating melt droplets mass on the calculated pressure loads, whereas the influence of the steam explosion triggering position on the steam explosion development was less expressive.

1. INTRODUCTION

A steam explosion in a nuclear power plant may develop when the molten corium interacts with the water inside the reactor vessel or in the reactor cavity. During the fuel-coolant interaction (FCI), the corium thermal energy is intensively transferred to the water. The water vaporizes at high pressure and expands, doing work on its surroundings. Although the steam explosion has a low probability of occurrence, it is an important nuclear safety issue in case of a severe reactor accident. Namely, the high pressures occurring during a steam explosion can potentially induce severe dynamic loadings on surrounding safety relevant systems, structures, and components of the nuclear power plant. One of the most severe potential consequences of an ex-vessel steam explosion in a nuclear power plant is an early containment integrity loss, which can lead to an early radioactive material release into the environment. [1]

The prediction of steam explosion induced loads must be based on results of experimental research programs (e.g., TROI, KROTOS, FARO) and on simulations using validated FCI models (e.g., MC3D, IKEMIX, COMETA). Experiments provide experimental data for the steam explosions fundamental issues investigation, the structural loadings evalu-ation, and the severe accident management improvement. Since the experimental results are in general not directly applicable to reactor conditions, above all due to the different scales, FCI models are needed for experimental findings extrapolation to reactor conditions. To be able to make reliable predictions, the FCI models have to be validated on experimental data. In the complex FCI phenomenon, multiple processes are involved during the different steam explosion stages, that is, premixing (corium fragmentation when mixing with water), steam explosion triggering, explosion propagation (the corium thermal energy is converted into coolant thermal energy), and expansion (the coolant thermal energy is converted into mechanical energy), which have to be adequately modelled. The modelling contributes to the FCI phenomenon understanding and highlights issues that are not well understood or require further experimental investigation and model validation. Only adequate FCI processes and consequences understanding enable the FCI codes development to a sufficient high level, appropriate for steam explosion risk assessment in nuclear power plants. [2–4]

Among several experiments performed in the TROI research program, the TROI-13 FCI experiment was chosen for the simulation with the FCI computer code MC3D. The

TROI-13 experiment was selected since in this experiment the steam explosion occurred spontaneously and resulted in the strongest explosion among the TROI experiments performed with corium melt. The purpose of the performed analysis was to establish the modelling capabilities of the MC3D code and to get additional insight into the complex FCI phenomenon.

As follows, first, the description of the TROI facility and the main TROI-13 experimental results is provided. Next, the simulation results of the TROI-13 steam explosion experiment are being presented and discussed in comparison with the experimental measurements. Finally, conclusion remarks are given.

2. TROI-13 EXPERIMENT SET UP AND RESULTS

Test for real corium interaction with water (TROI) is one of the research programs, which was established to provide experimental data to investigate the steam explosions fundamental issues, to enable the structural loadings evaluation, and to improve the severe accident management in nuclear power plants. The program started in 1997 at Korea Atomic Energy Research Institute (KAERI). [5]

As shown in Figure 1, the TROI facility has a 3D geometry and consists of a furnace vessel, a pressure vessel, and a sliding valve. The furnace vessel contains a cold crucible (copper tubes), a release assembly (plug and puncher), and instrumentation for transient pressure (designator FSVP) and melt temperature (pyrometer) measurements. The melt is prepared in the cold crucible. The sliding valve is opened after the melting is completed. The melt is being released when the plug is removed and the puncher breaks the crust formed at the melt bottom. The puncher actuation time is the starting time for the dynamic data acquisition system and the camera. The melt is delivered into the pressure vessel, which contains the test section and the instrumentation for the measurement of the coolant temperature (designator IVT), the dynamic pressure in the coolant (designator IVDP), the dynamic load at the test section bottom (designator IVDL), the atmosphere temperature (designator PVT), the transient pressure (designator PVSP), the dynamic pressure (designator PVDP), the gas sampling (designator GAS), and the visualization (cameras). The melt is poured into the water inside the test section, which is 150 cm high and has an inner diameter of 60 cm. Due to FCI, a steam explosion may develop inside the test section. [5]

Among several experiments performed in the TROI facility, the TROI-13 experiment was chosen for the simulation with the MC3D code (Section 3). In the TROI-13 experiment, a eutectic corium composition was used. The mass fraction of UO_2 was 70%, and the mass fraction of ZrO_2 was 30%. In the crucible, 13.7 kg of corium were heated to a temperature of nearly 3500 K. Melted corium with the mass 7.735 kg was then poured into the test vessel, which was filled up to 67 cm with water at a temperature 292 K. The free fall height of the molten corium was 3.8 m. The free volume of the pressure vessel was 8.032 m³, and the initial air pressure was 0.108 MPa. [5]
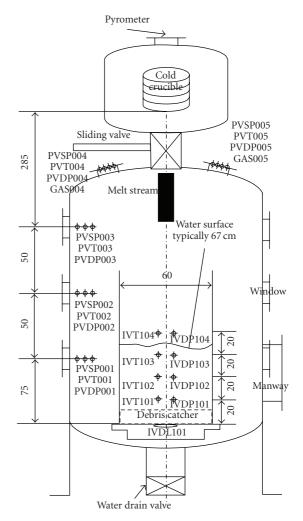
FIGURE 1: Schematic diagram of TROI facility (not in scale; unit in cm) [5].

In the TROI-13 experiment, a spontaneous steam explosion occurred. The steam explosion energy conversion ratio from thermal to mechanical energy was 0.4%. The steam explosion started at about 1220 milliseconds, when the jet reached the test vessel bottom. A pressure peak of 7 MPa and duration of 1 millisecond was measured at 1224 milliseconds. At the test vessel bottom, the dynamic load was measured. The dynamic force was higher than 250 kN, and the duration of the pressure load was about 15 milliseconds. The most important TROI-13 experimental measurements results are summarized in Table 1. In Table 1, also specific results of some other TROI experiments, which had a similar experimental set up as the TROI-13 experiment, are given. [5]

As seen in Table 1, not all experiments resulted in a spontaneous explosion. Based on the TROI experimental program and other comprehensive experimental programs (e.g., KROTOS, FARO), one can conclude that the explosivity of the premixture and the strength of the steam explosion depend on a number of conditions [2, 4], the most important are the following:

TABLE 1: Selected experimental results from TROI facility [5]. SDM is the mean Sauter diameter of the debris, $X_{<0.425\,mm}$ is the mass fraction of debris particles whose size was lower than the sieve size of 0.425 mm, SE indicates whether a spontaneous steam explosion occurred or not, $p_{dynamic}$ is the dynamic pressure peak, and F is the dynamic force peak at the test vessel bottom.

Result	Unit	TROI-9	TROI-10	TROI-11	TROI-12	TROI-13	TROI-14
SDM	mm	1.87	1.08	2.99	0.68	0.71	0.81
$X_{<0.425\,mm}$	%	2.3	8.7	0.5	20.9	18.9	15.7
SE	N/A	No	Yes	No	Yes	Yes	Yes
$p_{dynamic}$	MPa	N/A	No data	N/A	1.0	7.0	0.8
F	kN	N/A	No data	N/A	210	250	210

(i) melt material properties (the energy conversion ratio in steam explosion experiments with prototypic materials was one order of magnitude lower than with stimulant materials),

(ii) melt pouring mode (multiple pours form a more extended premixture than single pours),

(iii) system confinement (confined systems allow more time for heat transfer between the melt and coolant),

(iv) water subcooling (with higher water subcooling, the premixture void fraction is lower, resulting in a stronger steam explosion),

(v) noncondensable gases (noncondensable gases hinder the direct melt water contact, reducing the explosivity of the premixture),

(vi) system pressure (with a higher system pressure, the vapour film around the melt droplets becomes more stable, reducing the explosivity of the premixture).

3. SIMULATION OF TROI-13 EXPERIMENT

The TROI-13 experiment was simulated and analyzed with the computer code MC3D, version 3.5, patch 3 [6, 7]. MC3D is being developed by IRSN, France. MC3D is built mainly for the complex FCI phenomenon evaluation. MC3D has two main applications, which are being developed for the premixing and steam explosion calculations. The geometry model of the TROI-13 experiment, which was used for the premixing and steam explosion simulation, is given in Figure 2.

The melt description in the MC3D premixing application is made with three fields, describing the continuous corium, the melt droplets, and the melt fragments. The corium continuous field is used to describe the corium jet. The second field corresponds to the melt droplets (order of cm in diameter) issued from the jet fragmentation. The last field is used to describe the melt fragments (less than $100\,\mu$m in diameter) issuing from the melt droplet fine fragmentation. In the TROI-13 premixing simulation, the melt fragment field was not taken into account, since in the TROI experiments the amount of melt fragments smaller than 0.425 mm was small if the steam explosion did not occur (Table 1). The relations of jet fragmentation and coalescence are used to describe the mass transportation between the continuous corium and the melt droplets field. Inside the melt droplets
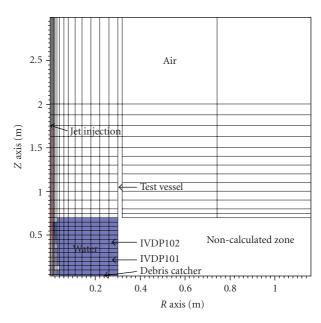
FIGURE 2: Geometry and mesh of the TROI-13 experiment model.

field, the melt droplets hydrodynamic fragmentation is driven by the coarse drop break up process. [6]

The appropriate melt droplets amount determination during the premixing simulation is important, since the melt droplets drive the heat transfer and also present the source for fine fragmentation in the MC3D steam explosion application [6].

In the simulations, the creation of the noncondensible hydrogen during the interaction of corium with water vapor was not modelled. Noncondensible gases in general reduce the strength of the steam explosion since they increase the premixture void fraction and hinder the direct melt water contact [2].

3.1. Premixing simulation

The initial conditions for the premixing simulations were obtained or estimated based on [5]. The jet was injected at a height of 1.75 m with a velocity of 7.35 m/s and a diameter of 2 cm [5, 8]. The MC3D default or recommended numerical and model parameters values were used as far as possible in the premixing simulation, although information from [5, 8, 9] was used to estimate those

simulation parameters which could have an influence on the jet fragmentation mechanisms, the coalescence process, the melt droplets hydrodynamic fragmentation, and the melt droplets solidification effects.

Both, the jet fragmentation and the coalescence processes depend on the molten corium material properties, which had to be defined reasonably. First, the appropriate poured molten corium temperature (T_{jet}) was established, since the experimental measurements of T_{jet} were not reliable. On one hand, the measured melt temperature was given to be 2600 K, what is below the corium solidus temperature, but on the other hand, the temperature was estimated to be most probably near 3500 K or even higher [5]. Therefore, the temperature of 3300 K was chosen, based on the simulations performed in the scope of the OECD program SERENA [8]. Next, the appropriate temperature ($T_{\text{sol-liq}}$), below which the melt droplets fragmentation and coalescence is suppressed due to droplets solidification, had to be determined. In the MC3D code, the temperature $T_{\text{sol-liq}}$ presents the threshold temperature below which the melt droplets are treated as solid spheres. In MC3D, the melt droplets temperature is defined with the melt droplets bulk temperature. So, if the melt droplets bulk temperature is higher than $T_{\text{sol-liq}}$, the melt droplets are treated as liquid, allowing droplets fragmentation and coalescence, otherwise the melt droplets are treated as solid. The droplets bulk temperature is a good measure for the droplets solid/liquid state only if the melt inside the droplet is well mixed. However, it is believed that the melt inside the droplet is not well mixed, and that consequently, a solid crust forms on the droplet much earlier than the droplets bulk temperature decreases below the solidification temperature [9]. Since in MC3D the droplets crust formation is not modelled, for $T_{\text{sol-liq}}$ a temperature higher than the default corium solid temperature 2800 K has to be taken. We decided to perform our simulations using for $T_{\text{sol-liq}}$ the temperature 2820 K, where corium is still liquid and which is only slightly higher than the default one.

For the melt droplet hydrodynamic fragmentation, the coarse drop break up model is used in the MC3D code. The model is based on wave crest stripping followed by catastrophic break up, and depends on the Weber's number (We). If the melt droplets We are above the critical value (We$_{\text{crit}}$), then melt droplet hydrodynamic fragmentation could occur. Below We$_{\text{crit}}$, internal forces inside the melt droplet cannot overcome the cohesive forces of the melt droplet surface tension and the hydrodynamic fragmentation stops. For We$_{\text{crit}}$, the most commonly used value 12 was taken. The coarse drop break up correlation used in MC3D should hold only for We above 350. For We below 350, two additional damping functions are introduced to take into account also other hydrodynamic fragmentation modes presented at lower We. The first damping function is introduced for We below 20, and the second damping function for We below 350. A sensitivity study was performed to evaluate the damping functions influence on the premixing results (Figure 3). [6]

On Figure 3(a), the simulated mean Sauter diameter (SDM) results are given. SDM is defined as the mean sphere diameter that has the same volume/surface area ratio as
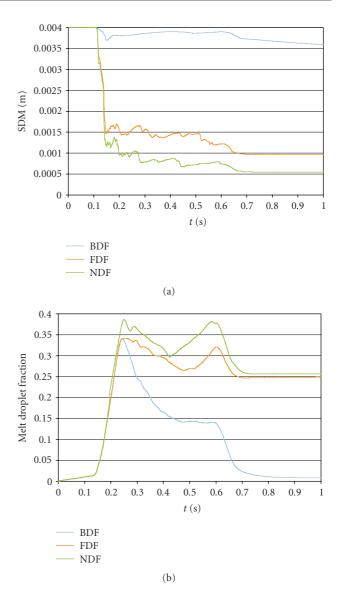

(a)

(b)

FIGURE 3: Mean Sauter diameter (SDM) history (a) and melt droplets fraction history (b) for TROI-13 premixing simulations using different melt droplets fragmentation modelling options.

the particles of interest. Based on the nonexplosive TROI-9 experiment, a SDM of around 2 mm could be expected in the premixing phase (Table 1). In the case of the nonexplosive TROI-11 experiment, SDM was overestimated since part of UO$_2$ pellets was not fully melted. The comparison of simulation results with the experimental results in Table 1 indicates that the use of both damping functions (designator BDF—both damping functions) overestimates SDM. If both damping functions were suppressed (designator NDF—no damping function), SDM was strongly underestimated due to the hydrodynamic fragmentation process overestimation. By suppressing, only the second damping function SDM is still underestimated (designator FDF—first damping function). The SDM values for FDF were around 1.5 mm as long as the effect of the melt droplets coalescence did not become dominant. Therefore, one can conclude that the simulated

SDM for case FDF is in reasonable agreement to the expected 2 mm in the nonexplosive cases. The final SDM decrease (to around 1 mm in case FDF) was due to the coalescence of larger melt droplets, which were still liquid at the end of the premixing phase. The results indicate that there is a need for further investigation of the melt droplet hydrodynamic fragmentation modelling.

Additionally, Figure 3(b) shows also the melt droplets fraction with regard to the total injected corium jet mass. The melt droplets coalescence was estimated to be low in TROI-13-like experiments, since no information about an observed cake was given in [5]. Although it was expected to achieve a low coalescence with the increased $T_{sol-liq}$ (from the default 2800 K to 2820 K) and by selecting the lower T_{jet} (SERENA value 3300 K instead of quite probable 3500 K or even higher), the coalescence still remained important once the jet reached the test vessel bottom at premixing time around 0.25 second (Figure 3). Since the steam explosion occurred already before the coalescence could become significant, we did not try to improve the coalescence modelling in our premixing simulations. As seen on Figure 3, the suppression of damping functions (FDF, NDF) strongly influences the SDM values and the coalescence. The coalescence reduction for smaller melt droplets could be explained with more extensive melt droplets freezing, since frozen droplets cannot coalescence. The coalescence was overestimated in all simulated cases if compared to the experimentally observed low coalescence. A way to improve the coalescence behavior is to improve the melt droplet solidification model.

3.2. Initial conditions for explosion simulation

The initial conditions inside the test vessel for the TROI-13 steam explosion simulations were determined based on the FDF premixing simulation case (Figure 4), where the agreement with experimental measurements was the best. The steam explosion was triggered at premixing time 0.25 second, which was selected based on general experimental observations that a spontaneous steam explosion usually triggers by the contact of the molten corium with the bottom of the test vessel.

In the explosion simulation, the area of water inside the test vessel was initially divided into three zones (interaction zone, trigger zone, and bulk zone). It was estimated from the premixing results (Figure 4) that the interaction zone extends from the water surface (0.70 m) to the test vessel bottom (0.03 m) and has a radius of 4 cm. A homogenous distribution of the melt droplets, vapour, and water was set. The volume fraction of melt droplets in the interaction zone was determined based on the corium jet mass entered in the water at time 0.25 second ($\sim$1.9 kg). The volume fraction of melt droplets participating in the steam explosion was varied in the performed simulations to consider the influence of the incomplete jet break up and the influence of droplets freezing. Based on the premixing simulation, the molten droplets temperature and diameter were set to 3150 K and 1.6 mm (Figure 3). The vapor volume fraction 0.43 and the vapor temperature 2760 K inside the interaction zone were set to values estimated from premixing results. Since the
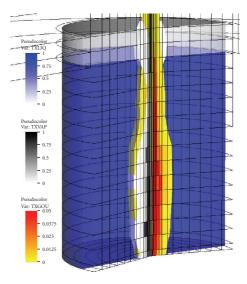

FIGURE 4: Volume fractions of water (TXLIQ), vapor (TXVAP), and melt droplets (TXGOU) inside the test vessel at triggering time in the premixing simulation.

sum of the volume fractions must be 1 by definition, the water volume fraction inside the interaction zone was set according to the vapor and melt droplets volume fractions. The water temperature in the interaction zone was set to 310 K and was also estimated from premixing results. The steam explosion triggering was modelled with a trigger zone placed inside the interaction zone at the central axis. The conditions in the trigger zone were set reasonable according to the interaction zone conditions. The triggering pressure of 1 MPa was chosen based on a sensitivity study, where the triggering pressure influence on the steam explosion results was investigated. It turned out that the triggering pressure has a negligible influence on the simulation results if set inside a reasonable range. The position of the trigger zone in vertical direction was varied to establish the influence of the assumed trigger location on the steam explosion development. In the bulk zone, only water and vapor were present. The vapor volume fraction in the bulk zone was estimated from the premixing results and was set to 0.01. The water temperature in the bulk zone was set to the initial premixing water temperature (292 K) and the vapour temperature to the saturation temperature. In the simulation, also the increase of the water level, due to the presence of the jet and vapor in the premixture, was taken into account based on premixing results.

3.3. Results of explosion simulation

The main steam explosion simulations results are given on Figure 5. Additionally, also a part of the experimentally measured dynamic pressure, digitalized from [5], is shown for comparison. The time delay between the calculated and measured pressure peak on Figure 5 should not be taken into consideration, since in the experiment pressure fluctuations occurred already before the strong pressure escalation, and so the time shift depends on the definition of the spontaneous
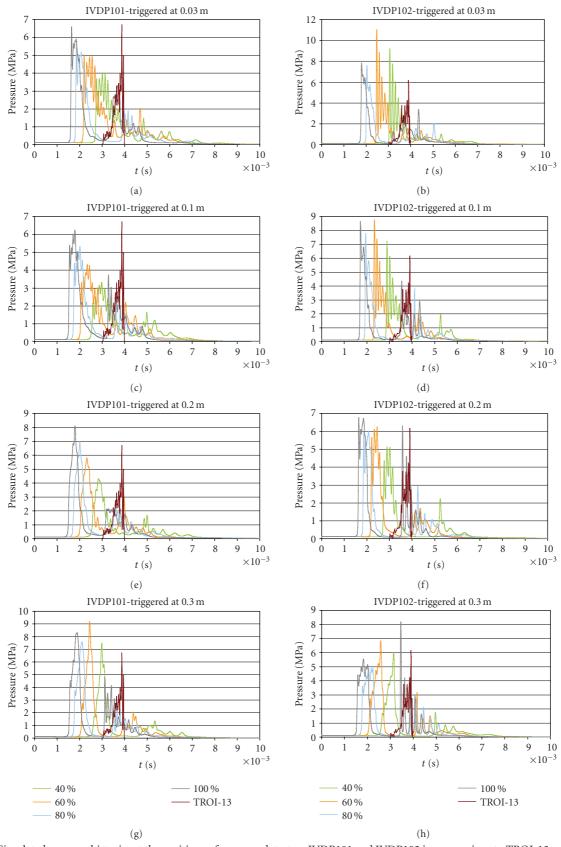
FIGURE 5: Simulated pressure histories at the positions of pressure detectors IVDP101 and IVDP102 in comparison to TROI-13 experimental measurements. Triggering was performed at positions 0.03, 0.1, 0.2, and 0.3 m. The melt droplets mass involved in the steam explosion is given as 40%, 60%, 80%, and 100% fractions of the total corium mass entered in the water at the steam explosion triggering time. Time zero on the figures corresponds to steam explosion triggering.

FIGURE 6: Calculated pressure field inside the test vessel between 0.5 and 3 milliseconds with time step 0.5 millisecond. The explosion was triggered in the test vessel center at position 0.03 m. The initial conditions were set for premixing time 0.25 second. The melt droplets mass fraction was 80% of the corium mass entered in the water at triggering time.
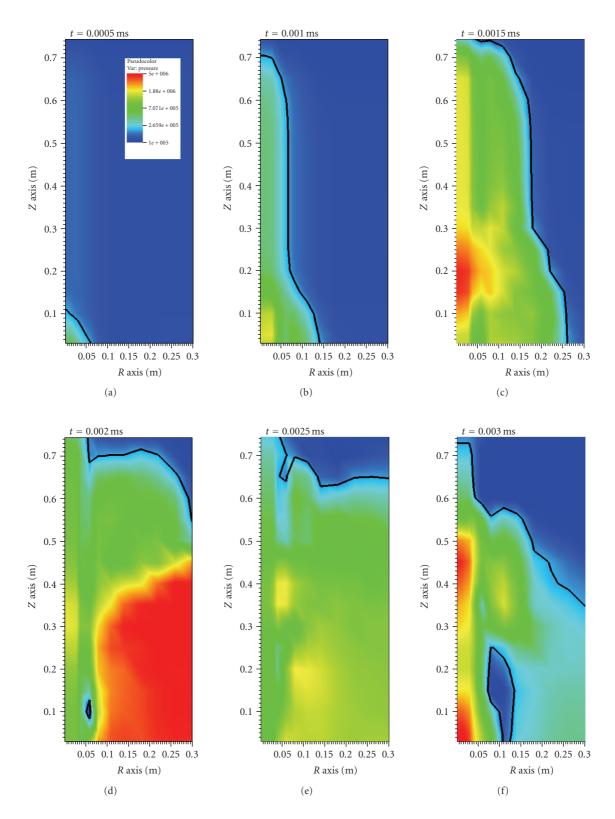
triggering time in the experiment. The simulation results are given for different trigger zone positions. In the simulations, the steam explosion was triggered between the bottom (0.03 m) and the near-mid (0.3 m) parts of the test vessel. The melt droplets mass participating in the steam explosion was set to fractions 40%, 60%, 80%, and 100% of the total corium mass entered in the water at triggering time. The pressure was tracked at the pressure detectors IVDP101 and IVDP102 positions (Figures 1 and 2).

The results on Figure 5 reveal that the melt droplets mass significantly influences the pressure peak height and its position. With a larger melt mass, more melt droplets are available for fine fragmentation, resulting generally in higher pressure peaks and larger pressure impulses. With larger melt droplets mass, also the steam explosion develops faster due to more intense interactions, and so the pressure peaks occur earlier. The calculated pressure peak becomes comparable with the measured data if around 40–80% of the injected corium mass in the water, presented as melt droplets, were taken into account in the explosion simulations. This observation is in agreement with the premixing simulation results, where around 80% of the jet inside the water were fragmented into melt droplets at triggering time, and we have to consider that part of these corium droplets is already frozen and so cannot efficiently participate in the steam explosion [9]. The so established melt droplets mass involved in the steam explosion (i.e., fine fragmentation) is comparable also with the experimentally measured mass of fine fragments (smaller than 0.425 mm) in Table 1. On Figure 5, we see that the influence of the assumed triggering position on the steam explosion development is quite stochastic and less expressive. So, we can conclude that the strength of a steam explosion is governed mainly by the premixture conditions at triggering time.

Figure 6 shows the pressure field propagation inside the test vessel during the steam explosion. The steam explosion was triggered at the test vessel bottom. It was assumed that in the interaction zone 80% of the corium mass are in form of molten droplets, which can participate in the steam explosion. The pressure field first developed along the interaction zone and then propagated towards the test vessel wall, where also the pressure detectors IVDP101 and IVDP102 were placed (Figures 1 and 5). The pressure increase near the wall was due to the incoming and reflecting pressure superposition. After the heat transfer process from the hot melt to water ceased, the pressure started to decrease.

4. CONCLUSION

Fuel coolant interaction computer codes have to be validated with steam explosion experimental data to be able to perform reliable simulations. The purpose of the presented work was to model the TROI-13 steam explosion experiment with the computer code MC3D to establish the modelling capabilities of the code and to get additional insight into the FCI phenomenon. The experiment was modelled according to public available experimental data, applying recommended or default MC3D numerical and model parameters. For the explosion simulation, the correct determination of

the premixture conditions at steam explosion triggering is essential. Therefore, first, the premixing conditions were simulated and discussed in details to enable the appropriate determination of the mass, size, temperature, and distribution of the corium droplets at steam explosion triggering. The corium droplets are so important because they drive the heat transfer and represent the source for fine fragmentation during the steam explosion.

The comparison of premixing results with experimental measurements revealed that the premixing simulations overestimate the melt droplets mean Sauter diameter if the MC3D coarse drop break up model damping functions are used, and underestimate it if they are suppressed. The melt droplet coalescence was overestimated in any case, if the damping functions were used or if they were not used. It turned out that using only the first damping function, quite reasonable premixing results are obtained in the initial stage of the melt pour, lasting also beyond the steam explosion triggering time. Therefore, these premixing results were used to define the initial conditions for the steam explosion simulations. The steam explosion simulations results were in reasonable agreement with the experimental measurements. The results revealed that there is an important influence of the involved melt droplets mass on the steam explosion process. The influence of the assumed steam explosion triggering location on the steam explosion strength was less expressive. Due to the importance of the adequate active melt droplets mass prediction at triggering time on the subsequent development of the steam explosion, it is of utmost importance to appropriately consider in the FCI codes also melt droplets solidification phenomena.

REFERENCES

[1] L. Cizelj, B. Končar, and M. Leskovar, "Vulnerability of a partially flooded PWR reactor cavity to a steam explosion," *Nuclear Engineering and Design*, vol. 236, no. 14–16, pp. 1617–1627, 2006.

[2] M. L. Corradini, B. J. Kim, and M. D. Oh, "Vapor explosions in light water reactors: a review of theory and modeling," *Progress in Nuclear Energy*, vol. 22, no. 1, pp. 1–117, 1988.

[3] D. Magallon, J. H. Song, R. Meignen, and N. D. Suh, "SERENA: Proposal for a Phase 2 programme," OECD Research programme on fuel-coolant interaction, Revision 2, May 2006.

[4] B. D. Turland and G. P. Dobson, "Molten Fuel Coolant Interactions: a state of the art report," European Commission Report 16874, 1996.

[5] J. H. Song, I. K. Park, Y. S. Shin, et al., "Fuel coolant interaction experiments in TROI using a UO$_2$/ZrO$_2$ mixture," *Nuclear Engineering and Design*, vol. 222, no. 1, pp. 1–15, 2003.

[6] R. Meignen and S. Picchi, "MC3D Version 3.5: User's guide," IRSN Report, NT/DSR/SAGR/05-84, 2005.

[7] R. Meignen, "Version 3.5 of the software MC3D: validation report," IRSN Report, NT/DSR/SAGR/05-89, 2005.

[8] "OECD Research Programme on Fuel-Coolant Interaction; Steam Explosion Resolution for Nuclear Applications— SERENA; Final Report," Nuclear Safety NEA/CSNI/R(2007)11, September 2007.

[9] M. Leskovar, R. Meignen, C. Brayer, M. Burger, and M. Buck, "Material influence on steam explosion efficiency: state of understanding and modelling capabilities," in *Proceedings of the European Review Meeting on Severe Accident Research (ERMSAR '07)*, p. 10, Karlsruhe, Germany, June 2007.

Research Article

Using Safety Margins for a German Seismic PRA

Ralf Obenland,[1] Theodor Bloem,[1] Wolfgang Tietsch,[1] and Jang-Bahadur Singh[2]

[1] *Westinghouse Electric Germany GmbH, Dudenstraße 44, 68167 Mannheim, Germany*
[2] *EnBW Kernkraft GmbH, Rheinschanzinsel, 76661 Philippsburg, Germany*

Correspondence should be addressed to Ralf Obenland, ralf.obenland@de.westinghouse.com

The German regulatory guide demands the performance of a probabilistic risk assessment (PRA) including external events. In 2005, a new methodology guideline (Methodenband) based on the current state of science and technology was released to provide the analyst with a set of suitable tools and methodologies for the analysis of all PRA events. In the case of earthquake, a multilevel verification procedure is suggested. The verification procedure which has to be used depends on the seismic risk at the site of the plant. For sites in areas with low seismic activity no analysis or only a reduced analysis is proposed. This paper describes the evaluation of safety margins of buildings, structures, components and systems for plants at sites with high seismic risk, corresponding to the German methodology guideline. The seismic PRA results in an estimation of core damage frequencies caused by earthquakes. Additionally, the described approach can also be adapted for the usage in a reduced analysis for sites with lower earthquake risks. Westinghouse has wide experience in performing seismic PRA for both BWR as well as PWR plants. Westinghouse uses the documented set of seismic design analyses dating from construction phase and from later updates, if done, as a basis for a seismic PRA, which means that usually no costly new structural mechanics calculations have to be performed.

1. VERIFICATION PROCEDURE OF THE GERMAN METHODOLOGY GUIDELINE

In the case of earthquakes, a multilevel verification procedure is suggested in the new German methodology guideline (Methodenband) [1] which requires a probabilistic analysis only for those nuclear power plants with an earthquake intensity $I_{DBE}(MSK) > 6$ on the site (DBE: Design Basis Earthquake, MSK: Medvedev-Sponheuer-Karnik-Scale, comparable with the European macroseismic scale (EMS)). For earthquake intensities I_{DBE} between 6 and 7, a reduced analysis is possible by demonstrating sufficient safety margins to carry loads of an earthquake with an intensity of $I = I_{DBE} + 1$. For earthquake intensities I_{DBE} above 7 a full scope analysis evaluating seismic fragilities for buildings, structures, mechanical, and electrical components is mandatory.

2. SEISMIC HAZARD ANALYSIS

Basis for a seismic PRA is a probabilistic seismic hazard analysis (PSHA) for the site estimating the frequencies for earthquakes to exceed a certain intensity as shown in Figure 1. In the PRA, the annual probability of exceedance for earthquakes will be used as initial values for the initiating events in addition to the seismic failure probabilities of buildings, structures, and components to estimate core damage frequencies in different intensity intervals.

While the annual probability of exceedance is given as a function of the earthquake intensity I, the horizontal peak ground acceleration of the design basis earthquake is used as basis for the existing stress calculations for structures and components. Therefore, a mapping associating peak ground acceleration with intensity as in Figure 2 has to be established. Figure 2 shows pairs of variates for some German plants according to the German methodology guideline. This guideline suggests also a doubling of the peak ground acceleration with each step in intensity, also known as Cancani correlation, with respect to the design basis earthquake at the site of the plant. The Cancani approximation can be improved by the usage of site specific response spectra for different annual probabilities of earthquakes and for different intensities, respectively. Site specific response spectra have been estimated for different sites in Germany. Calculation of site specific response spectra results for example in lower peak ground acceleration values as a function of the
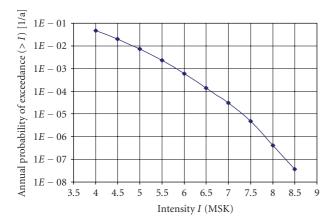
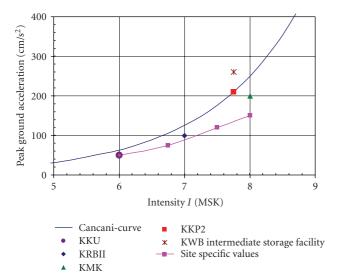FIGURE 1: Hazard curve of seismic risk at plant-site.

FIGURE 2: Classification of earthquake intensity to peak ground acceleration according to Cancani. Site specific spectra provide a higher level of accuracy and a possibility for improvements.

earthquake intensity. Typically, commonly used standardized response spectra were applied for earthquake calculations during the construction phase of a plant. As Figure 2 shows, the estimation of site specific response spectra can provide quite large safety margins in a seismic PRA.

3. IDENTIFYING THE PLANT SPECIFIC SCOPE OF THE ANALYSIS

To perform a seismic PRA, it has to be identified which plant specific beyond design-basis accidents, which lead directly to core damage sequences, and which design-basis accidents can be initiated by an earthquake. Therefore, all buildings, structures, and components have to be identified whose seismic-induced failure could lead to such accidents. Furthermore, it has to be identified which are the seismic relevant buildings, structures, and components of the corresponding safety systems needed to cope the design-basis accidents. Examples of beyond design-basis accidents are a

collapse of the reactor building, breakdown of the reactor pressure vessel, and failure of all primary piping as well as a structural failure or loss of the integrity of the cooling system circuit of the fuel storage pool. As design-basis accidents loss of offsite power, loss of main heat sink and main feed water, loss of coolant accident (LOCAs) and an interaction with flooding of safety related systems have to be considered.

For the identified structures and components a screening procedure supported by plant walkdowns is employed to reduce the amount of detailed investigation based on the calculation of safety factors and the estimation of fragility curves.

4. ASSUMPTIONS TO SIMPLIFY THE ANALYSIS

To reduce the scope of the analysis some conservative assumptions can be made. Above earthquake intensity 6, for which the analysis is done, a loss of offsite power is directly assumed which also covers a loss of main heat sink and main feed water, so that the amount of structures and components to be investigated is significantly reduced by those structures and components whose seismic-induced failure can initiate such a transient. Furthermore, a failure of all parts of the plant which are not designed to withstand the loads of an earthquake is assumed. As pipes are relatively robust against seismic loads, the failure of single pipes which are connected to the reactor pressure vessel can be added to the beyond design-basis accidents which lead directly to a core damage. Emergency procedures and operator procedures which require human actions outside the control room are not considered since buildings and rooms may not be accessible after an earthquake. An exception to this are operator actions to guarantee decay heat removal from the fuel storage pool under the condition that its integrity is preserved, due to the long time available.

5. SCREENING

All components needed to cope with design-basis accidents as modeled in the Level-1-PSA have to be considered for a seismic evaluation. Additionally, all relevant passive components (e.g., heat exchangers, tanks, and piping including their corresponding hangers and supports) have to be added. To reduce the large amount of components, generic values for seismic rugged components from the literature, for example [2], or results of shake table tests can be used. The usage of the generic values for typical plant components has to be verified by plant walkdowns.

6. PLANT WALKDOWNS

Plant walkdowns are an essential part of the seismic PRA to verify the screening done for seismic rugged components as mentioned in the previous chapter and also to support the estimation of safety margins on the basis of the existing stress analyses. Further goals of plant walkdowns are the identification of components with high resistivity against seismic loads and the identification of components where only a low resistivity is expected. Additionally nonsafety-related

components or structures have to be identified which can impact safety-related components as a result of seismic failure, for example, through collision or falling.

Prior to the walkdowns, a detailed planning with identification of the structures and components to be reviewed has to be done, including the preparation of record sheets with component specific criteria and checklists. The plant walkdowns are performed by seismic qualification and system experts accompanied by experts from the power plant. A detailed recording of the plant walkdowns is mandatory. The documentation of the plant walkdowns comprehends the summary of the record and the preparation of a photo documentation.

7. CALCULATION OF SAFETY FACTORS AND FRAGILITY CURVES

Westinghouse uses safety margins in the existing stress calculations to extract safety factors and estimate fragility curves as a function of the peak ground acceleration as described in [3]. The failure probability of structures and components can be calculated by

$$F_{\text{Failure}}(A, Q) = \Phi\left[\frac{\ln(A/\breve{A}) + \beta_U \cdot \Phi^{-1}(Q)}{\beta_R}\right], \quad (1)$$

F_{Failure} describes the probability of failure during an earthquake with a peak ground acceleration A at the confidence level Q. Φ and Φ^{-1} are the distribution function of the standardized normal distribution and its inverse distribution function. β_U and β_R describe the uncertainty and the scattering of the safety reserve factor $\breve{F}_{\text{SR}}$. The safety reserve factor $\breve{F}_{\text{SR}}$ is a product of all individual safety factors $\breve{F}_i$ described in (2) for the calculation of $\breve{A}$, the horizontal peak ground acceleration with the failure probability of 50% (Median):

$$\breve{A} = A_{\text{DBE}} \cdot \breve{F}_{\text{SR}} = A_{\text{DBE}} \cdot \prod_i \breve{F}_i, \quad (2)$$

A_{DBE} is given by the acceleration of the plant design basis earthquake. Examples for safety factors of a building are the strength factor with 1.5, the factor for hardening of concrete by time with 1.2, the factor for inelastic energy absorption with 1.4, the factor for broadening of the response spectra with 1.1 or the factor for the attenuation of intensity with depth of the building in ground with 1.1. These factors result in a typical safety reserve factor of approximately larger than 3. Figure 3 shows the corresponding fragility curve calculated by (1).

The fragility curve, shown in Figure 3 for three different confidence levels Q, describes the building failure probability as a function of the horizontal peak ground acceleration. To calculate point values for the quantification of core damage frequencies the median curve with a confidence level of 50% is used. To derive safety factors out of the existing documents of the seismic design analyses, the construction company of the buildings should be consulted.

Examples for safety factors of a component, here a pipe, are the factors for broadening the ground and floor response
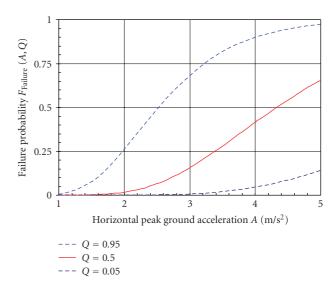
FIGURE 3: Example of a fragility curve for a building.
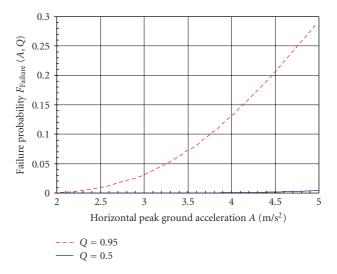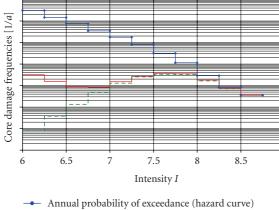
FIGURE 4: Example of a fragility curve for components, respectively for a pipe.

spectra with 1.1 and 1.6, the factor for the attenuation of intensity with depth of the building in ground with 1.1, the strength factor with 1.3, the three hinge factor with 1.2, the factor for inelastic energy absorption with 2.2, and the factor for damping of the floor response spectra with 1.2. These factors result in a typical safety reserve factor of approximately larger than 7 for the example of a pipe. The corresponding fragility curve is shown in Figure 4.

Because of the high resistivity of a pipe against seismic loads only a part of the fragility curve with a confidence level Q of 95% is visible, whereas the median fragility curve coincides nearly with the x-axis as indicated.

The procedure for using safety margins to calculate safety factors is described in detail in the German methodology guideline.

FIGURE 5: Core damage frequencies for different intensity intervals. For comparison the corresponding annual probability of exceedance and the fraction of seismic-induced beyond design-basis accidents are shown. Values on the y-axis are omitted intentionally.

8. MODELING AND QUANTIFICATION

In the last step of the full analysis within the scope of a seismic PRA for plants at sites with high seismic risk, core damage frequencies are calculated for individual intensity intervals in the relevant intensity area as shown in Figure 5. The relevant intensity area reaches from a reasonable minimum intensity where no seismic-induced failure would be anticipated for earthquakes with lower intensities to a maximum value where the probability for the occurrence of an earthquake becomes negligible. According to the German methodology guideline, where no analysis has to be done (see Section 2) for plants with intensity 6 or less for the design basis earthquake, intensity 6 as minimum intensity was used in the example shown in Figure 5.

In order to estimate core damage frequencies, the existing Level-1-PSA model can be separately adapted for each individual intensity interval. As frequency for the initiating event of the anticipated design-basis accident (loss of offsite power), the annual probability of earthquakes to exceed the maximum intensity in each intensity interval is used. The seismic-related failures and unavailabilities of buildings, structures, and components, estimated by the fragility curves, are superposed with the corresponding stochastic unavailabilities.

For beyond design-basis accidents which cannot be coped with the existing safety systems, the core damage frequencies correspond directly to the annual probability of earthquakes from the hazard curve and the probabilities of the seismic-induced failure of buildings, structures, and components which lead to the beyond-design-basis accidents. For design-basis accidents the core damage frequencies result from the annual probability of earthquakes, the assumed probability that such an accident is caused by an earthquake and from the stochastic and seismic-related failure probabilities of the relevant buildings, structures and

components which are needed to cope the accident. As described before, loss of offsite power is assumed already above intensity 6.

Figure 5 shows an example of calculated core damage frequencies in 11 intensity intervals from a seismic PRA for a German nuclear power plant. With increasing intensity, the initial annual probabilities of earthquakes become lower. In the last intensity interval, the remaining probability of earthquakes exceeding intensity 8.5 is directly added to core damage frequencies. At low earthquake intensities the anticipated loss of offsite power in conjunction with the stochastic unavailabilities of components dominates the result. This region of low intensities contributes with approximately 40% to the overall result. Seismic-related unavailabilities have nearly no influence. This supports the assumption that no earthquakes with intensities below 6 are to be considered. At high earthquake intensities the result is dominated by the seismic-induced failure of buildings and structures leading to beyond design-basis accidents. This region contributes with approximately 60% to the overall result. Improvements in the analysis due to site specific response spectra, as described in Section 2, lead to a reduction of core damage frequencies and therefore also to a reduction of the contribution of the high-intensity region to the overall result. The main contribution results from the failure of buildings and structures. The failure of components, especially of pipes, is only secondary.

9. REDUCED ANALYSIS

As described before, a reduced analysis is possible for plants at sites with earthquake intensities above 6 and equal or lower than 7. The procedure for this purpose is a considerably reduced procedure of the described full scope analysis. The verification of resistivity against seismic loads from an earthquake with one intensity step higher than the intensity of the design basis earthquake is done by fragility curves for individual buildings, structures, and components, which contribute by experience in a decisive way to the overall result. As criteria for the choice of the buildings, structures and components, which have a dominant influence on the overall result, experiences from previous PRAs, generic values for seismic-rugged components, plant walkdowns to identify components with low resistivity against seismic loads as well as the existing seismic analyses from the construction phase of the plant or from later updates, if done, can be used.

10. SUMMARY AND EXPERIENCES

Westinghouse used the procedure described by the new German methodology guideline during the development of a seismic PRA for a German BWR. Also a corresponding seismic PRA for a German PWR is currently in progress.

Due to the high core damage frequencies at low earthquake intensities caused by the conservatively assumed loss of offsite power in association with the stochastic unavailabilities of components, a modeling of all available safety systems is needed. The seismic-related unavailabilities of components are secondary, thereby their stability is the most

important part. Normally, all documents needed for the analysis are available at the site from the construction phase, so that no costly new calculations have to be performed. To derive safety factors for buildings their construction company should be consulted. The described screening procedure results in a significant reduction of the number of components to be analyzed and of fragility curves to be created. Plant walkdowns can be limited to one to two weeks. An important safety factor results from realistic site specific response spectra in comparison to the usually conservative response spectra used for the design phase. For a full scope analysis approximately 10 fragility curves for buildings and structures and approximately 30 fragility curves for components and piping have to be calculated. The overall conclusion for the development of a German seismic PRA by using safety margins is, that the procedure described in the German methodology guideline is feasible and realizable with reasonable effort.

ACKNOWLEDGMENTS

REFERENCES

[1] Facharbeitskreis Probabilistische Sicherheitsanalyse für Kernkraftwerke, Methoden zur probabilistischen Sicherheitsanalyse für Kernkraftwerke, Stand August 2005, BfS SCHR 37/05, Wirtschaftsverlag NW/Verlag für neue Wissenschaft GmbH, Salzgitter, Oktober 2005.

[2] K. L. Merz, "Generic seismic ruggedness of power plant equipment (revision 1)," Final Report EPRI NP-5223-SLR1, Electric Power Research Institute, Palo Alto, Calif, USA, August 1991.

[3] R. P. Kennedy and M. K. Ravindra, "Seismic fragilities for nuclear power plant risk studies," *Nuclear Engineering and Design*, vol. 79, no. 1, pp. 47–68, 1984.

Research Article

Comparison of Methods for Dependency Determination between Human Failure Events within Human Reliability Analysis

Marko Čepin

Jožef Stefan Institute, Reactor Engineering Division, Jamova cesta 39, 1000 Ljubljana, Slovenia

Correspondence should be addressed to Marko Čepin, marko.cepin@ijs.si

The human reliability analysis (HRA) is a highly subjective evaluation of human performance, which is an input for probabilistic safety assessment, which deals with many parameters of high uncertainty. The objective of this paper is to show that subjectivism can have a large impact on human reliability results and consequently on probabilistic safety assessment results and applications. The objective is to identify the key features, which may decrease subjectivity of human reliability analysis. Human reliability methods are compared with focus on dependency comparison between Institute Jožef Stefan human reliability analysis (IJS-HRA) and standardized plant analysis risk human reliability analysis (SPAR-H). Results show large differences in the calculated human error probabilities for the same events within the same probabilistic safety assessment, which are the consequence of subjectivity. The subjectivity can be reduced by development of more detailed guidelines for human reliability analysis with many practical examples for all steps of the process of evaluation of human performance.

1. INTRODUCTION

The human reliability analysis (HRA) is a systematic framework, which includes the process of evaluation of human performance and associated impacts on structures, system, and components for a complex facility. The process and the results are highly subjective, and they are the input for probabilistic safety assessment (PSA), which deals with many parameters of high uncertainty [1–4].

Many methods connected with HRA were developed in the last decades: for example, technique for human error rate prediction (THERP) [5], systematic human action reliability procedure (SHARP) [6], accident sequence evaluation program (ASEP) [7], a technique for human event analysis (ATHEANA) [8, 9], cognitive reliability and error analysis method (CREAM) [10], human cognitive reliability (HCR) [11], standardized plant analysis risk HRA (SPAR-H) [12], and Institute Jožef Stefan human reliability analysis (IJS-HRA) [13–15].

Those methods have some unique and some common features [16, 17]. It is difficult to judge them or to compare them in sense, which method is better than others. It is observed that in the methods developed recently more attention was given to the cognitive portion of human failure events (HFEs) [16, 17]. An important feature is the dependency [13, 18], which is more emphasized at more recent methods, although the standpoint was stated years ago with THERP [5]. The mentioned methods use the data, the human reliability databases. Well ago, less data was available and many specific human error probabilities and human shaping factors, which adjust those probabilities, were determined based on expert judgement. Nowadays, much more data is available due to more experience in the plant operation and due to more training in plant simulators. This may lead to the conclusion that more recent methods are less subjective.

The objective of the paper is to show that subjectivism can largely impact the HRA results and consequently the results and applications of PSA in a nuclear power plant (NPP) with special emphasis on consideration of dependency. The objective is to identify the key features, which may decrease subjectivity of HRA.

Two methods from the set mentioned above are selected for their detailed comparison in an example case of real
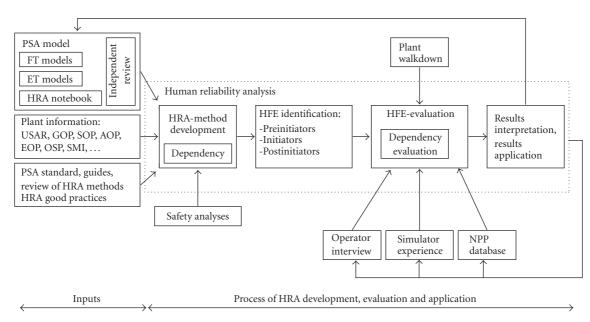
FIGURE 1: Scheme of IJS-HRA method.

probabilistic safety assessment model, which include human reliability analysis. Those two are: SPAR-H [12] and IJS-HRA [13, 14]. They are selected as they are relatively new methods, which encompass the previous knowledge in the field, which are relatively simple for their application, and which pay an acceptable level of attention to the issue of dependency, which is the focus of the work.

2. METHODS

2.1. IJS-HRA

Figure 1 shows the scheme of the IJS-HRA method [13]. The method for evaluation of HFE is developed including consideration about dependencies between HFE [5, 13]. Figure 1 shows that identification of HFE distinguishes preinitiator events (i.e., preinitiators), initiator events (i.e., initiators) and postinitiator events (i.e., postinitiators). Preinitiators are the events that may cause the equipment to be unavailable before the initiating event has occurred. Initiators are the events that may contribute to the occurrence of initiating events. Postinitiators are the events, which are connected with human actions to prevent accident or mitigate its consequences after initiating event has occurred. Evaluation of HFE including evaluation of dependencies integrates assessment of human error probabilities (HEPs) with plant information, operator interview, simulator experience, and plant database.

The five levels of dependency are determined according to THERP: zero dependency (ZD), low dependency (LD), moderate dependency (MD), high dependency (HD), and complete dependency (CD) [5]. Human error probability (HEPs) of dependent HFE A and B is determined according to equation: $P_{XD}(P_B \mid P_A) = P_A*(1 + K \cdot P_B)/(K + 1)$; where $K = 0, 1, 6, 19, \infty$, for dependency levels ZD, LD, MD,

HD, and CD, where $X = Z, L, M, H,$ and C, respectively [5].

Figures 2 and 3 show how dependency between HFE is determined for preinitiators and for postinitiators, respectively. Initiators are treated similarly as postinitiators. For preinitiators, there is an additional algorithm, which from independent HFE A and its dependent event HFE B calculates their HEP as the geometry average of both [13].

Figures 2 and 3 show that based on the parameters, which are connected with their representative HFE, the dependency evaluation code is identified (e.g., LD12). Dependency evaluation code consists of first two characters identifying the level of dependency (e.g., ZD, LD, MD, HD, and CD). The next numbers in the code represent the scenario number of the corresponding scenario from dependency method presented in its respective figure and identify parameters that are important for determining the level of dependency: for example, cue, time between, crew, stress, complexity, location, system, action description, procedure, timing, person, and action similarity [13]. For example, for 2 dependent postinitiators, a dependency level LD is determined on Figure 3 (LD12), which shows: different cue, 5–30 minutes between the events, low stress, simple action, and no change of probability needed as joined HEP > 1E-5.

2.2. SPAR-H

Standardized plant analysis risk HRA (SPAR-H) is a method for estimating the human error probabilities (HEPs) associated with operator actions and decisions in nuclear power plants [12]. Table 1 shows how dependency between HFE is determined. Five levels of dependency are determined, similarly to THERP and IJS-HRA. The parameters for determining the level of dependency differ from THERP and from IJS-HRA.

Preinitiator	System	Person	Action description	Procedure	Timing	Action similarity	Condition	No	Dependency Level
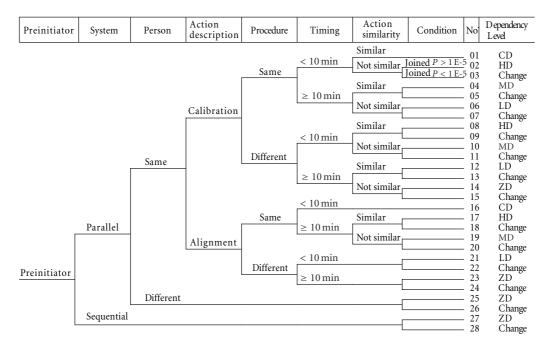
Figure 2: IJS-HRA dependency—preinitiator HFE.

Postinitiator	Cue	Time between	Crew	Stress	Complexity	Condition	No	Dependency level
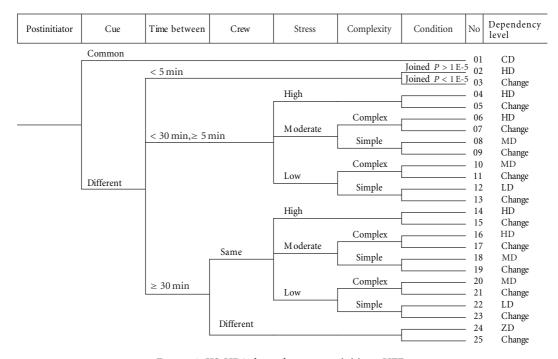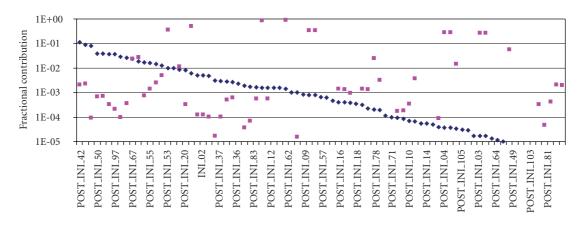
Figure 3: IJS-HRA dependency—postinitiator HFE.

3. ANALYSIS AND RESULTS

3.1. Qualitative comparison

Table 2 shows how dependency determined in IJS-HRA method suits the dependency determined in SPAR-H method (theoretical comparison of both dependency methods).

Table 3 is the subset of Table 2. Table 3 focuses only to those scenarios (specific scenario suits specific set of parameters), which suit real HFE considered in the specific HRA (practical comparison of both dependency methods based on specific PSA model). Both tables show that for specific HFE their respective HEP is evaluated as a different value, if it is determined with one or the other method.

Figure 4: Comparison of fractional contribution of HFE.

Table 1: SPAR-H dependency.

Condition number	Crew (same or different)	Time (close in time or not close in time)	Location (same or different)	Cues (additional or no additional)	Dependency	
1	S	C	S	NA	COMPLETE	When considering
2				A	COMPLETE	recovery in a series, for
3			D	NA	HIGH	example, 2nd, 3rd, or
4				A	HIGH	4th checker:
5		NC	S	NA	HIGH	if this error is the
6				A	MODERATE	*3rd error in the sequence*,
7			D	NA	MODERATE	then the dependency is
8				A	LOW	at least *moderate*;
9	D	C	S	NA	MODERATE	if this error is the
10				A	MODERATE	*4th error in the sequence*,
11			D	NA	MODERATE	then the dependency
12				A	MODERATE	is at least *high*
13		NC	S	NA	LOW	
14				A	LOW	
15			D	NA	LOW	
16				A	LOW	
17					ZERO	

3.2. Quantitative comparison

64 HFEs exist in the PSA model, which HEP is changed if HRA dependency method changes. Table 4 shows a part of those HFE with identified dependency levels and respective HEP for both methods IJS-HRA and SPAR-H. Terms CALC and IND marked at preinitiators represent the calculation of final HEP as the geometry average between the independent value of HEP for action at one train and the respective dependent HEP assessed as low dependency (LD12) for similar action at the other train.

Table 5 shows the results of risk increase factor and risk decrease factor of selected HFE calculated based on analysis

runs with PSA model based on IJS-HRA dependency and based on SPAR-H dependency considered. Selected HFE in the table are those with RDF > 1, 05 and RIF > 2, which are a criteria for identification of risk significant events. The differences between both cases are very large.

Table 5 shows that identification of important HFE shows only one HFE, which is identified as important in both analyses (POST_INI_04, which deals with operator establishing auxiliary feedwater pumps). The difference between both cases about the core damage frequency is very large, too. It differs for more than one order of magnitude.

Figure 4 shows a comparison of fractional contribution of HFE for both analyses. The figure shows that there are no

TABLE 2: Comparison of dependency levels—all scenarios are presented.

Postinitiators		Preinitiators	
IJS-HRA	SPAR-H	IJS-HRA	SPAR-H
CD1	CD1, HD3, HD5, MD7, MD9, MD11, LD13, LD15	CD1	CD1, HD3
HD2	CD1, HD3, MD9, MD11	HD2	CD2, HD4
HD4	MD6, LD8, LD14, LD16	MD4	HD5, MD7
HD6	MD6, LD8, LD14, LD16	LD6	MD6, LD8
MD8	MD6, LD8, LD14, LD16	HD8	CD1, HD3
MD10	MD6, LD8, LD14, LD16	MD10	CD2, HD4
LD12	MD6, LD8, LD14, LD16	LD12	HD5, MD7
HD14	MD6, LD8	ZD14	MD6, LD8
HD16	MD6, LD8	CD16	CD1, CD2, HD3, HD4
MD18	MD6, LD8	HD17	HD5, MD7
MD20	MD6, LD8	MD19	MD6, LD8
LD22	MD6, LD8	LD21	CD1, CD2, HD3, HD4
ZD24	LD14, LD16	ZD23	HD5, MD6, MD7, LD8
		ZD25	MD9, MD10, MD11, MD12, LD13, LD14, LD15, LD16
		ZD27	CD1, CD2, HD3, HD4, HD5, MD6, MD7, LD8, MD9, MD10, MD11, MD12, LD13, LD14, LD15, LD16

TABLE 3: Comparison of dependency levels—only scenarios, which are applicable for HFE of the specific PSA model.

Preinitiators		Postinitiators	
IJS-HRA	SPAR-H	IJS-HRA	SPAR-H
LD12	HD5	CD1	CD1
ZD27	MD7, LD13, LD16	MD8	HD4, LD8
HD17	HD5	ZD24	LD14, LD16
		LD12	LD8
		HD2	CD2, MD12
		LD22	MD6, LD8
		MD20	LD8

TABLE 4: Selected HFE with quantified HEP (for IJS-HRA and for SPAR-H).

Basic event ID	Dependency level IJS-HRA	Final HEP IJS-HRA	Dependency level SPAR-H	Final HEP SPAR-H
PRE_INI_01	CALC, IND, LD12	1,91E-03	HD5	5,00E-01
PRE_INI_02	CALC, IND, LD12	1,91E-03	HD5	5,00E-01
POST_INI_34	ZD24	4,52E-03	LD16	5,43E-02
POST_INI_42	MD8	1,71E-01	LD8	8,08E-02
POST_INI_53	ZD24	1,58E-02	LD14	6,50E-02
POST_INI_63	LD22	5,07E-02	HD-4th-in-seq	5,00E-01
POST_INI_66	HD2	5,16E-01	MD12	1,70E-01
POST_INI_69	ZD24	1,04E-03	LD14	5,10E-02
POST_INI_79	ZD24	1,96E-04	MD-3th-in-seq	1,43E-01
POST_INI_83	MD18	1,45E-01	LD8	5,28E-02
POST_INI_88	MD20	1,43E-01	LD8	5,06E-02
POST_INI_102	ZD24	2,91E-04	HD-5th-in-seq	5,00E-01

TABLE 5: Results of importance of HFE.

IJS-HRA			
HFE identification	RDF	HFE identification	RIF
POST_INI_42	1,13E+00	POST_INI_04	2,26E+02
POST_INI_63	1,09E+00	POST_INI_12	7,46E+01
POST_INI_88	1,09E+00	POST_INI_100	4,49E+01
		POST_INI_95	3,66E+01
		INI_01	2,34E+01
		INI_02	2,34E+01
		POST_INI_102	2,23E+01
		POST_INI_02	1,75E+01
		POST_INI_34	6,73E+00
		POST_INI_35	3,19E+00
		POST_INI_69	2,68E+00
		POST_INI_63	2,62E+00
		POST_INI_60	2,01E+00
SPAR-H			
HFE identification	RDF	HFE identification	RIF
PRE_INI_06	1,01E+01	POST_INI_53	5,76E+00
PRE_INI_05	8,18E+00	POST_INI_04	5,63E+00
POST_INI_102	2,07E+00		
POST_INI_53	1,55E+00		
PRE_INI_09	1,51E+00		
PRE_INI_10	1,51E+00		
PRE_INI_04	1,40E+00		
PRE_INI_01	1,40E+00		
PRE_INI_02	1,38E+00		
PRE_INI_03	1,38E+00		
POST_INI_79	1,06E+00		

comparable results: events, which contribute significantly, if IJS-HRA dependency is considered, can be insignificant, if SPAR-H dependency is considered and vice versa.

Similarly, large differences exist if instead of five levels of dependency less dependency levels are determined with different equations for evaluation of dependency.

4. CONCLUSIONS

The methods for dependency determination between human failure events within human reliability analysis have been examined.

Consideration of human error probability of the first human failure event in a sequence as it is and an increase of independent human error probability of the next human failure event in a sequence common to most of the HRA methods, except IJS-HRA, which for relatively similar actions determines identical failure probability based on geometry average.

The methods for determination of dependency between human failure events differ mostly in definition of parameters, which impact the dependency, in their application and in the determination of dependency level, which applies to a specific set of parameters. All those distinctions are subjective. This subjectivism can lead to a difference of several orders of magnitude in the results of HRA and in the PSA, which includes HRA. This means significant differences in all PSA results and their applications, for example,

(i) identification of key human failure events, which is an input for prioritization of simulator training,

(ii) calculation of core damage frequency and its sensitivity to changes, which is an input for risk-informed decision-making,

(iii) identification of different key tasks within human failure event in order to identify the key parameters from HRA database.

The subjectivism could be minimized with integration and standardization of

(i) selection of parameters, which affects the dependency between human actions, for example,

(a) persons (e.g., one or more persons involved, e.g., same or different people are performing the actions),

(b) similarity of actions (e.g., similar or not similar action),

(c) similarity of implementation of procedures (e.g., filling the forms without signing the steps of the form or with signing the steps, e.g., same or different procedure for),

(d) similarity of locations (e.g., same or different location),

(e) timing (e.g., sequential performance or a larger time interval between the actions),

(f) stress level (e.g., low, high, optional: moderate),

(g) complexity of actions (e.g., simple or complex actions, where specific definition of simplicity or complexity are important),

(ii) the number of levels of dependency and the formulas for their evaluation (e.g., five levels of dependency as in THERP, SPAR-H, and IJS-HRA with their corresponding formulas).

In addition, the detailed guidelines are needed which would guide the application and which would be highlighted with many practical examples. Database on the examples of quantified human error probabilities for independent tasks, for dependent tasks, and for complete human actions and their dependencies should become a part of nuclear power plant probabilistic safety assessment database.

ACKNOWLEDGMENT

REFERENCES

[1] ASME RA-S-2002, "Standard for probabilistic risk assessment for nuclear power plant applications," The American Society of Mechanical Engineers, 2002.

[2] Regulatory Guide 1200, "An approach for determining the technical adequacy of probabilistic risk assessment results for risk-informed activities," U.S. Nuclear Regulatory Commission, 2004.

[3] M. Čepin and B. Mavko, "A dynamic fault tree," *Reliability Engineering & System Safety*, vol. 75, no. 1, pp. 83–91, 2002.

[4] M. Čepin, "Analysis of truncation limit in probabilistic safety assessment," *Reliability Engineering & System Safety*, vol. 87, no. 3, pp. 395–403, 2005.

[5] A. D. Swain and H. E. Guttman, "Handbook of human reliability analysis with emphasis on nuclear power plant applications," Final Report NUREG/CR-1278, U.S. Nuclear Regulatory Commission, Washington, DC, USA, 1983.

[6] SHARP, "Systematic human action reliability procedure," EPRI. NP-3583, 1984.

[7] A. D. Swain, "Accident sequence evaluation program: human reliability analysis procedure," Tech. Rep. NUREG/CR-4772, U.S. Nuclear Regulatory Commission, Washington, DC, USA, 1987.

[8] W. D. Travers, "Technical basis and implementation guidelines for a technique for human event analysis (ATHEANA)," Tech. Rep. NUREG-1624, U.S. Nuclear Regulatory Commission, Washington, DC, USA, 1999.

[9] J. Forester, D. Bley, S. Cooper, et al., "Expert elicitation approach for performing ATHEANA quantification," *Reliability Engineering & System Safety*, vol. 83, no. 2, pp. 207–220, 2004.

[10] E. Hollnagel, *Cognitive Reliability and Error Analysis Method (CREAM)*, Elsevier, Amsterdam, The Netherlands, 1988.

[11] A. Spurgin, "Another view of the state of human reliability analysis (HRA)," *Reliability Engineering & System Safety*, vol. 29, no. 3, pp. 365–370, 1990.

[12] D. Gertman, H. Blackman, J. Marble, J. Byers, and C. Smith, "The SPAR-H human reliability analysis method," Tech. Rep. NUREG/CR-6883, U.S. Nuclear Regulatory Commission, Washington, DC, USA, 2005.

[13] M. Čepin, "DEPEND-HRA—a method for consideration of dependency in human reliability analysis," *Reliability Engineering & System Safety*. In press.

[14] M. Čepin, "Importance of human contribution within the human reliability analysis (IJS-HRA)," *Journal of Loss Prevention in the Process Industries*, vol. 21, no. 3, pp. 268–276.

[15] A. Prošek and M. Čepin, "Success criteria time windows of operator actions using RELAP5/MOD3.3 within human reliability analysis," *Journal of Loss Prevention in the Process Industries*, vol. 21, no. 3, pp. 260–267.

[16] A. Kolaczkowski, J. Forester, E. Lois, and S. Cooper, "Good practices for implementing human reliability analysis (HRA)," Tech. Rep. NUREG-1792, U.S. Nuclear Regulatory Commission, Washington, DC, USA, 2005.

[17] J. Forester, A. Kolaczkowski, E. Lois, and D. Kelly, "Evaluation of human reliability analysis methods against good practices," Final Report NUREG-1842, U.S. Nuclear Regulatory Commission, Washington, DC, USA, 2006.

[18] J. F. Grobbelaar, J. A. Julius, and F. Rahn, "Analysis of dependent human failure events using the EPRI HRA Calculator," in *Proceedings of the 9th International Topical Meeting on Probabilistic Safety Analysis (PSA '05)*, pp. 499–501, San Francisco, Calif, USA, September 2005.